

Copyright
by
Jun Wan Kim
2008

**The Dissertation Committee for Jun Wan Kim Certifies that this is the approved
version of the following dissertation:**

**Development of Interdigitated Capacitor Sensors for Direct and
Wireless Measurements of the Dielectric Properties of Liquids**

Committee:

Dean P. Neikirk, Supervisor

A. Bruce Buckman

Mircea Driga

Ananth Dodabalapur

Burt Fowler

**Development of Interdigitated Capacitor Sensors for Direct and
Wireless Measurements of the Dielectric Properties of Liquids**

by

Jun Wan Kim, B.S.; M.S.

Dissertation

Presented to the Faculty of the Graduate School of

The University of Texas at Austin

in Partial Fulfillment

of the Requirements

for the Degree of

Doctor of Philosophy

The University of Texas at Austin

December, 2008

Dedication

To my lovely family for their patience, support, and love

Acknowledgements

First of all, I would like to express my special thanks from my bottom of my heart to my supervisor Dr. Dean P. Neikirk for his tremendous amount of support, advice, and patience, and encouragement. I also would like to acknowledge the members of my dissertation committee, Dr. A. Bruce Buckman, and Dr. Mircea Driga, Dr. Ananth Dodabalapur, and Dr. Burt Fowler for their valuable feedback and corrections.

I would like to express my appreciation and gratitude to our former and present members of Team Neikirk, especially Dr. Jooyong Kim, Dr. Byungki Woo, Dr. Byungwha Park, Dr. Sangwook Han, Dr. Yoon Sok Park, Dr. Matthew Andringa, Praveen Pasupathy, Joo-Yun Jung, and our new member Jong Yeon Park. I also would like to thank for their friendship, particularly Dr. Hyung-Sub Kim, Dr. and Chang Hun Lee. In addition, I would like to express my special appreciation to Jongwook Suk, principal engineer in SAMSUNG electronics, for his valuable advice, support, and guidance. Also, my lifetime friend who has been with me more than 12 years in Austin, David Kim, Thanks man for being my friend!

Finally, I deeply appreciate the encouragement and devotion from my mother Song Ja Jung and my only brother Dong Wan Kim. They have provided love and emotional support throughout my life. I also thank my only nephew Min Kevin Kim for making me proud. Thanks for being my nephew. I love you man!.

Development of Interdigitated Capacitor Sensors for Direct and Wireless Measurements of the Dielectric Properties of Liquids

Publication No. _____

Jun Wan Kim, Ph.D.

The University of Texas at Austin, 2008

Supervisor: Dean P. Neikirk

The miniaturization of chemical and biological sensors has received considerable attention in recent years for medical diagnostics, environmental monitoring, pharmaceutical screening, military applications, etc. One interesting area of development in microfluidic system is detecting dielectric properties of MUT (Material Under Test) using IDC (Interdigital Capacitor) electrodes. The IDC chemical sensor has been investigated by many researchers because they are cheap to manufacture and can be easily integrated with other sensing components and signal processing electronics.

This dissertation presents the design, fabrication, and testing of an IDC (interdigital capacitor) electrode sensor for a fluid property monitoring component that can be integrated into a microfluidic system. One practical point of this research is the analytical evaluation of the interdigital electrode capacitance for the detection of conductivity and permittivity of the aqueous solutions, which is not apparently analyzed in other chemical sensor applications. In addition, a new noble methodology of remotely accessing the IDC sensor by wireless inductive coupling similar to EAS (Electronic Article Surveillance) tags is presented.

Table of Contents

List of Tables	X
List of Figures	XI
Chapter 1 Introduction	1
Chapter 2 Initial Works of Microfluidic System	8
2.1 Top and bottom channel incorporated microfluidic system	8
2.2 Airflow channel incorporated microfluidic system	13
2.3 SU-8 gasket design	17
2.4 Simple direct volumetric measuring system	22
Chapter 3 Measuring Dielectric Properties of Liquids	25
3.1 Introduction	25
3.2 Theory	26
3.2.1 Debye dielectric model	26
3.2.2 Dielectric spectroscopy	30
3.3 Interdigitated capacitor (IDC) sensor design	34
3.3.1 Historical perspective	34
3.3.2 Analysis of IDC electrodes using conformal mapping techniques	35
3.3.2.1 IDC electrodes with infinitely thick air layer	35
3.3.2.2 IDC electrodes with an insulation layer.....	40
3.3.3 Dependence of the capacitance on IDC geometric configurations	42
3.3.3.1 Dependence on IDC finger thickness	42
3.3.3.2 Dependence on IDC finger width and spacing	43
3.3.3.3 Dependence on IDC sensor wavelength λ and thickness of insulation layer h_2	45
3.4 Design of IDC sensor	46

Chapter 4	Measurement Techniques.....	52
4.1	Measurement setup	52
4.2	Impedance measurement with z-probe	53
4.3	Impedance measurement with impedance analyzer.....	56
Chapter 5	Detection Mechanism of Direct Measurement.....	60
5.1	Problem with traditional conformal mapping circuit model.....	60
5.2	New equivalent circuit model	61
5.3	Modified equivalent circuit model.....	64
5.3.1	C_p estimation using parallel plate analysis	66
5.3.2	C_{ins} estimation using parallel plate analysis	68
5.3.3	G_{ins} estimation from the measured air data	71
5.4	Measurement of dielectric properties of materials using fitting model analysis.....	73
5.4.1	Extract dielectric properties of known materials	74
5.4.1.1	Extraction of dielectric properties of air	74
5.4.1.2	Extraction of dielectric properties of IPA.....	76
5.4.1.3	Extraction of dielectric properties of DI water	80
5.4.1.4	Extraction of dielectric properties of salt water.....	82
5.4.2	Extract dielectric properties of unknown materials (GeNWs) ..	84
Chapter 6	Detection Mechanism of Wireless Measurement.....	86
6.1	EAS-tag like wireless sensor basics.....	86
6.2	Effects of the R_{tag} and C_{tag}	88
6.3	Detection mechanism of wireless measurement.....	89
Chapter 7	Conclusions and Future Work.....	86
References	95
Vita	101

List of Tables

Table 2.1: Fabrication process parameters for different SU-8 types.....	18
---	----

List of Figures

- Figure 1.1: (a) Schematic diagram illustrating the single pit region within the silicon wafer that is used to confine the bead sensor element; (b) A cross-section schematic shows an expanded view of the fluid delivery method; (c) illustration of the current operation setup for the “Electronic Taste Chips.”; (d) SEM picture of an array of micromachined cavities with chemically derivatized microbeads placed within the cavities [9,10].....2
- Figure 1.2: A fringing field interdigital capacitor electrodes can be visualized as: (a) a parallel-plate capacitor whose (b) electrodes open up to provide (c) a one- sided access to the MUT[12].....4
- Figure 1.3: Electronic structural surveillance tag: (a) reader and sensor circuit diagram, (b) resonant frequency of the sensor based on the state, and (c) commercial EAS (Electronics Article Surveillance) tag [24].....6
- Figure 2.1: Illustration of a top and bottom channel incorporated microfluidic system with (a) passive fluidic top channel and (b) rectangular fluidic top channel.....9
- Figure 2.2: Schematic drawing of the complete microfluidic test system with fluid delivery tubing..... 11
- Figure 2.3: Captured movie frames showing fluid sample passing through the channel.....12.
- Figure 2.4: Schematic design of airflow incorporated microfluidic system: (a) picture of top view of the system and (b) cross-sectional view of the system... 14
- Figure 2.5: Extracted movie frames showing performance of airflow incorporated microfluidic system..... 16.

Figure 2.6: Schematic drawing of a SU-8 gasket/channel microfluidic system.....	19
Figure 2.7: Top and cross-sectional view of the experimental system.....	20
Figure 2.8: Captured movie frames showing DI water passing through SU-8 gasket/channels.....	21
Figure 2.9: Illustration of the basic principle of the simple direct volumetric measuring system.....	22
Figure 2.10: Schematic diagram of a simple direct volumetric measuring system....	23
Figure 2.11: Captured movie frames showing DI water passing through the SU-8 simple direct volumetric measuring system.....	24
Figure 3.1: the Debye equivalent circuit model [39].....	29
Figure 3.2: Dielectric mechanisms over a wide range of frequencies. Ionic and dipolar relaxation at lower frequencies (up to 100 MHz) and atomic and electronic resonances at higher frequencies are shown [40].....	32
Figure 3.3: Cole-Cole diagram of dielectric properties of water [40].....	33
Figure 3.4: Cross-section view of coplanar strip line with fringing electric field [42].....	35
Figure 3.5: Conformal mapping transformations for the calculation of the line capacitance C_1 in the absence of the dielectric substrate layer [42].....	36
Figure 3.6: Conformal mapping transformations for the calculation of the line capacitance C_2 [42].....	39
Figure 3.7: Illustration of the calculation of the capacitances of a multilayered structure (a) using partial capacitance technique [45].....	42.
Figure 3.8: Capacitance change over different IDC finger thickness.....	43
Figure 3.9: Capacitance change over different IDC finger widths.....	44
Figure 3.10: Capacitance change over different IDC finger spacing.....	45

Figure 3.11: Capacitance as a function of the parameter h_2/λ	46
Figure 3.12: Microscopic pictures of fabricated IDC electrodes.	47
Figure 3.13: Illustration of our IDC electrode sensor configuration on a quartz substrate with geometric dimensions.....	48
Figure 3.14: Capacitance of an IDC sensor with a SU-8 insulation layer as a function of frequency: comparison between actual measurement and calculation data.....	51
Figure 4.1: Photographs of z-probe technique setup for the impedance measurement: (a) HP 4194A impedance analyzer and (b) probe station for impedance measurement.....	54
Figure 4.2: Measured data of the IDC sensor using z-probe technique: (a) impedance and phase over frequency range and (b) extracted capacitance value of the IDC sensor.....	56
Figure 4.3: Photographs of (a) IDC sensor bonded to a phono-plug and (b) direct measurement setup with impedance analyzer.....	58
Figure 4.4: Measured data of the IDC sensor using direct measurement technique: (a) impedance and phase over frequency range and (b) extracted capacitance value of the IDC sensor.....	59
Figure 5.1: Cross-section view of IDC sensor with its superimposed equivalent circuit model.....	60
Figure 5.2: (a) Cross-section view of IDC sensor with its superimposed new equivalent circuit model and (b) expanded representation of the circuit.....	62
Figure 5.3: (a) Schematic diagram of electric flux path in the IDC sensor and (b) its modified equivalent circuit model.....	65

Figure 5.4: Schematic diagram of (a) partial capacitance circuit model and (b) parallel plate circuit model of IDC sensor.....	67
Figure 5.5: Equivalent parallel plate circuit model with fixed C_p	68
Figure 5.6: Plot of estimated C_{ins} as a function of the dielectric constant of MUT....	70
Figure 5.7: Equivalent circuit model for G_{ins} estimation.....	71
Figure 5.8: Plot of (a) extracted G_{ins} and (b) $\tan\delta$ of the insulation layer over various frequencies.....	72
Figure 5.9: Equivalent circuit model for extraction of dielectric properties of air....	74
Figure 5.10: Plots of extracted (a) conductivity and (b) relative dielectric constant of air over various frequencies.....	75
Figure 5.11: Plots of first extracted dielectric properties of IPA: (a) dielectric constant and (b) conductivity.....	77
Figure 5.12: Plots of (a) the second iteration results with dielectric constant and conductivity and (b) the third iteration results with dielectric constant and conductivity of IPA.....	78
Figure 5.13: Plots of the final results of the fitting iteration processes: (a) extracted dielectric constant, (b) extracted conductivity, and (c) extracted $\tan\delta$ of IPA.....	79
Figure 5.14: Plots of (a) the first iteration results with dielectric constant and conductivity and (b) the second iteration results with dielectric constant and conductivity of DI water.....	80
Figure 5.15: Plots of the final results of the fitting iteration processes: (a) extracted dielectric constant, (b) extracted conductivity, and (c) extracted $\tan\delta$ of DI water.....	81

Figure 5.16: Plots of the final results of the fitting iteration processes: (a) extracted dielectric constant and conductivity of the salt water ($\sigma_{DC}=6.5$ [mS/cm]) and (b) extracted dielectric constant and conductivity of the salt water ($\sigma_{DC}=17$ [mS/cm]).....	83
Figure 5.17: Plots of the final results of the fitting iteration processes for unknown materials (left column: GeNWs-hexene; right column: GeNWs-octadecene): (a) extracted dielectric constant, (b) extracted conductivity, and (c) extracted $\tan\delta$	85
Figure 6.1: Schematic diagram of simple tag circuit for RFID-type measurement system.....	87
Figure 6.2: Phase plot of the input impedance with varying R_{tag}	88
Figure 6.3: Phase plot of the input impedance with varying C_{tag}	89
Figure 6.4: Schematic diagram of indirect wireless noncontact RFID-type measurement system.	90
Figure 6.5: Photograph of the actual IDC wireless measurement setup.....	90
Figure 6.6: Phase plot change of several liquids over various frequencies.....	91

Chapter 1: Introduction

The development of MEMS (Micro-Electro-Mechanical Systems) technologies has been a driving force for advances in miniaturized sensors, actuators, and structures in many areas of science and engineering. Such interdisciplinary studies and applications made it possible to realize a multifunctional micro-system on a chip. In addition, the micromechanical components can be integrated with electronics and signal processing circuits to develop smart micro sensors such as IC MEMS or CMOS MEMS [1-3].

In particular, the miniaturization of chemical and biological sensors has received considerable attention in recent years for medical diagnostics, environmental monitoring, pharmaceutical screening, military applications, etc [4-8]. One good example of chemical/biological sensor is “Electronic Taste Chip” [9,10]. Our group has been collaborating with other chemists and biologists at the University of Texas at Austin to develop a chip-based sensor array composed of individually addressable polystyrene-poly (ethylene glycol) and agarose microspheres using micromachining MEMS technology. These chemically derivatized microspheres are selectively arranged within anisotropic-etched pyramidal cavities which serve as reaction vessels and analysis chambers. This structure provides single or multi-analyte array system. The analyte is then flowed through the microreactor/analysis chambers. External illumination is applied on one side of the device and colorimetric and fluorescence changes to receptors are observed by a CCD (Charge Coupled Device) camera, which allows the near-real-time digital analysis of complex fluids. This analysis system is capable of the analysis of pH, metal cations, sugars, and antibodies within complex fluids such as beverages and biological samples [10]. Figure 1.1 shows this microbead array detection methodology.

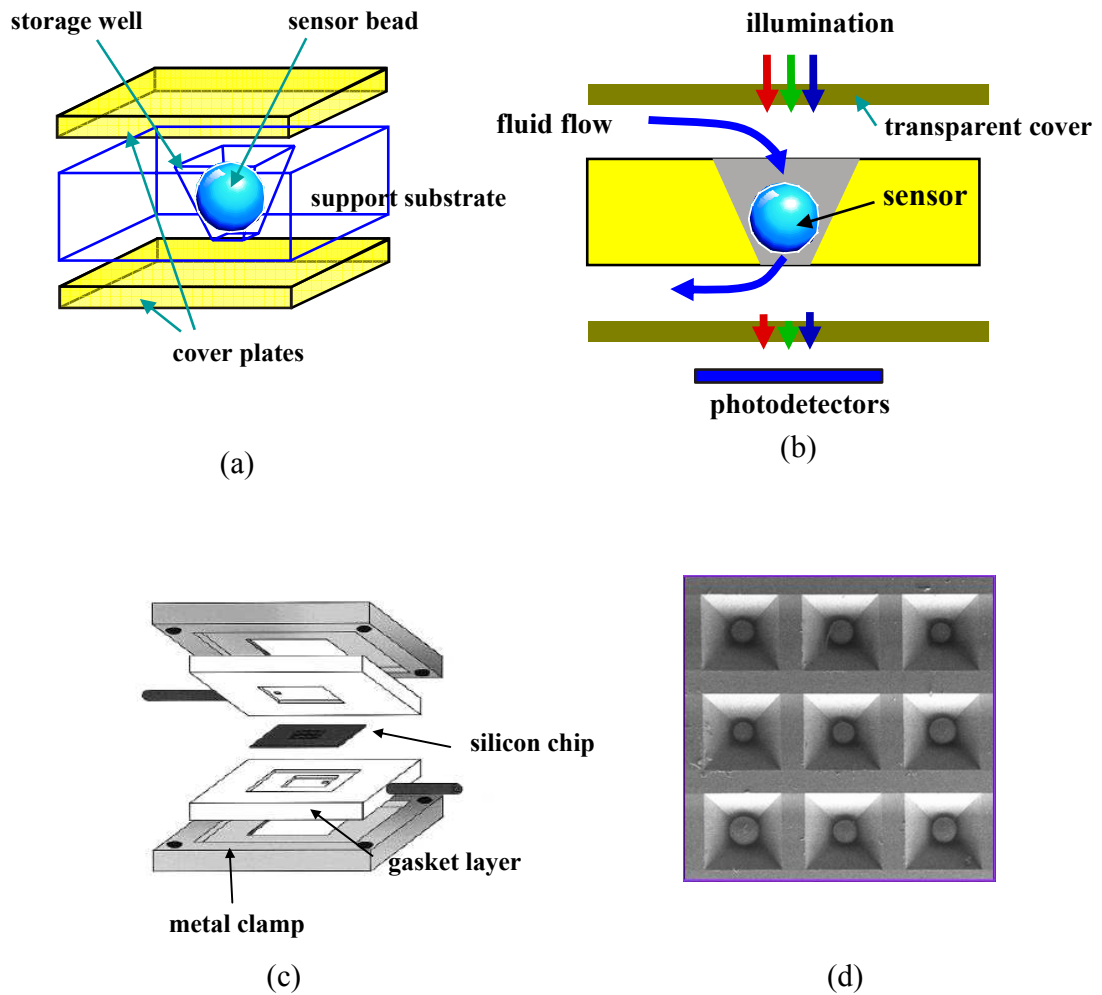


Figure 1.1: (a) Schematic diagram illustrating the single pit region within the silicon wafer that is used to confine the bead sensor element; (b) A cross-section schematic shows an expanded view of the fluid delivery method; (c) illustration of the current operation setup for the “Electronic Taste Chips.”; (d) SEM picture of an array of micromachined cavities with chemically derivatized microbeads placed within the cavities [9,10].

With the integration of microfluidic sample processing components the “Electronic Taste Chip” is a potential application for a lab-on-a-chip system or μ TAS (Micro Total Analysis Systems). In the past, efforts have been focusing on developing airflow-controlled multi-channel microfluidic system in our lab. The motivation behind this research includes decreased usage of expensive reagents, increased functionality, and the separation and control of the reagent/analyte reactions during the transportation of fluid through the microfluidic system. Microchannels are fabricated on both sides of the wafer to allow the fluid flow through the microbead-containing reservoirs. The airflow channels are then connected to the main microchannels to control the flow, allowing for optimum reagent/analyte mixing and reaction time. One attractive feature in microfluidic system is that their fabrication techniques are compatible with those already used in standard semiconductor batch-processing [11].

The other interesting area of development in microfluidic system is dielectric property measuring system from which information such as conductivity and permittivity of MUT (Material Under Test) is obtained. The detection principle of conductivity and permittivity of MUT is based on capacitively coupling the excitation signal produced by IDC (Inter-digital Capacitor) electrodes. Mamishev et al. define the interdigital capacitor electrode as a digitlike or fingerlike periodic pattern of parallel in-plane electrode used to build up the capacitance associated with the electric fields that penetrate into the MUT [12]. The IDC sensor operates in a way that is very similar to a conventional parallel plate capacitor. Figure 1.2 shows the schematic diagram of interdigital capacitor electrodes which help to visualize the transition from a parallel plate capacitor to a fringing field sensor.

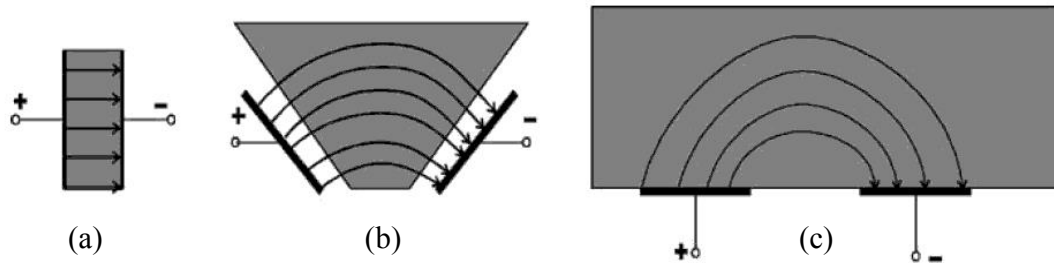


Figure 1.2: A fringing field interdigital capacitor electrodes can be visualized as: (a) a parallel-plate capacitor whose (b) electrodes open up to provide (c) a one-sided access to the MUT [12].

It is clearly shown in Figure 1.2 that the electric field lines always penetrate into the bulk of MUT regardless of the position of electrodes (parallel or coplanar). Depending on the geometric configuration of the electrodes the electric field lines can penetrate deeper with wider electrode configuration. Therefore, the capacitance of the IDC sensor always depends on the dielectric property of MUT and geometry of the electrodes. Note that the measured fringing field capacitance is usually considerably low so the electrode pattern needs to be repeated several times in order to strengthen the measured signal.

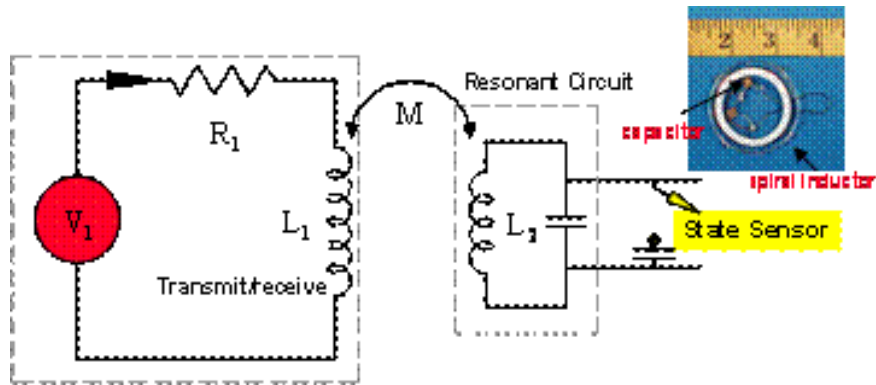
Among the widespread applications of IDC such as SAWs (Surface Acoustic Waves) for consumer electronics and telecommunication applications [13], microwave integrated circuits [14-16], and biochemical sensors for DNA detection [17-19], capacitive chemical sensors [20-23] constitute a major portion of all IDC sensors. Typically, a chemically sensitive layer is deposited on top of IDC electrodes in order to detect various gases, chemicals, moisture, organic impurities, etc. When the sensitive

layer (usually a polymer) interacts with the chemicals present in the MUT, the layer changes its conductivity (σ), dielectric constant (ϵ), and the effective thickness (h) of the layer. The IDC chemical sensor then detects the change in capacitance due to the change of dielectric constant and the thickness of the layer. The IDC chemical sensor has been investigated by many researchers because they are cheap to manufacture and can be easily integrated with other sensing components and signal processing electronics [12].

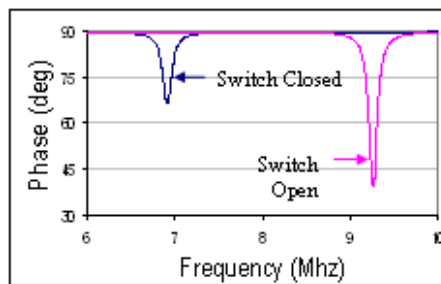
This dissertation presents the design, fabrication, and testing of an IDC electrode sensor for a dielectric property measuring component that can be integrated into a microfluidic system. Unlike the conventional chemical sensors described previously this IDC sensor detects directly the conductivity and permittivity of aqueous solutions on the microfluidic chip. This IDC sensor also has a polymer insulation layer on top of the electrodes, but it is not chemically sensitive to the MUT. One practical point of this research is the analytical evaluation of the interdigital electrode capacitance for the detection of conductivity and permittivity of aqueous solutions, which is not apparently analyzed in other chemical sensor applications.

In addition to the analytical evaluation of the IDC sensor for the direct measurement, a new novel methodology of remotely accessing the IDC sensor by wireless inductive coupling similar to EAS (Electronic Article Surveillance) tags is presented. Our group has been working with the civil engineering department at the University of Texas at Austin on the development and analysis of a passive wireless ESS (Electronic Structural Surveillance) sensor platform for structural health monitoring [24,25]. The general concept of the sensor system is to develop a small, inexpensive, and self-contained sensor which would be embedded in the concrete of the structure the sensor is monitoring. The sensor is an inductive coil of wire which is magnetically

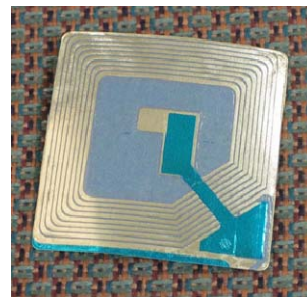
coupled to a remote reader coil outside of the concrete. Figure 1.3 shows an illustration of the electronic structural surveillance tag sensor.



(a)



(b)



(c)

Figure 1.3: Electronic structural surveillance tag: (a) reader and sensor circuit diagram, (b) resonant frequency of the sensor based on the state, and (c) commercial EAS (Electronics Article Surveillance) tag [24].

In chapter 2 initial works regarding the airflow-controlled multi-channel microfluidic system and various other MEMS based microfluidic fabrication technologies are explained.

Chapter 3 explains mainly about dielectric property measuring IDC sensor design. First, brief history and basic theory of dielectric spectroscopy are presented. Then, the design of the IDC sensor is explained more in depth using conformal mapping techniques and its dependence on the geometric configuration of the IDC electrodes. Verification of this analytical model with the measured data is also presented.

In chapter 4 two different measurement techniques are presented: impedance measurement with z-probe and impedance analyzer. For each technique experimental results are shown and explained.

Chapter 5 presents detection mechanism of direct measurement. In this chapter several different equivalent circuit models of IDC sensor are presented. In addition, a new analytical evaluation method is proposed and evaluated for the actual measurement data analysis. This method is verified with extraction of dielectric properties of known materials and dielectric properties of truly unknown materials are tested as well.

Chapter 6 presents detection mechanism of wireless measurement. Background and basic circuit theory of RFID-type readout are explained. The detection mechanism of the wireless system is also explained along with experimental results.

Chapter 2: Initial Works of Microfluidic System

2.1 TOP AND BOTTOM CHANNEL INCORPORATED MICROFLUIDIC SYSTEM

One practical advantage of microfluidic system is cost. Obviously, microfluidic system is very cost effective because reagent consumption is very low and lithographic procedures provide mass production of identical chips. In “Electronic Tongue” system analyte consumption is relatively high because flood delivery system of sample solutions generates high dead volumes. Even though the sensor array chips are sealed within a customized flow cell designed to minimize exchange volume of samples, the unused and wasted sample volumes are relatively high. Therefore, top and bottom channels incorporated microfluidic system is developed in order to reduce the initial sample volume and usage of expensive reagents and increase functionality.

Figure 2.1 illustrates the top and bottom channels incorporated microfluidic system. The advantage of this design is that analyte solutions are delivered to the reservoirs only through the channels minimizing the usage of solutions. In addition, top and bottom channels still provide large effective sensing area by allowing flow through the system. Fluid solutions are delivered from reservoirs containing reagent source microbeads to “downstream” reservoirs containing detector microbeads.

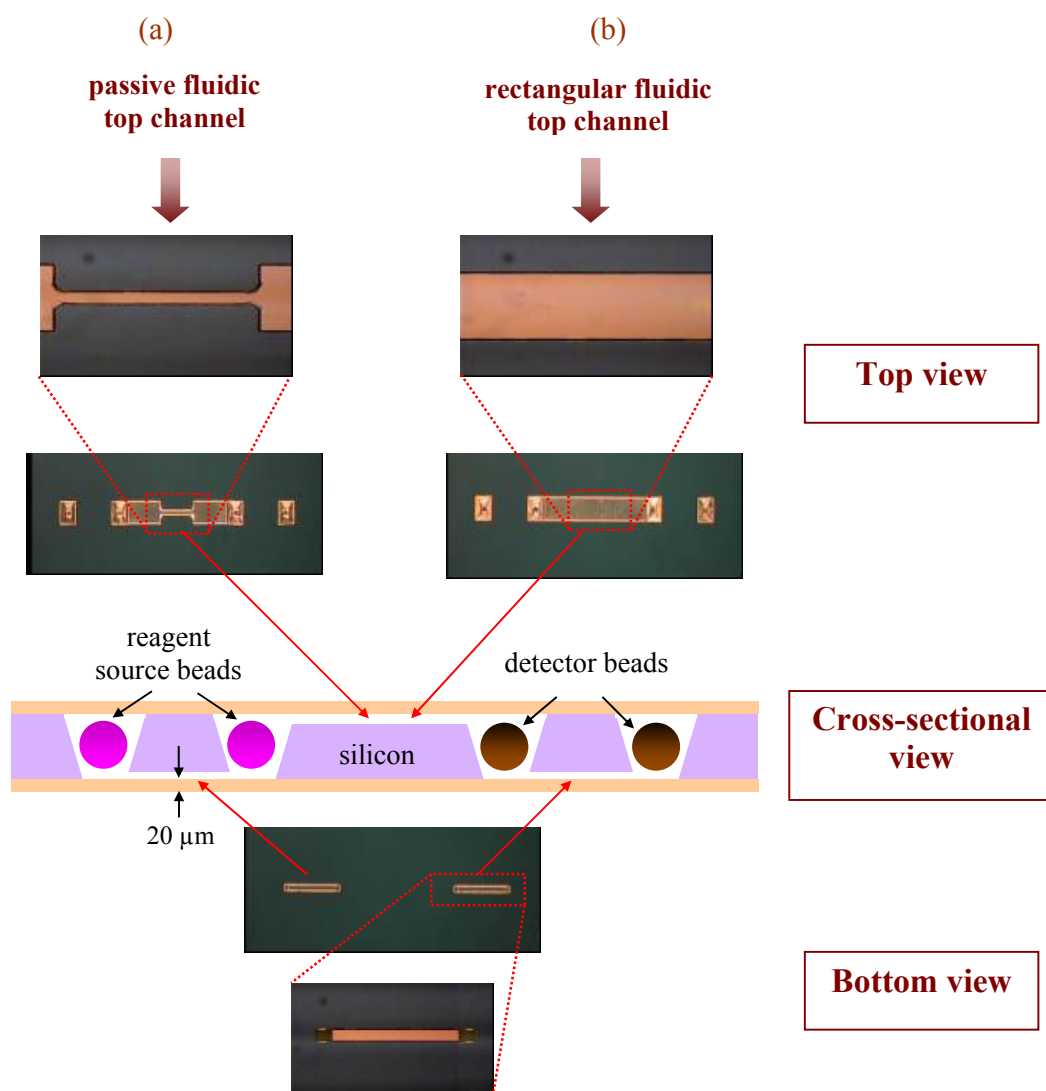


Figure 2.1: Illustration of a top and bottom channel incorporated microfluidic system with (a) passive fluidic top channel and (b) rectangular fluidic top channel.

A noble feature of this design is the ability to control the fluid speed and reaction time by incorporating a passive valve in the top channel as illustrated in Figure 2.1. In order to test the controllability of the fluid, two different kinds of top channels are designed: a simple rectangular channel and a passive valve channel. In a passive valve channel, the channel cross-section varies from wider to the narrower in order to stop fluid passively due to the pressure difference. It is passive because fluid is stopped without any outside control. This constricted flow is used to control chemical reaction times as the fluid passes through the reagent microbead reservoirs to the downstream detector microbead reservoirs.

PDMS (Polydimethylsiloxane) polymer material is used for the cover layer instead of rigid glass cover. PDMS provides several major advantages that are not immediately available in traditional fluidic circuit material such as glass. Advantages are bio and chemical compatibility, ease of processing using micromolding techniques, adjustable stiffness and surface adhesion energy, and transparency at least within the visible spectrum [26]. Another advantage of using PDMS is the ease of integration of fluid delivery tubing. The elastic property of PDMS material allows the ease of insertion of tubing without any special drilling tool.

PDMS layer is prepared by mixing two materials: prepolymer and curing agent (Sygard 184) on a flat surface container. Typically, 10:1 mixture of prepolymer and curing agent respectively is used but the ratio can be adjusted in order to change the stiffness of PDMS material. For example, if the ratio of curing agent is increased, the stiffness of the material increases as well. The mixture is placed in vacuum chamber for an hour to remove air bubbles that are introduced during mixing. Then, the mixture is hardened in oven at 70 °C for about 8 hours. After the curing process, PDMS is easily peeled off from the surface and then applied on the surfaces of the microfluidic chip.

Figure 2.2 illustrates the schematic drawing of the complete microfluidic test system with fluid delivery tubing. The performance of the system is tested with visible fluid sample. The sample is injected through the inlet delivery tubing and drained out to outlet tubing. Figure 2.3 shows the movie frames about testing of fluid sample passing through the top and bottom microchannels through the delivery tubing. The performance of the test demonstrates the fluid flow through the top and bottom channel without failure. One important thing to note in this experiment is the functionality of the passive valve of the top channel. In the design stage, we predicted that the channel cross-section variation from wider to narrower would stop fluid passively due to the pressure difference. As an experimental result, the top channel design worked in a proper way that we had to apply pressure to continue the fluid flow, and otherwise fluid was immobile.

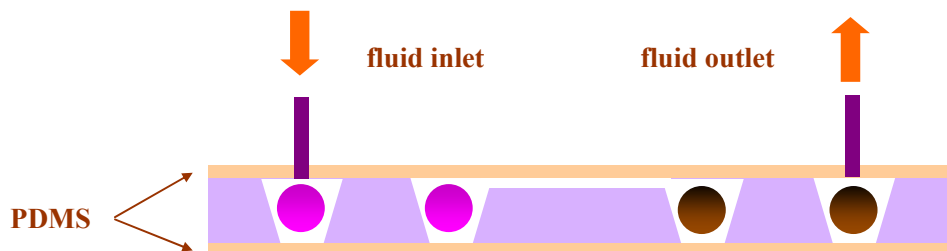
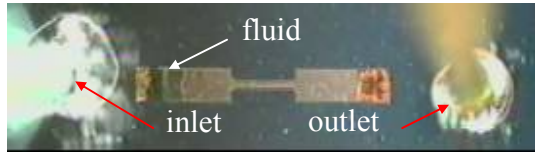


Figure 2.2: Schematic drawing of the complete microfluidic test system with fluid delivery tubing.



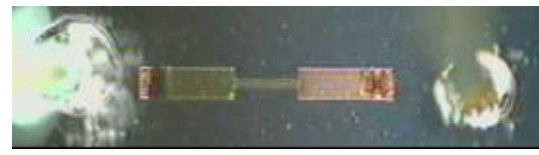
a. Initial stage of the visible fluid



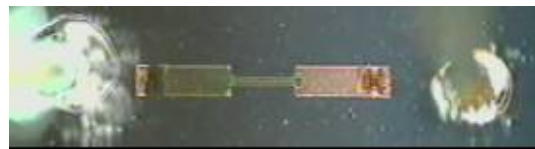
b. Before entering narrow part of the top channel



c. Visible fluid through the narrow channel



d. Visible fluid at the end of the narrow channel



e. Visible fluid entering wide part of the channel



f. Visible fluid In the middle of the wide channel



g. Visible fluid at the end of the wide channel



h. Visible fluid coming out through the outlet

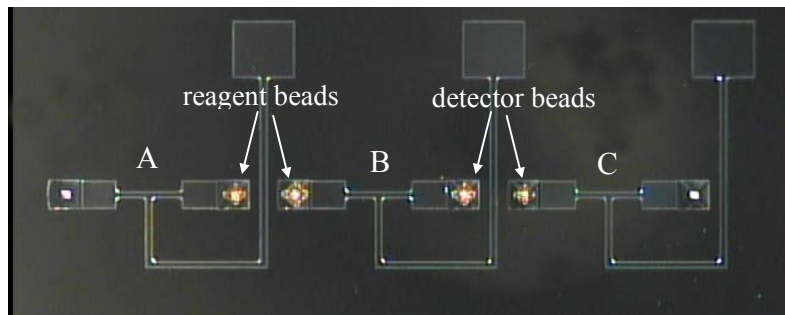
Figure 2.3: Captured movie frames showing fluid sample passing through the channel.

2.2 AIRFLOW CHANNEL INCORPORATED MICROFLUIDIC SYSTEM

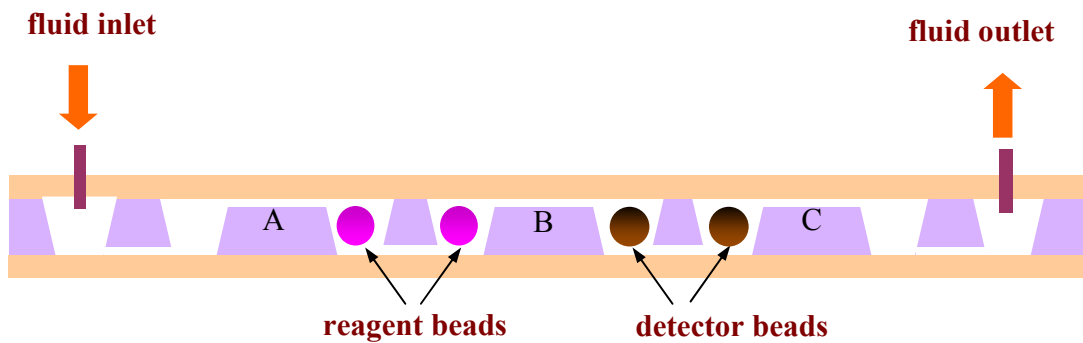
The motivation behind the airflow channel incorporated microfluidic system is to improve and enhance a drawback of the top and bottom channel system from the previous chapter. The structure of the previous system could have deficiencies of reliability for certain chemical sensing applications. For example, when analyte solution enters to the reagent source bead reservoir, it reacts with the reagent sensor bead while it is passively stopped at the neck of the top channel. After some reaction time, when the solution is transported downstream to the detector bead reservoir, a substantially time varying concentration of reagent would produce in the detector bead reservoir. Therefore, in order to enhance reliability of the system and minimize the problem described above, an airflow channels is connected to the top channel. Figure 2.4 shows the schematic drawing and picture of the system.

Three airflow channels (A, B, and C) are connected to the neck of each top channel to test the feasibility of the airflow channel. Referring to Figure 2.4, when fluid is injected to the reagent source bead reservoirs, the fluid stops passively at B while it reacts with the reagent source beads. At the same time, the problem of diffusion of the reacted fluid back to the dummy reservoirs is minimized due to another passive stop channel at A. After sufficient reaction time, airflow at A is initiated. In this case, only reacted fluid from the reagent source bead reservoirs is transported to the detector bead reservoirs and it stops again at C. Finally, airflow at B is initiated to remove fluid from the detector bead reservoirs to the outlet tubing. Figure 2.5 shows several extracted movie frames from recorded video that demonstrates the performance of the airflow channel by transporting fluid from reservoir to reservoir. Note that when fluid sample enters the second top channel, a small amount of the sample also flows partially into the airflow channel as shown in Figure 2.5 (c) and (d). After the second top channel is completely filled with

fluid sample, air pressure is applied to the airflow channel (e). As expected, the airflow removes the fluid sample from the top channel (g).

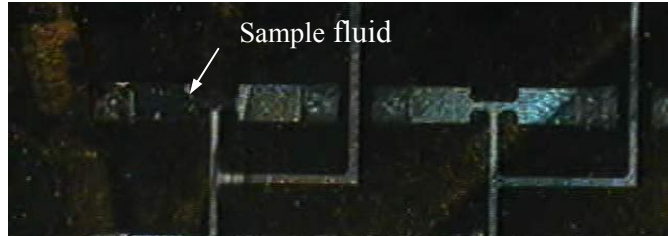


(a)

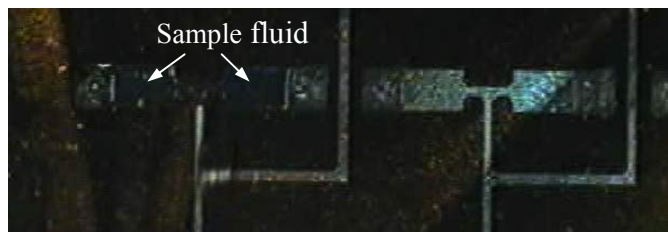


(b)

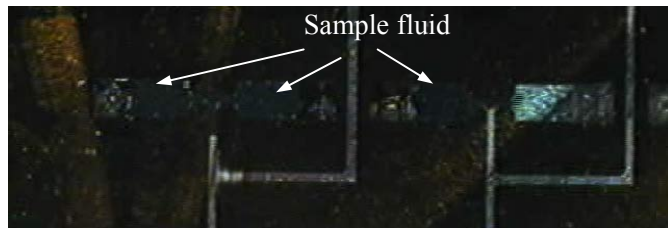
Figure 2.4: Schematic design of airflow incorporated microfluidic system: (a) picture of top view of the system and (b) cross-sectional view of the system.



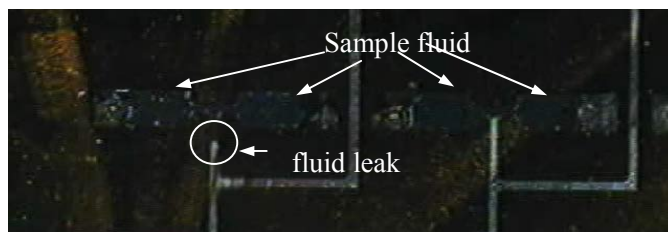
(a) Sample fluid starts



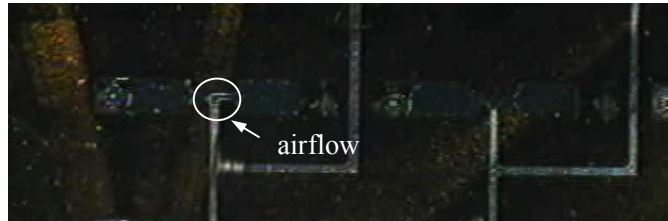
(b) Sample fluid is filled in the first top channel



(c) Sample fluid is half-filled in the second top channel



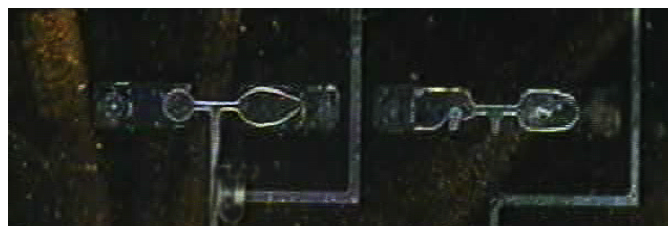
(d) Sample fluid is filled in the second top channel



(e) Initiates airflow



(f) Airflow enters the top channel



(g) Airflow removes sample fluid from the top channels

Figure 2.5: Extracted movie frames showing performance of airflow incorporated microfluidic system.

2.3 SU-8 GASKET DESIGN

One critical requirement for the complete operation of microfluidic system is a compact package that connects the chip to the outside environment. To facilitate such connections between our microfluidic chip and a conventionally machined fluidic interface high quality, very small, and compliant gaskets are needed. Our primary progress has been in this area. We use SU-8 series supplied by the Microlithography Chemical Co. as the material to form integrated gaskets. SU-8 is epoxy based negative photoresist with high functionality, high optical transparency and are sensitive to near UV radiation. At the near-UV wavelengths from 365 to 436 nm the photoresist has very low optical absorption, which makes photolithography of thick films with high aspect ratios. Because of its simple fabrication processes and the good mechanical properties, SU-8 is used as structural material for many microfluidic applications [27].

Typically, the fabrication steps to build SU-8 structures of 100 μm start with two steps of resist spinning: spread cycle and spin cycle. Due to the high viscosity of the photoresist, low spin speed of 500 rpm for 10 seconds is needed to spread evenly. During the second step the spin speed ramps quickly up to 3000 rpm for about 30 seconds. The film thickness or SU-8 structure height is determined by the viscosity of the photoresist and the spin speed. Higher viscosity or lower spin speed results in a thicker resist film. After the resist is applied onto the substrate, a soft bake is performed on a hot plate to evaporate the solvent and densify the film. Ramping or stepping the soft bake temperature is used for better film quality. The standard soft bake process is 5 minutes at 65°C and 20 minutes at 95°C. After the soft bake, the SU-8 is optimized for near-UV exposure. Recommended exposure energy for the target thickness of 100 μm is 240mJ/cm². Following the exposure, PEB (Post Exposure Bake) must be performed to selectively cross-ling the exposed portions of the photoresist. Again, a slow ramp is

recommended to minimize resist stress. In general, PEB of 1 minute at 65°C and 10 minutes at 95°C is used for the target thickness. Finally, the SU-8 is developed for about 15 minutes with strong agitation for high aspect ratio and thick film structure. Table 2.1 gives an example of different SU-8 types with different fabrication process parameters as a reference.

SU8 types / Thickness (μm)		Spin speed (rpm)	Soft bake times (min)		Exposure energy (mJ/cm^2)	PEB (min)		Development (min)
			65°C	95°C		65°C	95°C	
SU8 2002	2	3000	0	1	80	0	2	1
	2.4	2000	0	1	85	0	2	1
SU8 2050	50	3000	0	6	160	1	6	5
	80	2000	3	9	215	2	7	7
SU8 2100	100	3000	5	20	240	5	10	10
	200	1500	6	35	310	5	15	17

Table 2.1: Fabrication process parameters for different SU-8 types.

SU-8 gaskets are fabricated and tested on both silicon and glass substrates. Both silicon and glass substrates are sandwiched together and housed in a Plexiglas package to form the fluid flowing channel as shown in Figure 2.6. In this microfluidic system, SU-8 serves as both a sealing gasket to the external plastic package as well as defining on-chip fluid channels. SU-8 gasket on the glass substrate forms the bottom channel with the

silicon wafer and SU-8 gasket on the silicon wafer with Plexiglas cover forms the closed top channel.

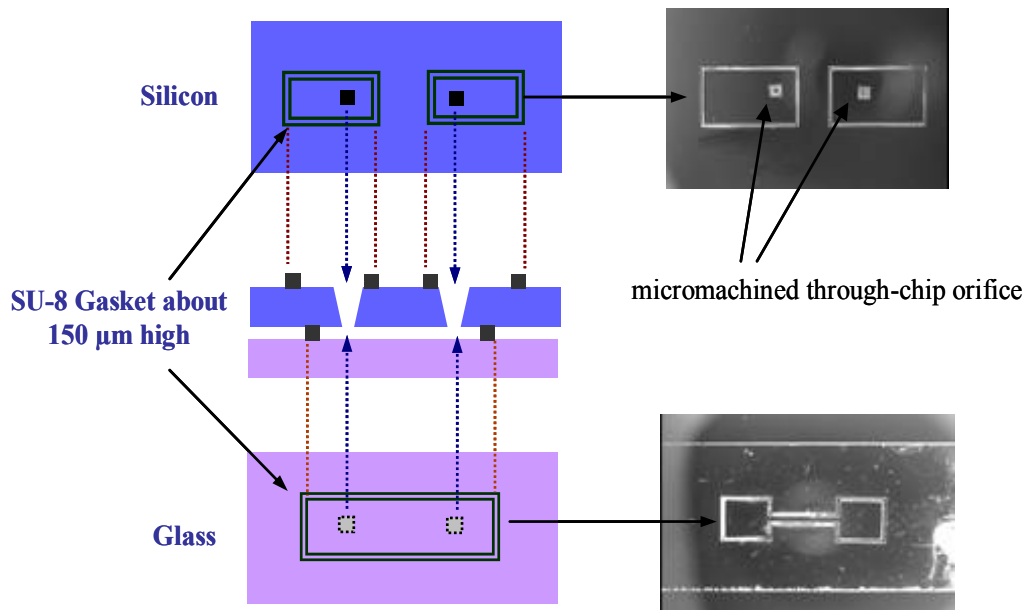


Figure 2.6: Schematic drawing of a SU-8 gasket/channel microfluidic system.

Figure 2.7 shows the SU-8 gasket/channel microfluidic system with the Plexiglas package with pipe-threaded fluid inlet and outlet. Since the depth of the cavity inside the Plexiglas housing is carefully calculated based on the thicknesses of the substrates and SU-8 height, glass and silicon substrates need not be first bonded together in order to provide sealed fluidic channels; instead the clamping action provided by the Plexiglas housing is sufficient to cause compression of the SU-8 gasket providing excellent fluid sealing.

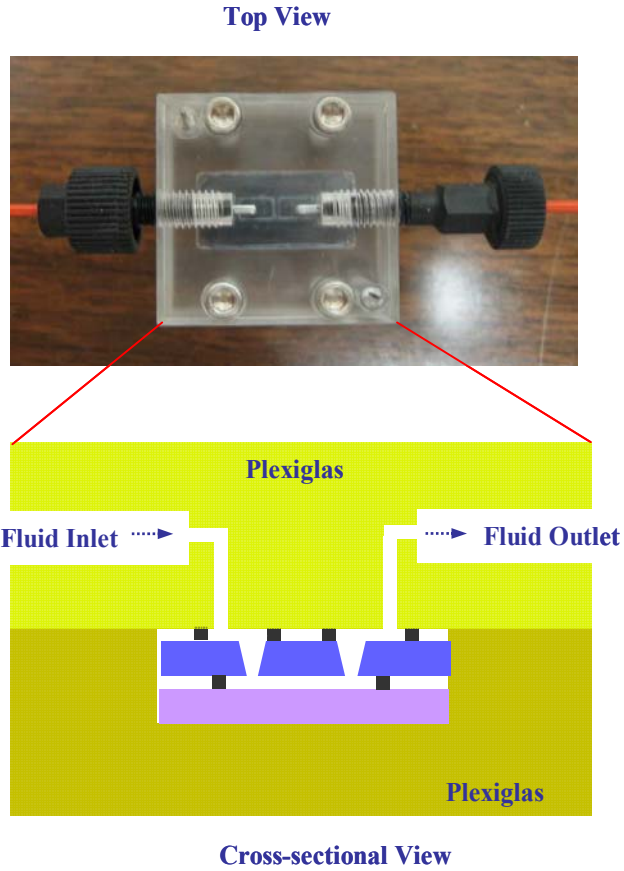
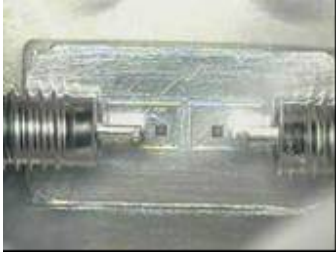
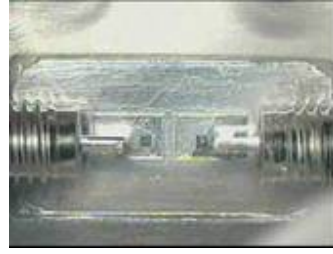


Figure 2.7: Top and cross-sectional view of the experimental system.

SU-8 gasket performance is tested with flowing DI water through silicone tubes which are connected between a syringe pump and the Plexiglas packaged fluidic chip. Frames from a captured movie as DI water is pumped through the system are shown in Figure 2.8. The pictures clearly demonstrate that the SU-8 serves successfully for both gasket and fluidic channel applications.



(a) Initial stage of the experimental system.



(b) DI water is entering top right SU-8 gasket defined channel.



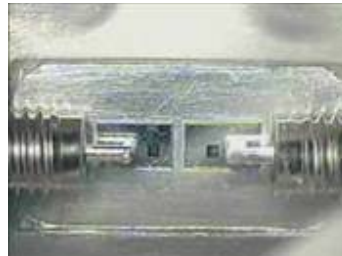
(c) DI water fills completely within the top right SU-8 gasket channel.



(d) DI water passes through the bottom SU-8 gasket channel under the chip and begins entering the top left SU-8 gasket channel.



(e) DI water spreads out the top left SU-8 gasket channel.



(f) DI water fills completely the top left SU-8 gasket channel.

Figure 2.8: Captured movie frames showing DI water passing through SU-8 gasket/channels.

2.4 SIMPLE DIRECT VOLUMETRIC MEASURING SYSTEM

Unlike other flow control transducers which depend on the voltage difference or pressure difference, a simple direct volumetric measuring system is designed. There are several advantages of this system over other existing flow monitoring devices. First, it provides direct measurement. Simply observing the volumetrically predefined reservoirs connected at the end of the fluidic channel as shown in Figure 2.9, information about the target volume transportation to the detector reservoir can be obtained. Second, the system is relatively easy to build in terms of fabrication process point of view, as it does not require any electrical connections. Third, the system is independent of the fluid properties.

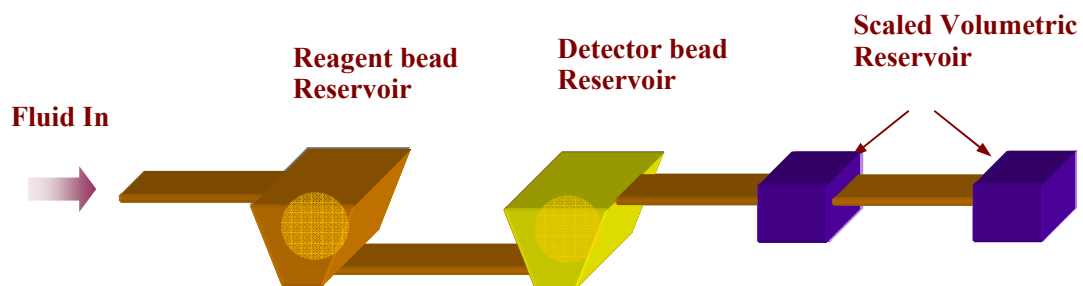


Figure 2.9: Illustration of the basic principle of the simple direct volumetric measuring system.

Volumetrically predefined reservoirs are attached at the end of the fluidic channel. Since the fluid volume in each reservoir and channel are known, it is possible to calculate how much of the fluid volume must be removed from the system in order for the target volume to be transported into the detector reservoir. Figure 2.10 shows the schematic diagram of the direct volumetric system.

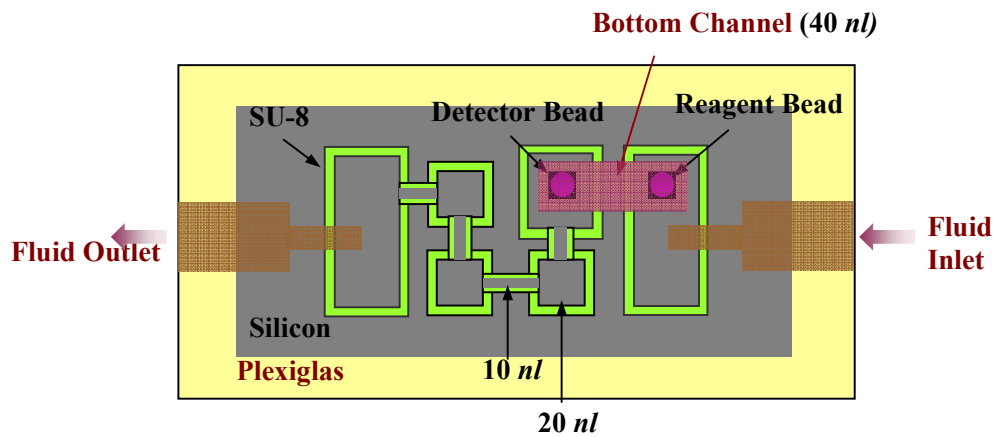
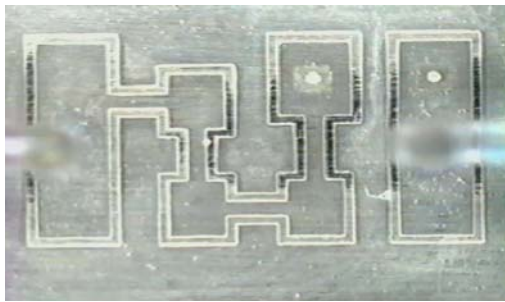
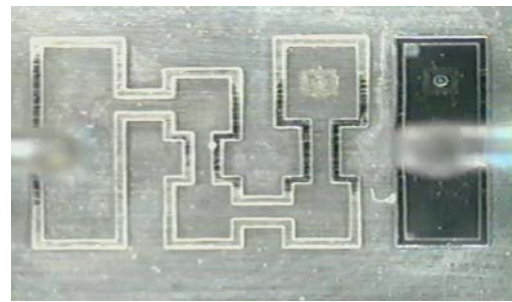


Figure 2.10: Schematic diagram of a simple direct volumetric measuring system.

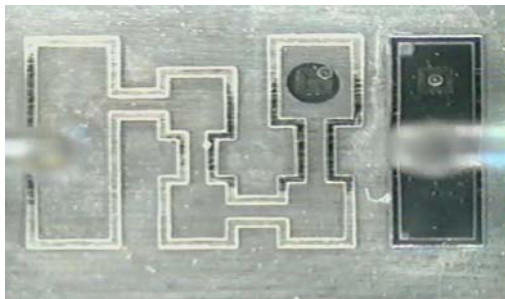
The top and bottom channels are made of SU-8 material. As Figure 2.10 indicates that the bottom channel is designed for a volume of 40 *nl* and each scaled reservoir and connector is 20 *nl* and 10 *nl* respectively. Knowing that the fluid flow is laminar and the volume of the bead reservoirs is 20 *nl*, it is predicted that the reacted fluid is transported into the detector reservoir if the fluid is filled through the second scaled reservoir connector, of which volume is 60 *nl*. Figure 2.11 shows captured movie frames as DI water is pumped through the system.



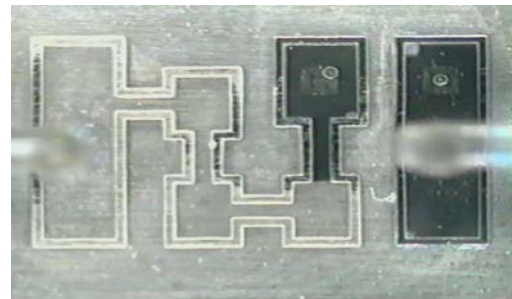
a. Initial stage of the experimental system



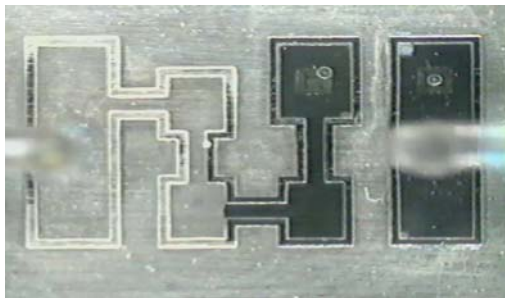
b. DI water fills completely within right SU-8 channel



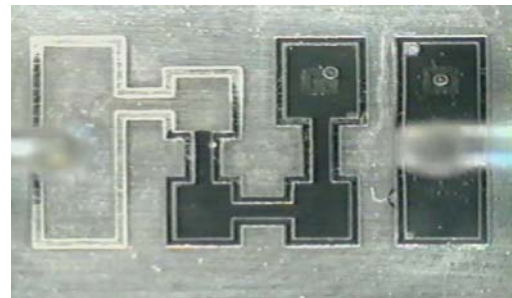
c. DI water starts to fill the detector bead containing SU-8 channel



d. DI water fills completely detector bead containing SU-8 channel



e. DI water fills the first VMS reservoir



f. DI water fills the second VMS reservoir

Figure 2.11: Captured movie frames showing DI water passing through the SU-8 simple direct volumetric measuring system.

Chapter 3: Measuring Dielectric Properties of Liquids

3.1 INTRODUCTION

One interesting area of development in microfluidic system is to build a chemical transducer component which can detect conductivity and dielectric constant of fluids flowing in the system. This particular component is very attractive as to it is inexpensive to fabricate and can be easily integrated with other sensing components for the lab-on-a-chip application. The most popular and widely employed technique for the dielectric property measurement is impedance spectroscopy.

Impedance spectroscopy is an electrochemical technique and a very powerful method of characterizing many intrinsic electrical properties of materials and their interfaces [28]. The theoretical basis of impedance spectroscopy is based on the analysis of the impedance of the system to be observed with respect to the applied frequency and exciting signal. The first impedance spectroscopy technique was introduced by Nernst in 1894 for measurement of the dielectric constants for aqueous electrolytes and different organic fluids using Wheatstone electrical bridge [29]. Since then, the idea of impedance spectroscopy has been employed by other researchers in many fields of science and technology such as biochemical and medical applications, as the analysis of impedance spectroscopy provides quantitative information about the conductance, the dielectric constant, and the static properties of the interfaces of a system [30].

Over the last decade, impedance spectroscopy has been a very useful tool in biochips combined with microfluidics, micromachining, and MEMS technologies. For example, impedance spectroscopy technique is used for microfluidic device for identification and characterization of cell in suspensions [31], interdigitated ITO immunosensor for detection of *E. coli* [32], Pt electrode array for detection of bovine

chromaffin cells [33], and microfluidic capillary electrophoresis system for conductivity detection applications [34-37].

Furthermore, the detection of dielectric properties of materials based on impedance spectroscopy has been a potential application in bio and chemical sensors. The detection principle is based on capacitively coupling the excitation signal produced by planar electrodes such as IDC with material. As the dielectric properties of a material are unique, such detection can be related to other physical properties of the material: bulk density, moisture content, chemical reaction, concentration, etc. For example, the amount of water in a solution can be determined by measuring the material's permittivity or if the molecular structure of a material changes due to a chemical reaction, its permittivity changes as well.

As understanding of impedance spectroscopy requires basic knowledge of dielectric properties of materials, a through review of related theory is presented in the next section.

3.2 THEORY

3.2.1 Debye dielectric model

The Debye dielectric relaxation model [38] has been a very useful tool for investigating the electrical and electrochemical properties of materials. The model is characterized with a single time constant to define the analogies between circuit elements and electrochemical processes. The relationship between the applied electric field and polar material is derived from basic laws of polarization and conduction using the following argument [28].

An electric field can interact with a polar or dielectric material in two principal ways: the reorientation of the complex defects with dipole moments and the translative motion of charge carriers such as vacancies and ionic interstitials. The resulting current density in the dielectric material due to the interactions is equal to

$$\vec{J} = \sigma \vec{E} + \frac{\partial \vec{D}}{\partial t} \quad (3.1)$$

where E is the electric field, σ is real (dc) conductivity, and D is the electric displacement. D is also defined as the total charge density on the electrodes and is given by

$$\vec{D} = \varepsilon_0 \vec{E} + \vec{P} \quad (3.2)$$

where ε_0 is the permittivity of free space and P is the polarization of the dielectric material.

When an electric field E is applied to a dielectric material, the resulting polarization P consists of two parts: instantaneous polarization and time dependent polarization. The instantaneous polarization due to the displacement of electrons with respect to the nuclei determines the high frequency dielectric constant ε_∞ as

$$\varepsilon_\infty - 1 = \frac{\vec{P}_\infty}{\varepsilon_0 \vec{E}} \quad (3.3)$$

The time dependent polarization P' is due to the reorientation of dipoles in the electric field. If the field remains in place for an infinitely long time, the resulting total polarization defines the static dielectric constant ε_s as

$$\epsilon_s - 1 = \frac{\vec{P}_s}{\epsilon_0 \vec{E}} \quad (3.4)$$

Thus, the resulting total polarization P_s can be rewritten as

$$\vec{P}_s = \vec{P}_\infty + \vec{P}'(t = \infty) \quad (3.5)$$

Assuming that the time dependent polarization P' is governed by first-order kinetics with a relaxation time τ , then the rate at which P approaches P_s is proportional to the difference between them. That is expressed as

$$\frac{d \vec{P}'(t)}{dt} = \frac{\vec{P}_s - \vec{P}}{\tau} \quad (3.6)$$

If a unit step voltage $u_0(t)$ is applied, then

$$\vec{P} = \vec{P}_\infty u_0(t) + \vec{P}' \quad (3.7)$$

And if we take the Laplace transforms of (3.6) and (3.7) and solve for the Laplace transform of polarization $\{P\}$, then

$$\left\{ \vec{P} \right\} = \frac{\vec{P}_\infty}{\left(p + \frac{1}{\tau} \right)} + \frac{\vec{P}_s}{\tau p \left(p + \frac{1}{\tau} \right)} \quad (3.8)$$

where p is the complex frequency variable. From (3.8), one can derive the expression for polarization as

$$\vec{P} = \frac{\vec{P}_s + j\omega\tau \vec{P}_\infty}{j\omega\tau + 1} \quad (3.9)$$

From (3.1), the displacement current density with conductivity of zero is defined as

$$J(t) = \vec{P}_\infty \delta(t) + (\vec{P}_s - \vec{P}_\infty) \frac{e^{-t/\tau}}{\tau} \quad (3.10)$$

This result corresponds exactly same to the response of the Debye equivalent circuit shown in Figure 3.1 with the lumped circuit elements:

$$\tau = RC_2 \quad (3.11.a)$$

$$C_2 = (\varepsilon_s - \varepsilon_\infty) \varepsilon_0 \quad (3.11.b)$$

$$C_1 = \varepsilon_\infty \varepsilon_0 \quad (3.11.c)$$

The admittance due to the relaxation process is, since $\{E\}=1/p$,

$$Y^* = \frac{\{J\}}{\{E\}} = \varepsilon_\infty \varepsilon_0 p + (\varepsilon_s - \varepsilon_\infty) \varepsilon_0 \frac{\omega_0 p}{(p + \omega_0)} \quad (3.12)$$

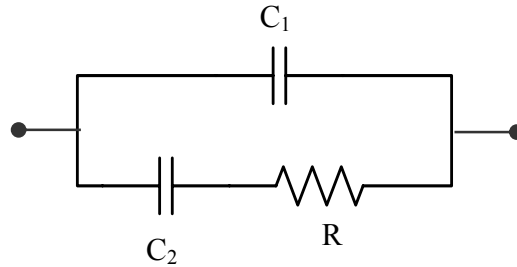


Figure 3.1: the Debye equivalent circuit model [39].

Separating the real and imaginary parts of (3.12) and substituting with $p=j\omega$, we obtain

$$Y^* = \frac{\omega^2 RC_2}{1 + \omega^2 R^2 C_2^2} + j \frac{\omega C_2}{1 + \omega^2 R^2 C_2^2} + j\omega C_1 \quad (3.13)$$

Therefore, since $\varepsilon^*=Y^*/j\omega\varepsilon_0$, the complex dielectric constant ε^* can be obtained from (3.13) as

$$\varepsilon^* - \varepsilon_\infty = \frac{\varepsilon_s - \varepsilon_\infty}{1 + \omega^2 \tau^2} - j \frac{\omega \tau (\varepsilon_s - \varepsilon_\infty)}{1 + \omega^2 \tau^2} \quad (3.14)$$

The real and imaginary parts of this equation are the Debye dispersion relations.

Note that even when the conductivity of a material is zero, its complex dielectric permittivity may have a non-zero imaginary part. The non-zero imaginary part is responsible for the energy dissipation process due to dipole re-orientation and translational motion of charge carriers [39].

3.2.2 Dielectric spectroscopy

All dielectric materials have an arrangement of electric charge carriers. These charges are displaced by an external electric field and polarized to neutralize the effect of the external electric field. This dielectric response of each dielectric material over the frequency spectrum is unique characteristic for each material. The study of this dielectric response over frequency spectrum is known as dielectric spectroscopy [40].

Recall that the dielectric response of a material is represented in terms of its complex dielectric permittivity ε^* and it is given as $\varepsilon^* = \varepsilon' - j \varepsilon''$. The real part of permittivity ε' is called dielectric constant and is a measure of energy stored from an

external electric field in a material. The imaginary part of permittivity ϵ'' is called the loss factor and is a measure of the energy loss to an external electric field. The loss factor is actually expressed as a function of both dielectric loss and conductivity and it is given as

$$\epsilon^* = \epsilon' - j\epsilon'' = \epsilon' - j\left(\epsilon_d'' + \frac{\sigma}{\omega}\right) \quad (3.15)$$

where ϵ_d'' is dielectric loss and σ is conductivity. In liquid material, ionic conductivity comprises of the overall conductivity over many other conduction mechanism at low frequency [40]. Sometimes the loss factor is expressed in terms of the ratio of the energy lost to the energy stored, which is called dissipation factor.

$$\tan \delta = \frac{\epsilon''}{\epsilon'} \quad (3.16)$$

Depending on their relaxation frequency $\sigma/\omega\epsilon$, a material falls into two categories: conductive material and dielectric material. In general, when $\sigma/\omega\epsilon \gg 1$, the material is considered as a good conductor or lossy material. Similarly, the material is considered dielectrics or low-loss material if $\sigma/\omega\epsilon \ll 1$.

Figure 3.2 illustrates how the dielectric properties of water vary with the frequency of the applied electric field. Water molecules are permanent dipoles and can follow the applied electric field at low frequencies, which results in maximum value of ϵ' or maximum energy stored. As the frequency increases the water molecules can no longer follow the changing electric field, which results in less energy stored and high rotational losses. At the critical frequency or relaxation frequency, the loss factor reaches its maximum value. As shown in Figure 3.2, dielectric constant of water rolls off around its relaxation frequency of about 22 GHz.

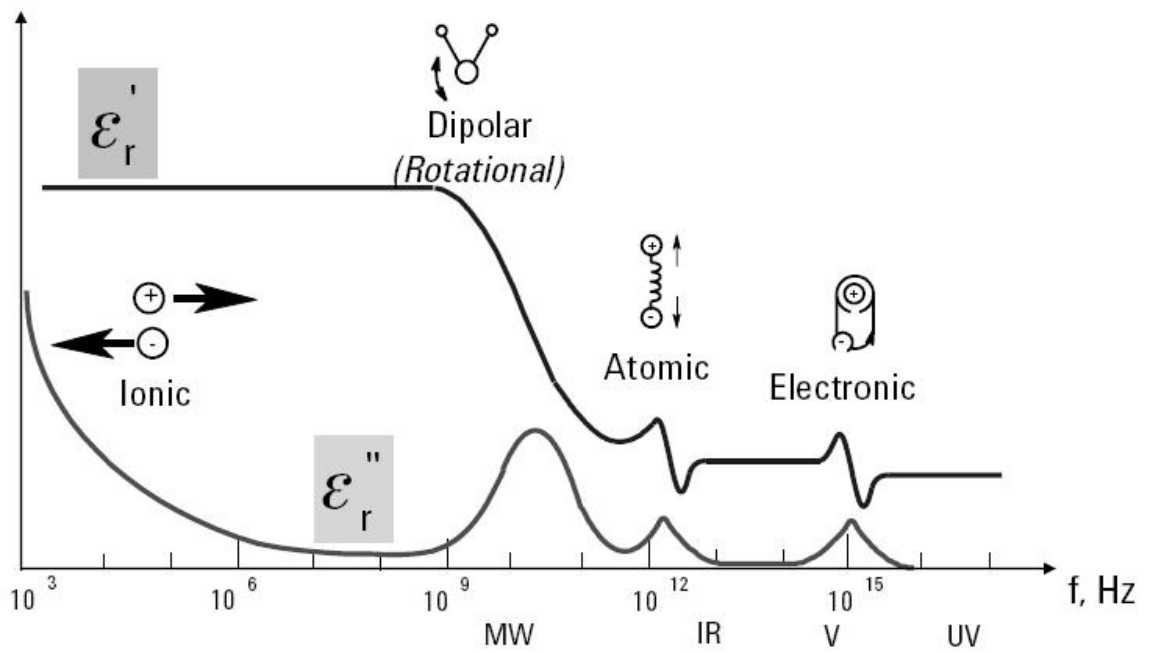


Figure 3.2: Dielectric mechanisms over a wide range of frequencies. Ionic and dipolar relaxation at lower frequencies (up to 100 MHz) and atomic and electronic resonances at higher frequencies are shown [40].

A compact and informative way of displaying the relationship between ϵ' and ϵ'' with frequency ω as the independent parameter is the Cole-Cole plot as shown in Figure 3.3 [40]. The method consists in plotting ϵ'' as a function of ϵ' and the locus points appears as a semicircle. If a material has a single relaxation frequency, the center of the semicircle lies on the horizontal axis, and otherwise, its center lies below the horizontal axis. As shown in the Cole-Cole plot, when a material has a single relaxation frequency, the maximum value of ϵ'' is equal to the radius of the semicircle $(\epsilon_s - \epsilon_\infty) / 2$ and it occurs at $1/\tau$.

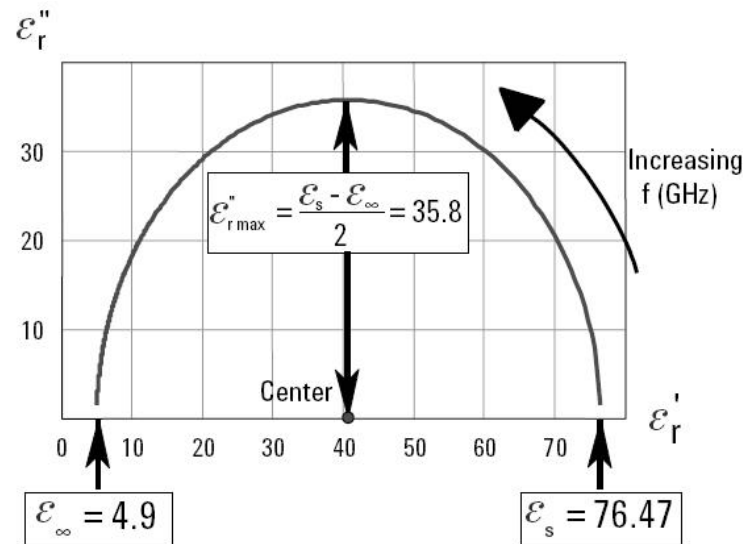


Figure 3.3: Cole-Cole diagram of dielectric properties of water [40].

3.3 INTERDIGITATED CAPACITOR (IDC) SENSOR DESIGN

3.3.1 Historical perspective

Interdigitated capacitor electrodes are among the most widely used periodic electrode structures for the chemical sensing applications due to the several advantages such as one-side access, control of signal strength, and simplification of modeling. The basic principle of IDC sensor relies on applying a spatially periodic fringing electric field into the material under test. The combination of this periodic fringing field with the excitation frequency provides the information about the dielectric spectroscopy of the material under test (MUT) [12].

A useful method for the calculation of the capacitance of IDC structures is conformal mapping technique. Conformal mapping technique provides closed form expressions for the computation of the capacitance of IDC electrodes based on the geometry and property of the sensor. In 1977 Wei first evaluated the capacitance of an IDC with an infinite top layer based on conformal mapping technique [41]. This model is developed and improved by Veyres and Hanna [42] to evaluate the capacitance for a sensor having a finite layer structure in 1980. Since then, the model used by Veyres et al. has played an important role in analyzing the IDC structure in a variety of scientific applications. In our lab, Wentworth et al. used the model to characterize the tape automated bonding (TAB) interconnect in 1989 [43]. In 1996 Gevorgian et al. [44] proposed a different model for an IDC with a multilayered top structure based on the same conformal mapping technique. The more general form of multilayered IDC electrodes is developed by Igreja in 2004 [45].

3.3.2 Analysis of IDC electrodes using conformal mapping techniques

3.3.2.1 IDC electrodes with infinitely thick air layer

A conformal mapping technique can be used to transform the coplanar line geometry into a parallel plate capacitor, for which the capacitance is a linear function of dielectric constant. Closed-form expressions for the coplanar line impedance characteristics and its effective dielectric constant are obtained in terms of finite dimensions. A cross section of coplanar strip line is shown in Figure 3.4.

Veyres and Hanna [42] assume that the total line capacity between the signal strip and the adjacent ground strip is the sum of the line capacity C_1 and C_2 , where C_1 is the line capacitance of coplanar strips with air layer above and below and C_2 is the capacitance of coplanar strips with the dielectric substrate layer present. For this reason, C_2 is calculated with a dielectric constant of $\epsilon_{sub}-1$, because this region is already included in the calculation of C_1 . This technique is so called partial capacitance technique. This technique is explained more in detail later in this section.

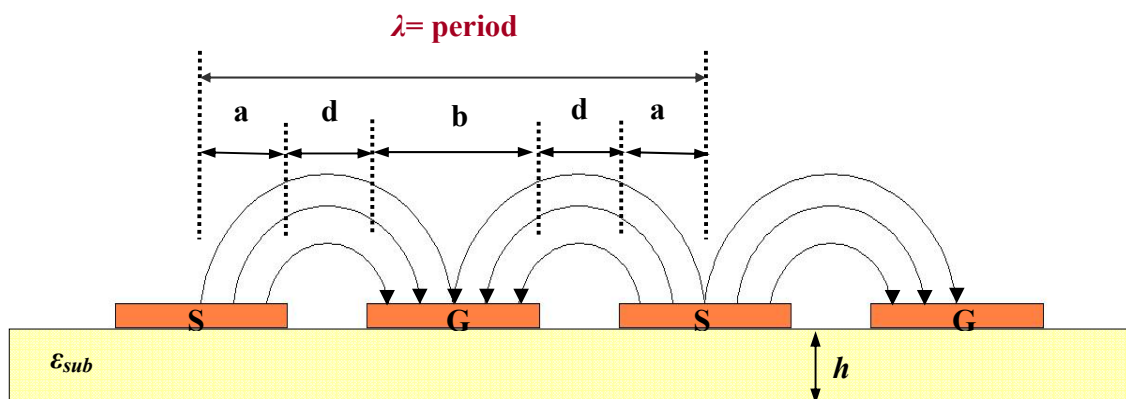


Figure 3.4: Cross-section view of coplanar strip line with fringing electric field [42].

The computation of the capacitance C_l involves two conformal maps: the first map translates the boundary layer of the coplanar line geometry in the x plane into the t plane, and the second map is from t plane into the rectangle in the z plane successively as shown in Figure 3.5. In this map, only lower right quadrant is considered and the final capacitance is multiplied by 4 to compute the total value of C_l . Note that the coplanar line thickness is not considered in this analysis.

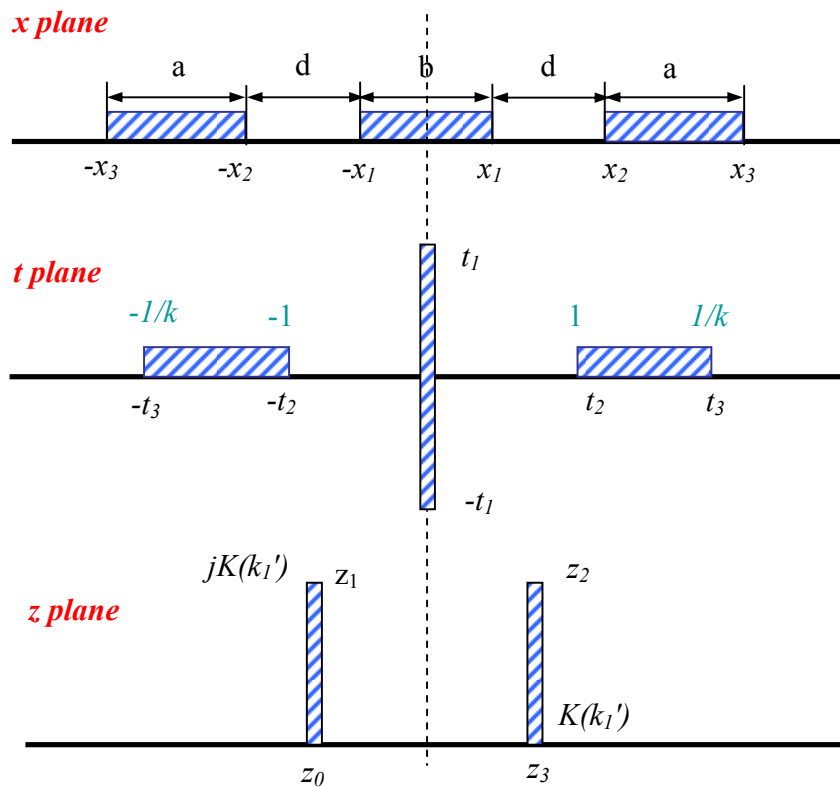


Figure 3.5: Conformal mapping transformations for the calculation of the line capacitance C_l in the absence of the dielectric substrate layer [42].

The boundary of x plane is mapped into the t plane using the mapping functions

$$\begin{cases} t = \frac{x}{x_3} \sqrt{\frac{x_3^2 - x_1^2}{x^2 - x_1^2}} & \text{for } |x| > |x_1| \\ t = j \frac{x}{x_3} \sqrt{\frac{x_3^2 - x_1^2}{x^2 - x_1^2}} & \text{for } |x| \leq |x_1| \end{cases} \quad (3.17)$$

where x_1 is the half-width of the center strip and x_3 is the distance from the middle of the center signal strip to the outside of an adjacent ground plane as shown in Figure 3.5. Therefore, the boundaries are defined as

$$x_1 = \frac{b}{2}, x_2 = \frac{b}{2} + d, \text{ and } x_3 = \frac{b}{2} + d + a \quad (3.18)$$

All of the coplanar strip lines in the lower quadrant of the x plane are mapped into the upper right quadrant of the t plane. Then, the map from the t plane to the z plane uses the Schwarz-Christoffel transformation [46]

$$z = \int_0^t \frac{dt}{\sqrt{(t_3^2 - t^2)(t_2^2 - t^2)}} \quad (3.19)$$

The mapping gives separation between the parallel plates in z plane as $K(k_1)$ where

$$k_1 = \frac{t_3}{t_2} = \frac{x_3}{x_2} \sqrt{\frac{x_2^2 - x_1^2}{x_3^2 - x_1^2}} \quad (3.20)$$

and x_2 is the distance from the middle of the center signal strip to the inside of the adjacent ground plane as shown in Figure 3.5.

Therefore, (3.20) can be rewritten as

$$k_1 = \left(1 + \frac{2a}{2d + b}\right) \sqrt{\frac{\left(1 + \frac{b}{d}\right)}{\left(1 + \frac{a}{d} + \frac{b}{d}\right)\left(1 + \frac{a}{d}\right)}} \quad (3.21)$$

The width of a plate is $K(k_1')$, where $k_1' = \sqrt{1 - k_1^2}$. $K(k_1)$ is the complete elliptical integral of the first kind with modulus k_1 , and $K(k_1') = K'(k_1)$.

The first capacitance of the coplanar strip lines with air layer only is therefore

$$C_1 = 4 \varepsilon_0 \frac{K(k_1')}{K(k_1)} \quad (3.22)$$

where $K(k_1')/K(k_1)$ is a ratio of complete elliptical integral of the first kind and ε_0 is the free space permittivity ($\varepsilon_0 = 8.85 \times 10^{-14} \text{ F/cm}$). The ratio of the integral can be estimated using Hilberg's approximation [47], which is given in general form as

$$\begin{aligned} \frac{K(k)}{K(k')} &\cong \frac{2}{\pi} \ln\left(2\sqrt{\frac{1+k}{1-k}}\right) && \text{for } 0.707 \leq k \leq 1 \\ \frac{K(k)}{K(k')} &\cong \frac{\pi/2}{\ln\left(2\sqrt{\frac{1+k'}{1-k'}}\right)} && \text{for } 0 \leq k \leq 0.707 \end{aligned} \quad (3.21)$$

Similarly, C_2 is calculated considering only lower right quadrant as before. The capacitance of this quadrant will be multiplied by 2 instead of 4, as C_2 accounts for the capacitance of the dielectric substrate layer which is located only in the lower two quadrants. Evaluation of C_2 first involves a conformal map to transform the finite-

thickness dielectric layer onto one that appears infinitely thick. This is accomplished using the hyperbolic sine function

$$p = \sinh\left(\frac{\pi x}{2h}\right) \quad (3.22)$$

to map the x plane into the p plane as shown in Figure 3.6.

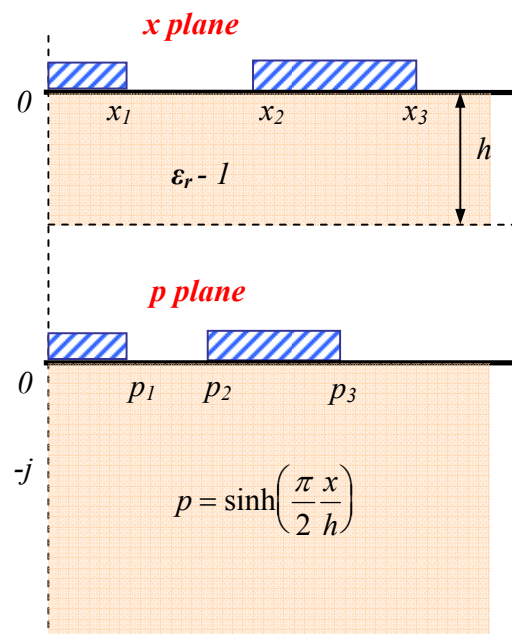


Figure 3.6: Conformal mapping transformations for the calculation of the line capacitance C_2 [42].

Then, the mapping proceeds exactly same as in the first case for C_1 , mapping from the p plane to the t plane using (3.17), and then to the z plane using the elliptical integral successively. The result for the second capacitance is given as

$$C_2 = 2\varepsilon_0(\varepsilon_{sub} - 1) \frac{K(k_2')}{K(k_2)} \quad (3.23)$$

where

$$k_2' = \frac{\sinh\left(\frac{\pi b}{4h}\right)}{\sinh\left[\frac{\pi}{2h}\left(\frac{b}{2} + d\right)\right]} \sqrt{\frac{\sinh^2\left[\frac{\pi}{2h}\left(\frac{b}{2} + d + a\right)\right] - \sinh^2\left[\frac{\pi}{2h}\left(\frac{b}{2} + d\right)\right]}{\sinh^2\left[\frac{\pi}{2h}\left(\frac{b}{2} + d + a\right)\right] - \sinh^2\left(\frac{\pi b}{4h}\right)}} \quad (3.24)$$

and $k_2 = \sqrt{1 - k_2'^2}$.

Therefore, total line capacity between the signal strip and the adjacent ground strips is

$$C_{total} = n \cdot l \cdot (C_1 + C_2) \quad (3.25)$$

where n is the number of IDC finger pairs or wavelength λ and l is the overlapping finger length.

3.3.2.2 IDC electrodes with an insulation layer

To measure the dielectric properties of aqueous materials, it is necessary to insulate the electrodes from the aqueous material in order to avoid any electrical or electrochemical interference. Therefore, the capacitance effect of the insulation layer must be taken into account when evaluating the impedance analysis of the IDC sensor.

The analytical evaluation of the capacitance of an insulation layer on top of the IDC electrodes is based on the same partial capacitance technique explained in the previous section. The capacitance of an insulation layer, C_3 , is evaluated again through

conformal mapping technique and the complete elliptical integral. The complete elliptical integral of an insulation layer based on the geometric parameters is given as

$$k'_3 = \frac{\sinh\left(\frac{\pi b}{4h_2}\right)}{\sinh\left[\frac{\pi}{2h_2}\left(\frac{b}{2} + d\right)\right]} \sqrt{\frac{\sinh^2\left[\frac{\pi}{2h_2}\left(\frac{b}{2} + d + a\right)\right] - \sinh^2\left[\frac{\pi}{2h_2}\left(\frac{b}{2} + d\right)\right]}{\sinh^2\left[\frac{\pi}{2h_2}\left(\frac{b}{2} + d + a\right)\right] - \sinh^2\left[\frac{\pi b}{4h_2}\right]}} \quad (3.27)$$

where h_2 is the thickness of the insulation layer. Therefore, the capacitance of a dielectric insulation layer C_3 is

$$C_3 = 2\varepsilon_0(\varepsilon_{ins} - 1) \frac{K(k'_3)}{K(k_3)} \quad (3.28)$$

Note that the capacitance effect of the insulation layer is simply added to the capacitance of IDC electrodes with substrate. Therefore, the total capacitance of IDC sensor with an insulation layer is given as

$$C_{total} = n \cdot l \cdot (C_1 + C_2 + C_3) \quad (3.29)$$

where n is the number of IDC finger period and l is the overlapping IDC finger length. A simple representation of partial capacitance technique is shown in Figure 3.7.

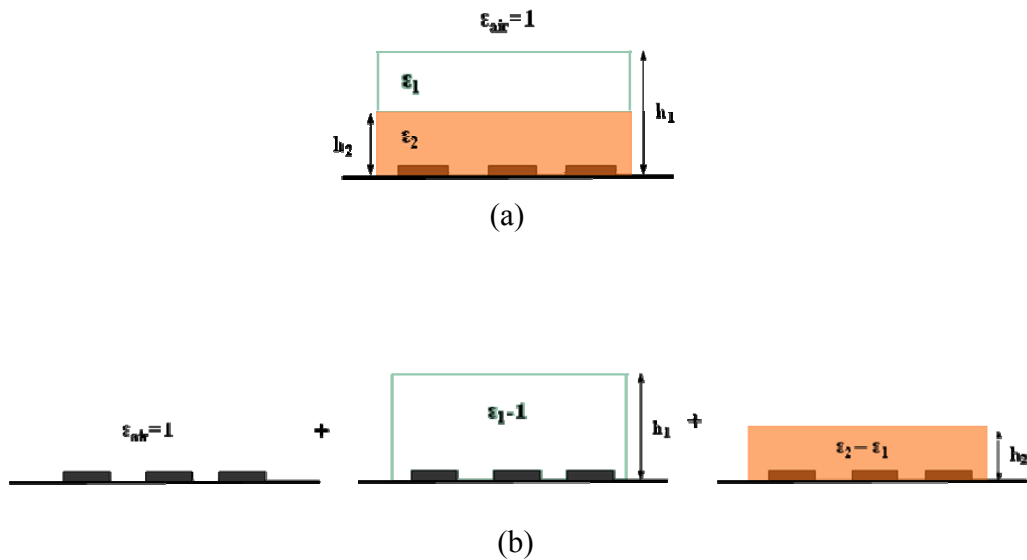


Figure 3.7: Illustration of the calculation of the capacitances of a multilayered structure (a) using partial capacitance technique [45].

3.3.3 Dependence of the capacitance on IDC geometric configurations

In this section the dependence of the capacitance of IDC on geometric parameters such as IDC finger thickness, width, spacing, and most importantly sensor wavelength λ is investigated. Understanding such features is essential to the evaluation and development of future IDC design.

3.3.3.1 Dependence on IDC finger thickness

The thickness of the previously measured IDC electrodes is about 1500 Å or 150 nm. The capacitances of several different IDC finger thicknesses are calculated in order to investigate the dependence on the finger thickness. As shown in Figure 3.8, the

influence of the finger thickness on the overall IDC capacitance is not notable and small capacitance increase is due to the fringing field capacitance increase.

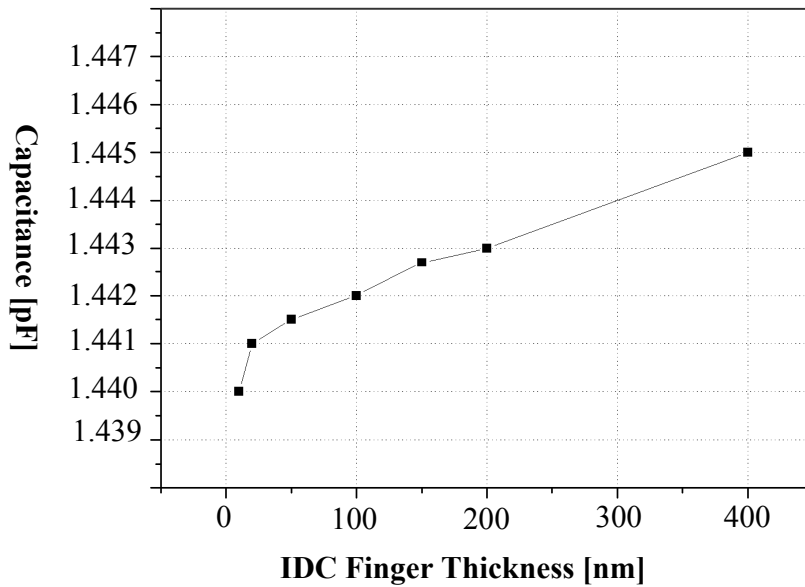


Figure 3.8: Capacitance change over different IDC finger thickness.

3.3.3.2 Dependence on IDC finger width and spacing

The following experimental results show the strong dependence of IDC finger width and spacing on overall IDC capacitance. IDC electrodes with different widths and spacing are calculated and evaluated. Note that the minimum spacing between IDC fingers is set to $40 \mu\text{m}$ due to the limitation of a simple mask making and overlap finger length is set to $1200 \mu\text{m}$. Figure 3.9 shows the effect of different IDC finger widths on the total IDC capacitance. The result indicates a strong influence of IDC finger widths on the

total capacitance: finger width change from 40 μm to 200 μm resulted in about 50 % increase of the total capacitance.

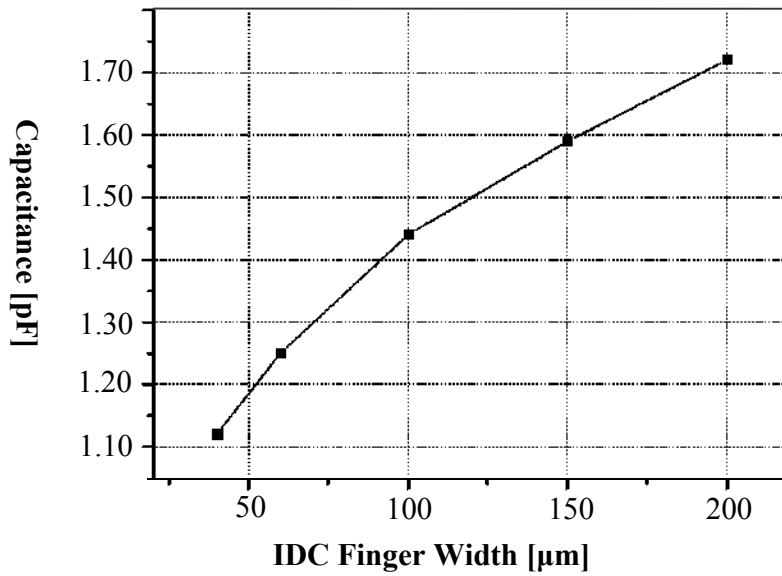


Figure 3.9: Capacitance change over different IDC finger widths.

In addition, the capacitance change over different IDC finger spacing is shown in Figure 3.10. For this calculation the finger width is set to 100 μm and other parameters are set to the same as previous experiment.

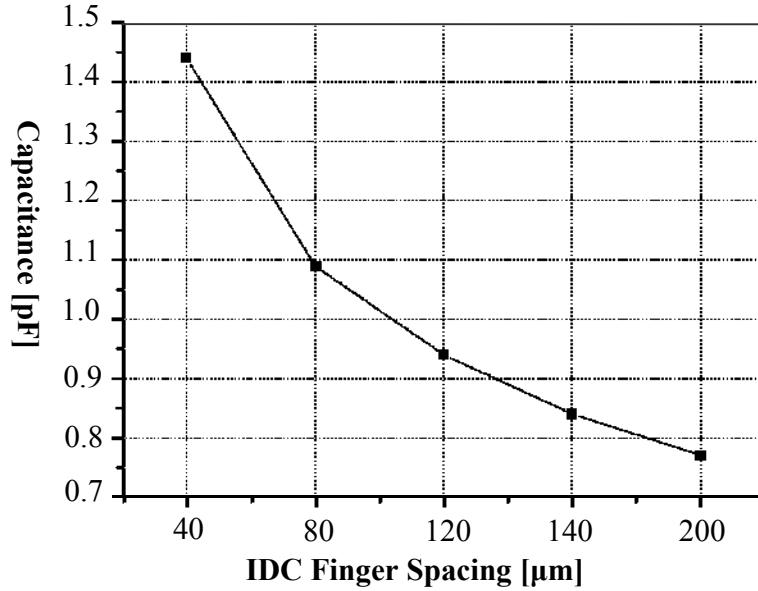


Figure 3.10: Capacitance change over different IDC finger spacing.

3.3.3.3 Dependence on IDC sensor wavelength λ and thickness of insulation layer h_2

The relationship among the total IDC capacitance, sensor wavelength λ , and insulation layer thickness h_2 is a very important factor to design the final sensing device. Therefore, this relationship will be used as a baseline for further calculation.

As shown in Figure 3.11, the total IDC capacitance reaches a saturation value for a value of $h_2/\lambda=0.5$. This means that the IDC device is not sensitive to a distance from the IDC finger electrode plane greater than about half the sensor wavelength λ . Therefore, when designing an IDC sensor with finger width of $100 \mu\text{m}$ and spacing of $40 \mu\text{m}$, an insulation layer must be much less than $140 \mu\text{m}$ in order to detect MUT (Material Under Test) over the insulation layer.

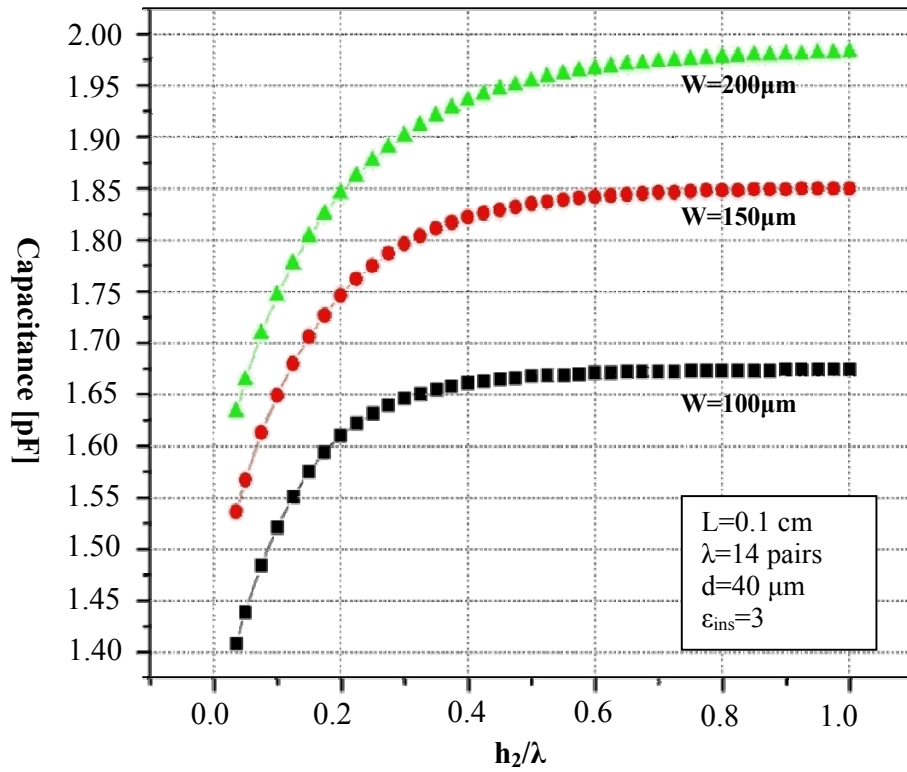


Figure 3.11: Capacitance as a function of the parameter h_2/λ .

3.4 DESIGN OF IDC SENSOR

A simple dielectric property measuring IDC sensor is fabricated using conventional photolithography processes on a quartz substrate. The geometric parameters of IDC sensor are based on the previous analysis. The IDC finger width and spacing are set to $100\ \mu\text{m}$ and $40\ \mu\text{m}$ respectively based on the previous geometrical dependence analysis. Several different numbers of IDC electrodes are fabricated.

The IDC electrodes are fabricated by thermal evaporation of aluminum and its thickness is set to 1500 Å. After the electrodes are patterned and defined, a thin dielectric insulation layer of SU-8 about 15 μm is deposited and patterned to electrically isolated electrodes from aqueous MUT. SU-8 is an excellent material for the insulation layer as it is mechanically strong and highly resistant to chemical solutions. Figure 3.12 shows microscopic pictures of the fabricated IDC electrodes with geometric dimensions. And Figure 3.13 shows the 3D drawing and cross-section view of the IDC sensor.

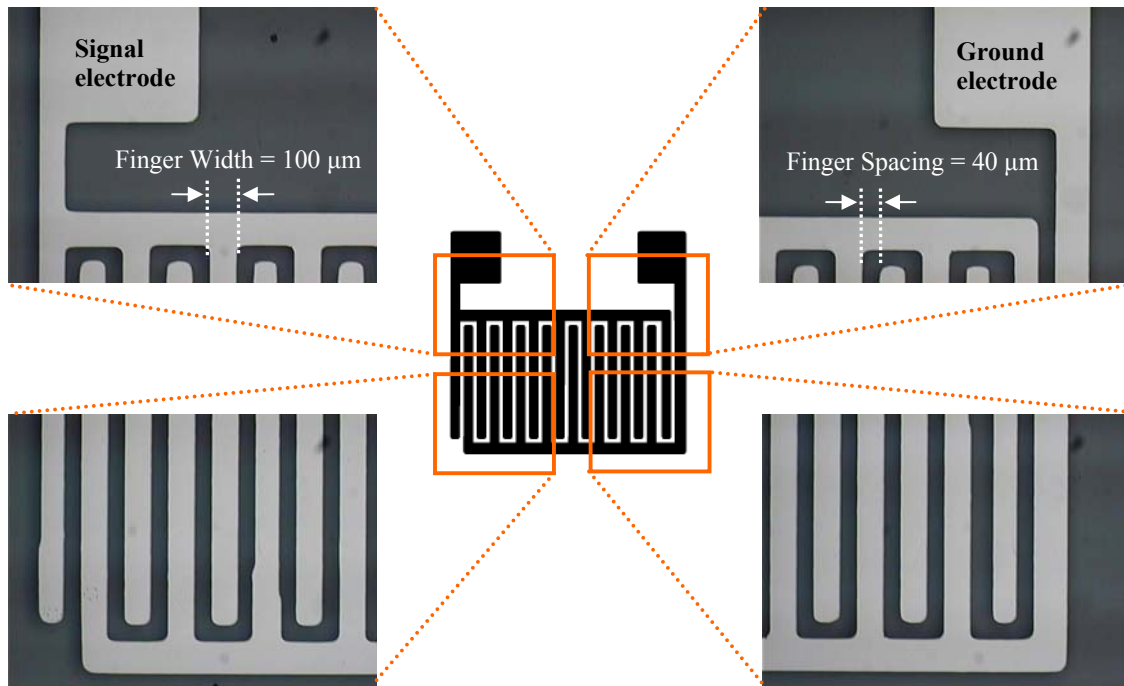


Figure 3.12: Microscopic pictures of fabricated IDC electrodes.

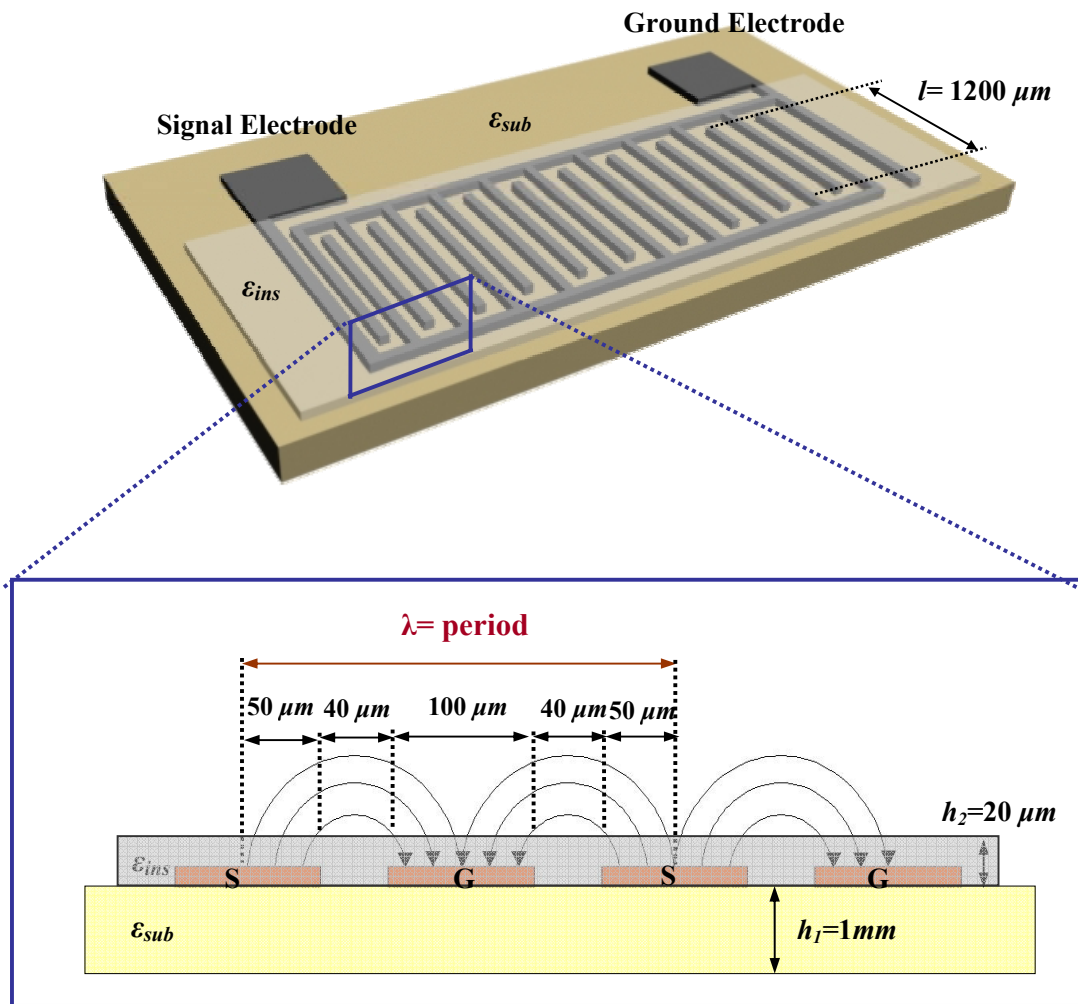


Figure 3.13: Illustration of our IDC electrode sensor configuration on a quartz substrate with geometric dimensions.

First, the line capacitance C_1 for the case of absence of a dielectric substrate layer is calculated. Using the actual geometric dimensions as shown in Figure 3.8, the modulus k_1 of the elliptical integral is given as

$$k_1 = \left(1 + \frac{2a}{2d + b}\right) \sqrt{\frac{\left(1 + \frac{b}{d}\right)}{\left(1 + \frac{a}{d} + \frac{b}{d}\right)\left(1 + \frac{a}{d}\right)}} \approx 0.89019$$

and the ratio of complete elliptical integral of the first kind based on the Hilberg's approximation is

$$\frac{K(k_1)}{K(k_1')} \cong \frac{2}{\pi} \ln\left(2\sqrt{\frac{1+k}{1-k}}\right) = \frac{2}{\pi} \ln\left(2\sqrt{\frac{1+0.8243}{1-0.8243}}\right) \cong 1.186$$

Therefore, the line capacitance C_1 is calculated as follows:

$$C_1 = 4 \varepsilon_0 \frac{K'(k_1)}{K(k_1)} \approx 0.263 \text{ [pF/cm]}$$

where $\varepsilon_0 = 8.85 \times 10^{-14} \text{ F/cm}$ is free space permittivity.

Now, consider the line capacitance C_2 with a dielectric substrate layer present. A quartz substrate with dielectric constant of 4.2 and thickness of 1 mm is used for our IDC sensor. Similarly, k_2 and the general function are given as follows:

$$k_2' = \frac{\sinh\left(\frac{\pi b}{4h_1}\right)}{\sinh\left[\frac{\pi}{2h_1}\left(\frac{b}{2} + d\right)\right]} \sqrt{\frac{\sinh^2\left[\frac{\pi}{2h_1}\left(\frac{b}{2} + d + a\right)\right] - \sinh^2\left[\frac{\pi}{2h_1}\left(\frac{b}{2} + d\right)\right]}{\sinh^2\left[\frac{\pi}{2h_1}\left(\frac{b}{2} + d + a\right)\right] - \sinh^2\left(\frac{\pi b}{4h_1}\right)}} \approx 0.456$$

and

$$\frac{K(k_2')}{K'(k_2')} \cong \frac{\pi/2}{\ln\left(2\sqrt{\frac{1+k_2}{1-k_2}}\right)} = \frac{\pi/2}{\ln\left(2\sqrt{\frac{1+0.889}{1-0.889}}\right)} \approx 0.745$$

Therefore, the line capacitance C_2 is

$$C_2 = 2\varepsilon_0(\varepsilon_{sub} - 1) \frac{K(k_2')}{K(k_2)} \approx 0.421 \quad [pF/cm]$$

Finally, the line capacitance of an insulation layer is computed. SU-8 material is used as an insulation material for our IDC sensor due to its good mechanical properties. The dielectric constant of SU-8 is 3 and the height of the insulation layer is about $15 \mu m$. Based on these parameters, the complete elliptical integral is calculated as

$$k_3' = \frac{\sinh\left(\frac{\pi b}{4h_2}\right)}{\sinh\left[\frac{\pi}{2h_2}\left(\frac{b}{2} + d\right)\right]} \sqrt{\frac{\sinh^2\left[\frac{\pi}{2h_2}\left(\frac{b}{2} + d + a\right)\right] - \sinh^2\left[\frac{\pi}{2h_2}\left(\frac{b}{2} + d\right)\right]}{\sinh^2\left[\frac{\pi}{2h_2}\left(\frac{b}{2} + d + a\right)\right] - \sinh^2\left(\frac{\pi b}{4h_2}\right)}} \approx 0.08$$

and the capacitance C_3 is

$$C_3 = 2\varepsilon_0(\varepsilon_{ins} - 1) \frac{K(k_3')}{K'(k_3')} \approx 0.143 \quad [pF/cm]$$

Therefore, the total capacitance of IDC sensor with a SU-8 insulation layer is calculated as

$$C_{total} = n \cdot l \cdot (C_1 + C_2 + C_3) = 1.44 \quad [pF/cm]$$

where $n=14.5$ is the number of sensor wavelength and $l=0.12 \text{ cm}$ is the overlapping electrode length.

Then, the calculation of the total capacitance of the IDC sensor is verified with the actual measurement data. Figure 3.14 shows the comparison over a range of frequencies. The graph indicates that both calculation and measured data fit quite well within 3.5% of an error margin. Therefore, we can safely conclude that the analytical model developed here is in good agreement with the experimental result.

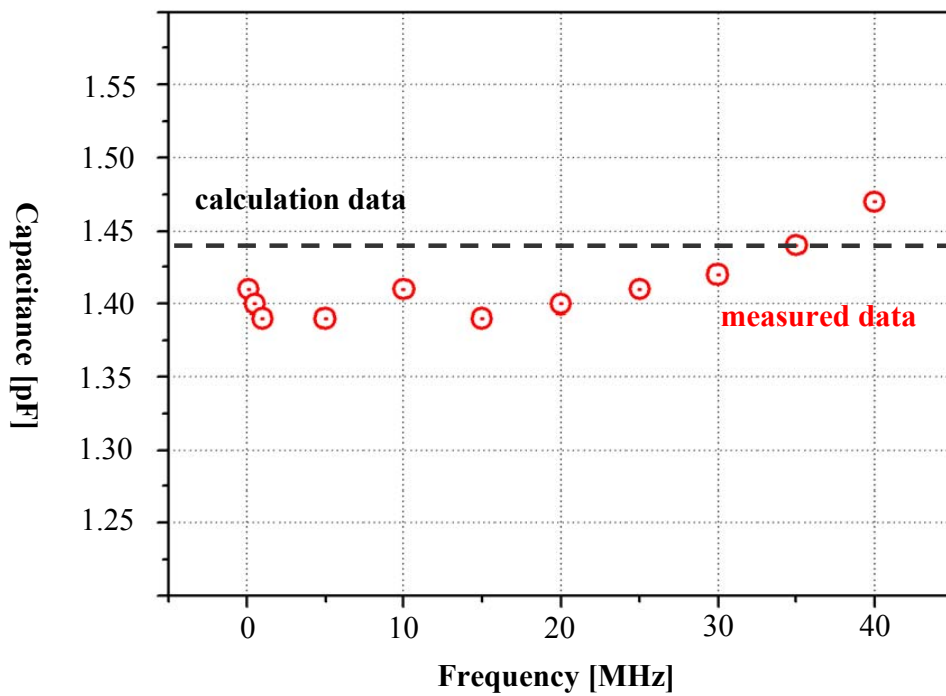


Figure 3.14: Capacitance of an IDC sensor with a SU-8 insulation layer as a function of frequency: comparison between actual measurement and calculation data.

Chapter 4: Measurement Techniques

The impedance of IDC sensor is measured with Hewlett-Packard 4194A Impedance/Gain-Phase Analyzer and LabVIEW as control software. The HP 4194A provides two different impedance measurement techniques with different frequency sweep ranges: measurement with z-probe (10Hz~100MHz) and measurement with impedance analyzer (100Hz~40MHz) [48]. In this chapter both measurement procedures and results are discussed.

4.1 Measurement setup

The actual measurement of the input impedance is complicated by many factors, mainly due to the connection of the impedance meter to the IDC sensor. An impedance measurement includes the impedance of everything on the measurement side of the sensing circuit. This includes connectors, circuitry in the impedance meter itself, cables, and many other items necessary to interface the device being measured with the part of the impedance meter performing the measurement. It is therefore necessary to remove the contributions of all items, excluding the device being measured. Depending on how it is performed, this procedure is called calibration or compensation [49].

The reference plane is the point in the measuring circuit where both ground and signal are defined. All measurements are made from that plane because it is the only place where there is truly a ground and a source signal of known magnitude: zero magnitude and zero phase.

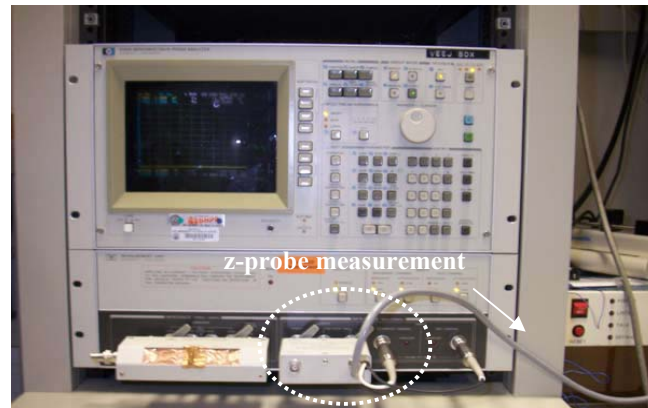
Calibration is defined as mathematically moving the reference plane of the measurement to some other location. As mentioned above, the default reference plane is located at the sensing circuit. Known impedances, called standard, are used to make a

series of measurement from which the calibration coefficients are computed. The coefficients are used with all subsequent measurements to mathematically move the reference plane to a new location in the measuring apparatus and to attach units to all measurements. Compensation is similar to calibration because it also removes measurement errors using known standards. Compensation differs from calibration because, in compensation, the reference plane is not moved and units are not assigned. Parasitics in the measurement apparatus are compensated for or removed [49].

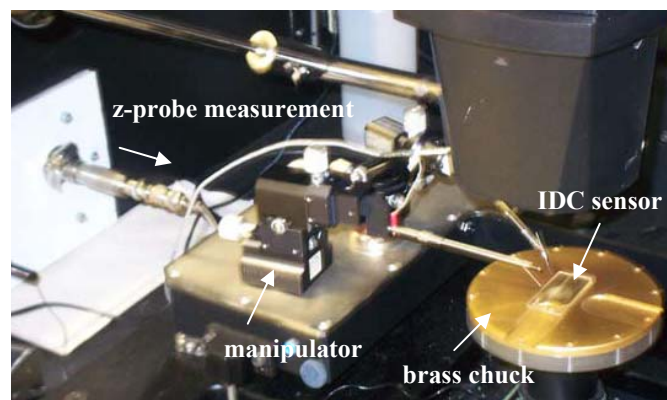
4.2 Impedance measurement with z-probe

In order to measure the impedance with z-probe open/short/load (OSL) calibration needs to be carried out first. As mentioned previously, the OSL calibration moves the reference plane of the measurement to the tip of the z-probe. Then, z-probe is connected to a dual signal/ground cable through probe manipulators where tungsten probe tips are placed on the signal and ground electrode pads of IDC sensor on the vacuum chuck. The chuck is considered floating because it has no DC connection. Again, beyond z-probe open/short compensation is performed to remove the unwanted parasitic which are present in the dual cable. Figure 4.1 shows the photography of z-probe measurement setup with IDC sensor.

HP 4194 A Impedance/Gain-Phase Analyzer



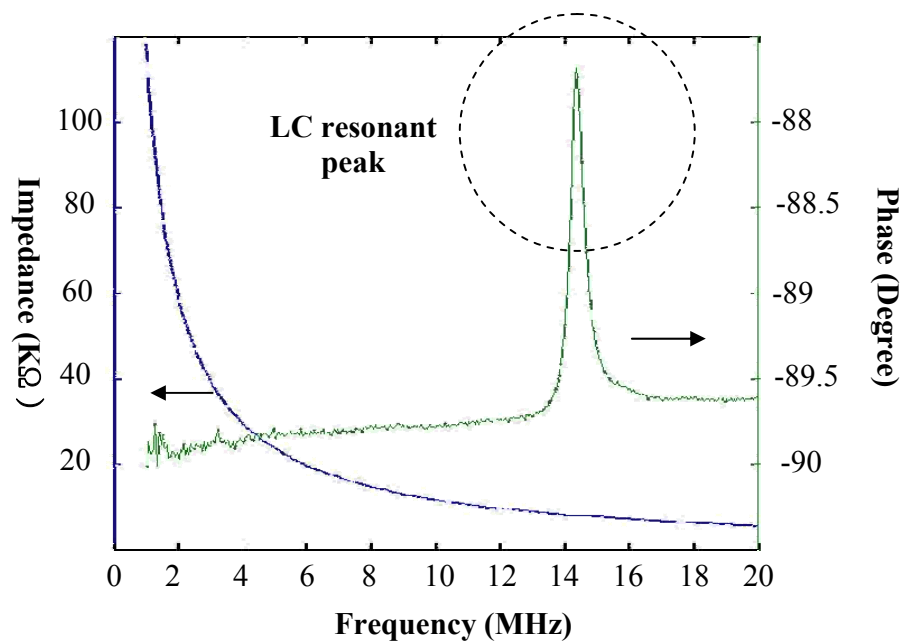
(a)



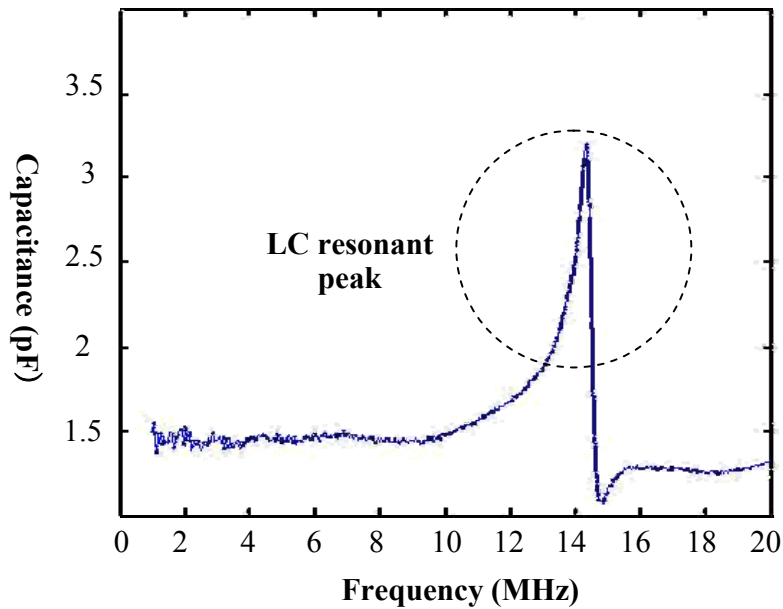
(b)

Figure 4.1: Photographs of z-probe technique setup for the impedance measurement: (a) HP 4194A impedance analyzer and (b) probe station for impedance measurement.

Figure 4.2 (a) shows plots of measured impedance and phase of the IDC sensor over frequency sweep range and (b) is the plot showing extracted capacitance value from the measured impedance data. Unfortunately, the plots show a very prominent peak in what should be a smooth set of data. It resembles LC resonance at a specific frequency. Efforts are made to remove the unwanted resonant peak from the measurement, but it was hard to remove it since the resonant peak is inherent to the test system such as long cables, tungsten probe tips, manipulator, and connectors. A few measurements of many intents show a little bit improved plots, but the repeatability of experimental measurement is another concern.



(a)



(b)

Figure 4.2: Measured data of the IDC sensor using z-probe technique: (a) impedance and phase over frequency range and (b) extracted capacitance value of the IDC sensor

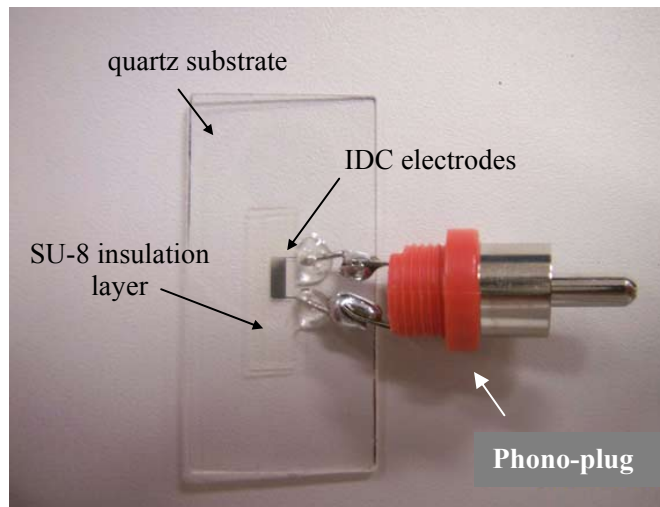
4.3 Impedance measurement with impedance analyzer

Impedance measurement with impedance analyzer provides only open/short compensation option. In addition, the frequency sweep extends only up to 40MHz. This is not a limiting factor as this is enough frequency range for our impedance analysis. However, the actual problem of this measurement technique is also the long cable length from the impedance analyzer to the probe station. Even though the majority of parasitic capacitor and inductor can be compensated for or removed with open/short compensation, this is not a good way of measuring relatively small value of capacitance.

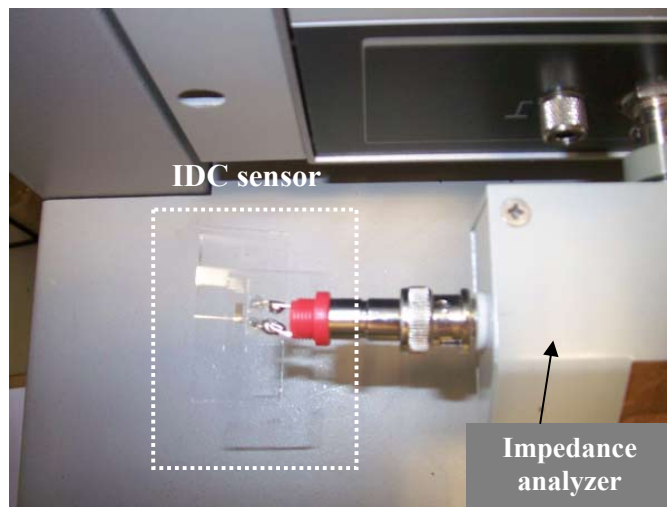
Therefore, in order to proceed to next experiments, removing the parasitic long cable from the measurement is necessary. A new connection method with impedance analyzer is introduced which is not possible with z-probe technique: direct measurement with impedance analyzer.

The IDC sensor and a phono-plug are bonded together through soldering technique as shown in Figure 4.3 (a). One notable advantage of this connection-via-phono-plug method is that all the unnecessary long cables, probe manipulator, and tungsten probe tips are removed from the measurement. That removed the parasitic LC resonance which was present in the conventional z-probe and impedance analyzer techniques as well. In addition, the time required to process multiple impedance measurements is considerably reduced. Figure 4.3 (b) shows a photograph of the direct measurement setup with impedance analyzer.

Again, open/short compensation using shorted and opened phono-plugs is performed before starting any measurement in order to remove parasitic capacitance and inductance present inside the phono-plug. After the proper compensation, a test measurement is performed with the same IDC sensor used for the previous experiment. Figure 4.4 (a) shows plots of the measured impedance and phase data over frequency range. It clearly shows that the LC resonance is completely removed. Figure 4.4 (b) is a plot of the extracted capacitance value of the IDC sensor and it shows a good agreement with the calculation data as expected.

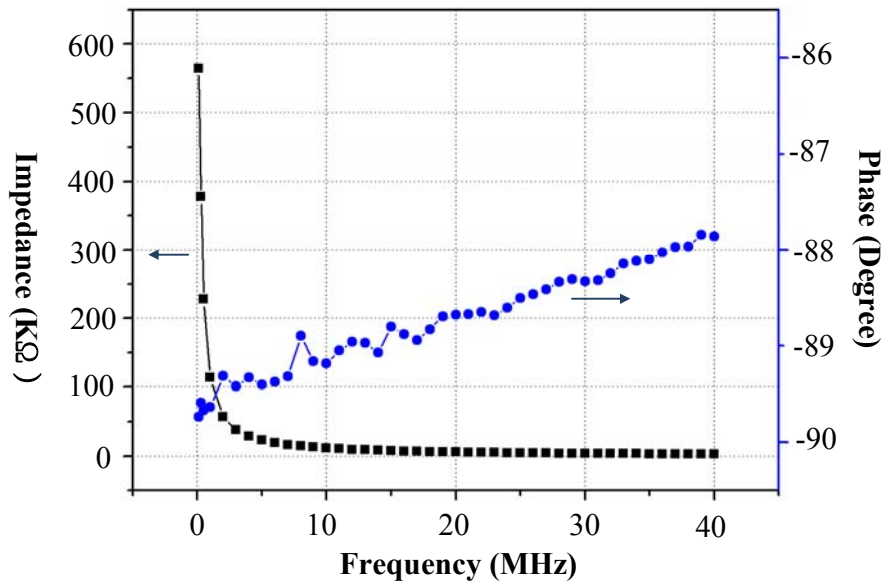


(a)

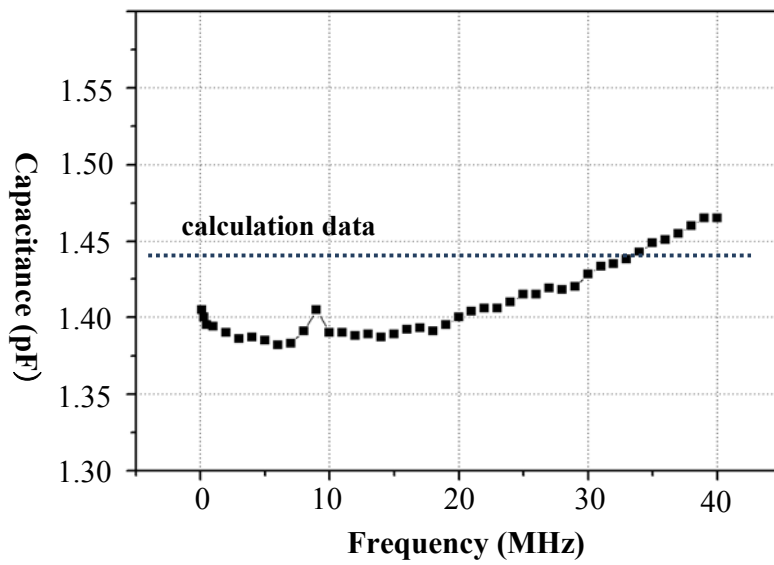


(b)

Figure 4.3: Photographs of (a) IDC sensor bonded to a phono-plug and (b) direct measurement setup with impedance analyzer.



(a)



(b)

Figure 4.4: Measured data of the IDC sensor using direct measurement technique: (a) impedance and phase over frequency range and (b) extracted capacitance value of the IDC sensor.

Chapter 5: Detection Mechanism of Direct Measurement

In this chapter several different equivalent circuit models of IDC sensor are presented. In addition, a new analytical evaluation method is proposed and evaluated for the actual measurement data analysis. This method is verified with extraction of dielectric properties of known materials and dielectric properties of truly unknown materials are tested as well.

5.1 Problem with traditional conformal mapping circuit model

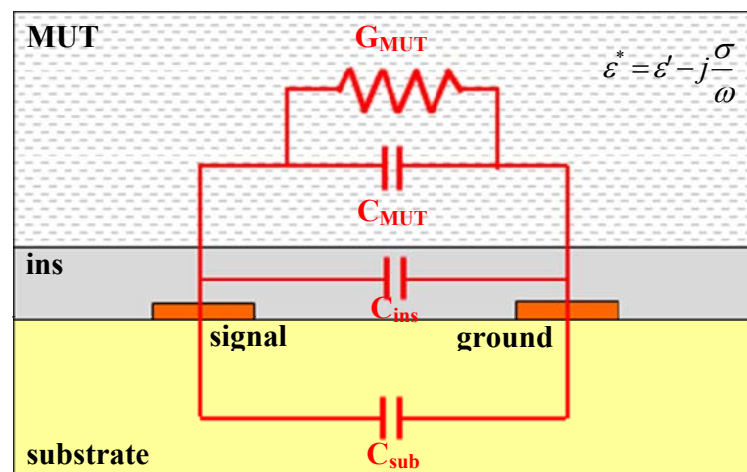


Figure 5.1: Cross-section view of IDC sensor with its superimposed equivalent circuit model.

Figure 5.1 shows IDC sensor with its superimposed equivalent circuit model based on the traditional conformal mapping technique. Note that all the capacitances are connected in parallel including the loss of the material under test (MUT). Based on the partial capacitance technique, the capacitance of each layer is given by

$$C_{mut} = 2\varepsilon_0\varepsilon_{mut} \frac{K'_1(k_1)}{K_1(k_1)} \quad (5.1)$$

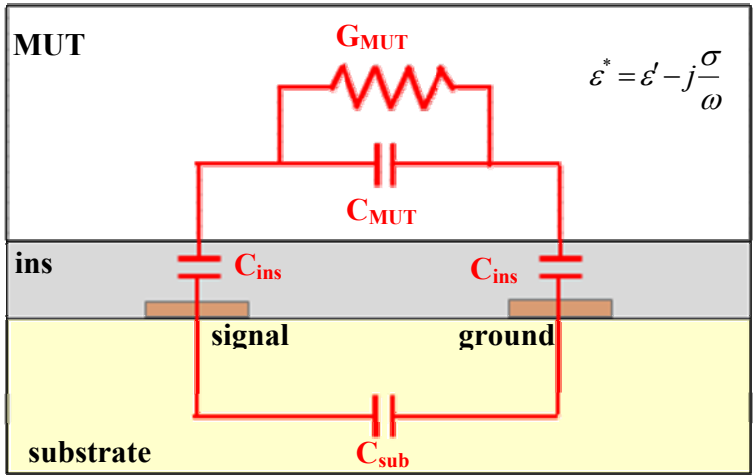
$$C_{ins} = 2\varepsilon_0(\varepsilon_{ins} - \varepsilon_{mut}) \frac{K'_2(k_2)}{K_2(k_2)} \quad (5.2)$$

$$C_{sub} = 2\varepsilon_0\varepsilon_{sub} \frac{K'_3(k_3)}{K_3(k_3)} \quad (5.3)$$

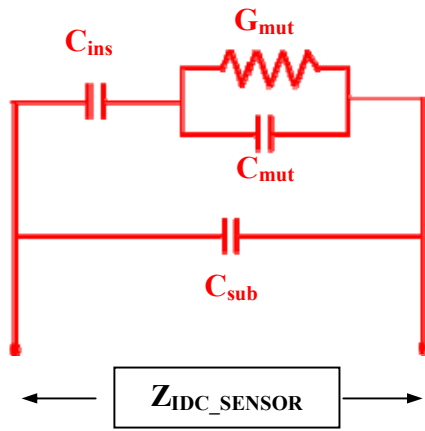
The problem occurs when MUT has relative dielectric constant bigger than that of the insulation layer. In other words, the equation (5.2) becomes negative. The total capacitance is reduced due to this negative capacitance and makes sense from the mathematical point of view. However, interpreting negative capacitance in physical world is not very convincing. Moreover, when analyzing the fringing electric field path from one electrode to another electrode, it makes more sense that both the capacitance of the insulation layer and the capacitance of MUT must be connected in series. Therefore, this circuit model needs to be modified accordingly for our IDC sensor.

5.2 New equivalent circuit model

In this section a new equivalent circuit model is presented and evaluated. Figure 5.2 (a) shows a schematic diagram of cross section view of IDC sensor with a superimposed new equivalent circuit model and Figure 5.2 (b) is the expanded representation of the circuit. The insulation capacitance is now connected in series with the capacitance of MUT.



(a)



(b)

Figure 5.2: (a) Cross-section view of IDC sensor with its superimposed new equivalent circuit model and (b) expanded representation of the circuit.

Then the total impedance of IDC sensor can be expressed as

$$Z_{IDC_SENSOR} = \left\{ j\omega C_{sub} + \left(\frac{1}{j\omega C_{ins}} + \frac{1}{G_{MUT} + j\omega C_{MUT}} \right)^{-1} \right\}^{-1} \quad (5.4.a)$$

or

$$Y_{IDC_SENSOR} = \frac{1}{Z_{IDC_SENSOR}} = j\omega C_{sub} + \left(\frac{1}{j\omega C_{ins}} + \frac{1}{G_{MUT} + j\omega C_{MUT}} \right)^{-1} \quad (5.4.b)$$

As the admittance of the substrate is independent of the presence of MUT, its contribution can be subtracted directly from the measured total admittance. Therefore, it will be neglected in the subsequent analyses. Note that the insulation layer is no longer evaluated using conformal mapping technique and it is estimated using parallel plate model. In other words, if there is an imaginary plate placed parallel to the electrode and most electric flux passes through the insulation layer, the capacitance of the insulation layer can be estimated using a simple parallel plate equation $\epsilon_0 \epsilon_{ins} w/h$, where w is the width of the electrode, h is the thickness of the insulation layer, and ϵ_{ins} is given as 3 from the reference data sheet[27]. Therefore, the insulation layer is now independent and impedance of MUT can be easily extracted from the measurement data by simply subtracting the calculated parallel capacitance of the insulation layer.

However, after evaluating this new circuit model several times with the measurement data, we have found that the insulation layer can not be considered independently from MUT. Moreover, there are more important parameters that need to be analyzed in order to extract accurate information of MUT. These parameters are explained more in detail in the following.

First, the new circuit model is evaluated using the parallel plate analysis with the air measurement data. Air is used as a good reference material as it has known parameter such as $\epsilon_{\text{air}}=1$ and $\sigma_{\text{air}}=0$. Although the insulation material, SU-8, is considered as a very good dielectric material, it is shown from the analysis that SU-8 behaves slightly as a “lossy” material as frequency increases.

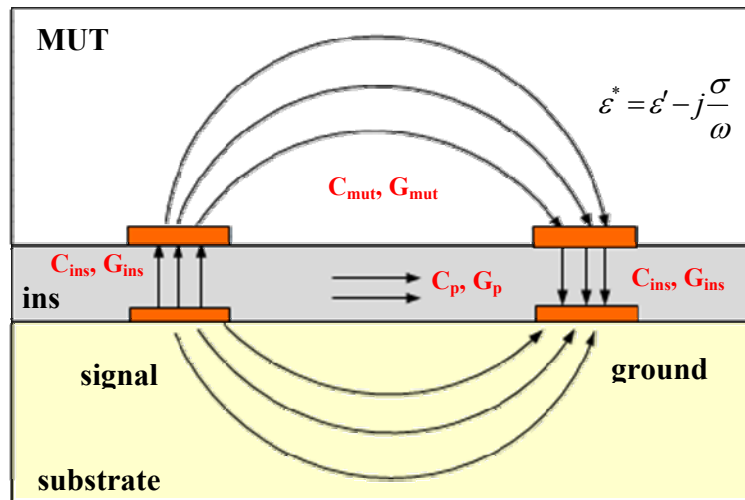
Second, when a very good dielectric material such as air is present above the insulation layer, a portion of the electric flux must flow directly from signal electrode to ground electrode within the insulation layer without passing through MUT. This accounts for other loss in the insulation layer.

Third, although the insulation layer is estimated using a simple parallel plate model based on its own parameters, it is shown that it can not be considered separately from MUT. Therefore, there must be a correlation between the insulation layer and MUT.

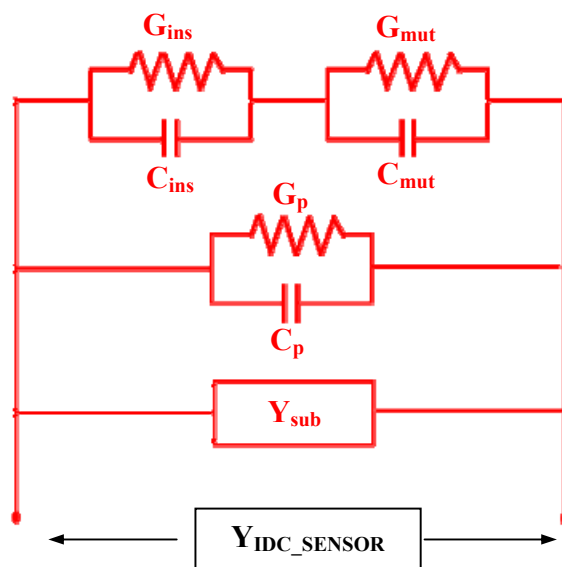
Therefore, as a summary, these three parameters are very important in order to extract very accurate information regarding MUT. So, the previous circuit model is modified again accordingly to include all these parameters, which is presented in the next section.

5.3 Modified equivalent circuit model

Figure 5.3(a) illustrates the possible electric flux path in the IDC sensor and Figure 5.3(b) represents the modified equivalent circuit model. Note that loss term of the insulation layer G_{ins} is now considered in parallel with the C_{ins} , and C_p and G_p represent the direct flux from the signal electrode to the ground electrode within the insulation layer.



(a)



(b)

Figure 5.3: (a) Schematic diagram of electric flux path in the IDC sensor and (b) its modified equivalent circuit model.

Then, the total impedance is expressed as

$$Y_{IDC_SENSOR} = Y_{sub} + (G_p + j\omega C_p) + \left(\frac{1}{G_{ins} + j\omega C_{ins}} + \frac{1}{G_{MUT} + j\omega C_{MUT}} \right)^{-1} \quad (5.5)$$

Equation (5.5) shows that G_p , C_p , and G_{ins} must be determined in order to extract dielectric properties of MUT from the measurement data Y_{IDC_SENSOR} . It is not possible to determine those parameters from one single measurement because the measurement data contains only impedance and phase information of the whole system. Therefore, before proceeding further analysis, those parameters must be estimated first.

5.3.1 C_p estimation using parallel plate analysis

It is not an easy task to define an exact value of C_p because C_p is also dependent of MUT. However, one smart way to estimate C_p is to find the boundary limit for extreme cases. If the maximum C_p can be calculated, it can be used as the upper bound limit for most analyses. So, in order to find the upper bound limit of C_p air is used as MUT since the maximum flux must flow directly when a low dielectric constant layer is present above the insulation layer.

The process of finding the maximum C_p is as follows. First, the conventional partial capacitance technique is used to obtain the total capacitance value based on the conformal mapping. The equivalent circuit model is shown in Figure 5.4 (a). The total capacitance is calculated as 0.12 [pF/cm] by summation of each partial capacitance,

$$C_{air} = \varepsilon_0(1) \frac{K_1(k'_1)}{K_1(k_1)} = 0.07[\text{pF} / \text{cm}]$$

and

$$C_{ins} = \varepsilon_0(\varepsilon_{ins} - 1) \frac{K_2(k'_2)}{K_2(k_2)} = 0.05[\text{pF} / \text{cm}]$$

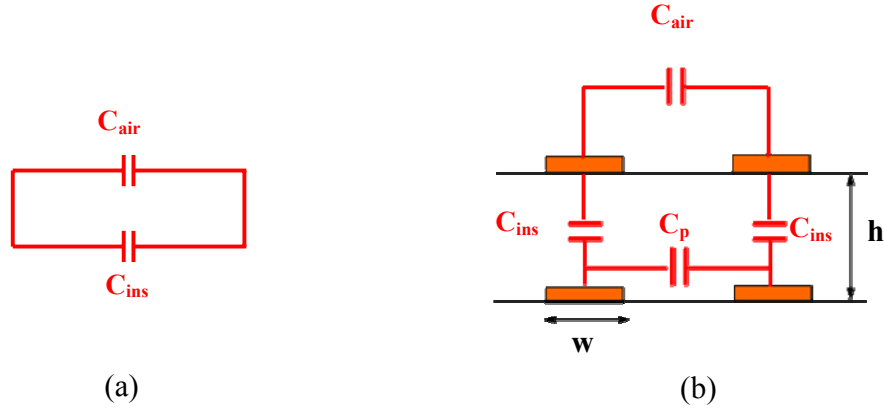


Figure 5.4: Schematic diagram of (a) partial capacitance circuit model and (b) parallel plate circuit model of IDC sensor.

Then, if the total partial capacitance is set equal to the total capacitance of the parallel plate model, C_p can be calculated. Figure 5.4(b) shows the equivalent circuit model for the parallel plate analysis. C_{air} is calculated using same conformal mapping and C_{ins} is calculated using parallel plate equation

$$C_{ins} = \epsilon_0 \epsilon_{ins} \frac{w}{h} = 1.77 [pF / cm]$$

where $\epsilon_0 = 8.85 \times 10^{-14} [F/cm]$, $\epsilon_{ins} = 3$, $w = 100 \mu m$, and $h = 15 \mu m$. The total capacitance of the parallel plate model is then estimated as

$$C_{total_equiv} = C_p + \left(\frac{1}{C_{ins}} + \frac{1}{C_{air}} + \frac{1}{C_{ins}} \right)^{-1} = C_p + \left(\frac{1}{1.77} + \frac{1}{0.07} + \frac{1}{1.77} \right)^{-1} = C_p + 0.07 [pF / cm]$$

Therefore, $C_p = C_{total_equiv} - 0.07$ is $0.05 [pF/cm]$. This value will be fixed as the maximum value of C_p throughout the subsequent analyses, since it can not be bigger when material other than air is present. Once C_p is determined, now let's estimate the other important parameter C_{ins} .

5.3.2 C_{ins} estimation using parallel plate analysis

The circuit model shown in Figure 5.5 with fixed $C_p=0.05$ [pF/cm] is used for the estimation of C_{ins} . Again, same parallel plate analysis is used for the C_{ins} estimation. Let's first assume that MUT is water and its dielectric constant is 80. Then, C_{water} and C_{ins} are calculated first using partial capacitance technique as follows:

and
$$C_{water} = \epsilon_0 (80) \frac{K_1(k_1')}{K_1(k_1)} = 5.58 [pF / cm]$$

$$C_{ins} = \epsilon_0 (\epsilon_{ins} - 80) \frac{K_2(k_2')}{K_2(k_2)} = -1.92 [pF / cm]$$

Note that C_{ins} is negative and the total capacitance $C_{total_partial}=C_{water}+C_{ins}$ is 3.66 [pF/cm]. Then, this total capacitance is set equal to the total capacitance of parallel plate model, which is given by

$$3.66 = 0.05 + \left(\frac{1}{C_{ins}} + \frac{1}{5.58} \right)^{-1}$$

and C_{ins} is calculated as 10.2 pF/cm

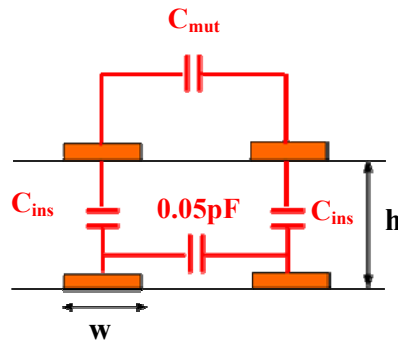


Figure 5.5: Equivalent parallel plate circuit model with fixed C_p .

Now, let's assume that MUT has dielectric constant of 18. Using the same partial capacitance method, C_{mut} and C_{ins} are calculated as follows

$$C_{mut} = \varepsilon_0 (18) \frac{K_1(k'_1)}{K_1(k_1)} = 1.18 [pF / cm]$$

and

$$C_{ins} = \varepsilon_0 (3-18) \frac{K_2(k'_2)}{K_2(k_2)} = -0.37 [pF / cm]$$

Then, the total capacitance $C_{total_partial} = C_{mut} + C_{ins}$ is 0.81 [pF/cm]. Again, this total capacitance is set equal to the total capacitance of parallel plate model, and C_{ins} is calculated as 2.14 [pF/cm]. Note that C_{ins} is different from the previous analysis and is changing with different value of dielectric constant of MUT. Let's try one more case where dielectric constant is 3 to find the correlation between C_{ins} and ε_{mut} .

If $\varepsilon_{mut}=3$, then the C_{mut} and C_{ins} are

$$C_{mut} = \varepsilon_0 (3) \frac{K_1(k'_1)}{K_1(k_1)} = 0.21 [pF / cm]$$

and

$$C_{ins} = \varepsilon_0 (3-3) \frac{K_2(k'_2)}{K_2(k_2)} = 0 [pF / cm]$$

The total partial capacitance is 0.21 [pF/cm] and C_{ins} is calculated from the same algebraic equation for the parallel plate model and it is 0.67 [pF/cm]. Figure 5.6 shows the plot of the calculated C_{ins} as a function of ε_{mut} . Note that the "fitting" parameter C_{ins} looks like it is very close to a straight line as a function of the dielectric constant of the medium above. However, instead of using a simple linear function, the quadratic fitting equation is derived analytically from the parallel plate circuit model to avoid moderate errors. The derived quadratic fitting equation is given as

$$C_{ins} = \frac{\left(\frac{\epsilon_0^2}{K_1^2} - \frac{\epsilon_0^2}{K_1 K_2} \right) \epsilon_{mut}^2 + \left(\frac{3\epsilon_0^2}{K_1 K_2} - \frac{0.05 * 10^{-12} \epsilon_0}{K_1} \right) \epsilon_{mut}}{\left(\frac{\epsilon_0}{K_2} \right) \epsilon_{mut} + \left(0.05 * 10^{-12} - \frac{3\epsilon_0}{K_2} \right)} \quad (5.6)$$

where K_1 and K_2 are the complete elliptical integral of the first kind.

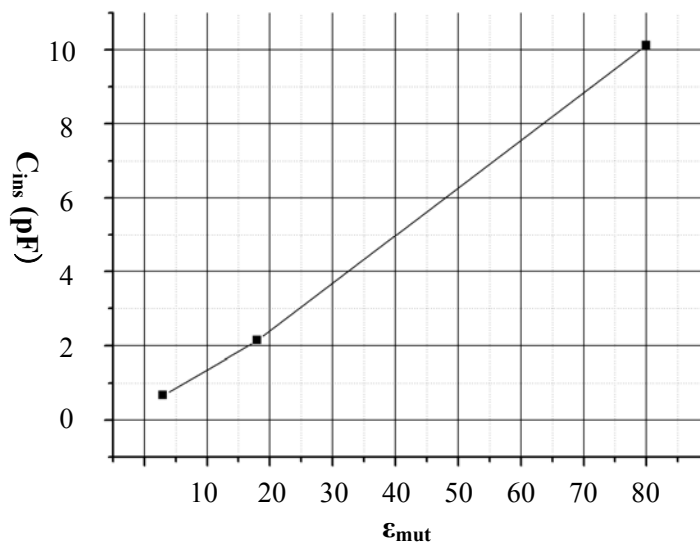


Figure 5.6: Plot of estimated C_{ins} as a function of the dielectric constant of MUT.

5.3.3 G_{ins} estimation from the measured air data

Now G_{ins} can be estimated based on the previous C_p estimation and the relationship between C_{ins} and ϵ_{mut} . In this analysis the actual air measurement data is used to extract the G_{ins} . First, C_{ins} is calculated using equation (5.6) with $\epsilon_{mut}=1$ and it is given as $C_{ins}=0.37$ [pF/cm]. The equivalent circuit model is shown in Figure 5.7.

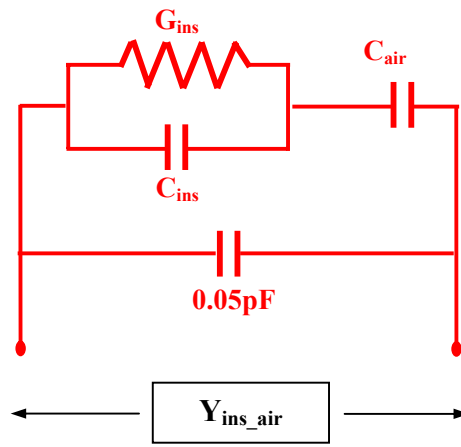
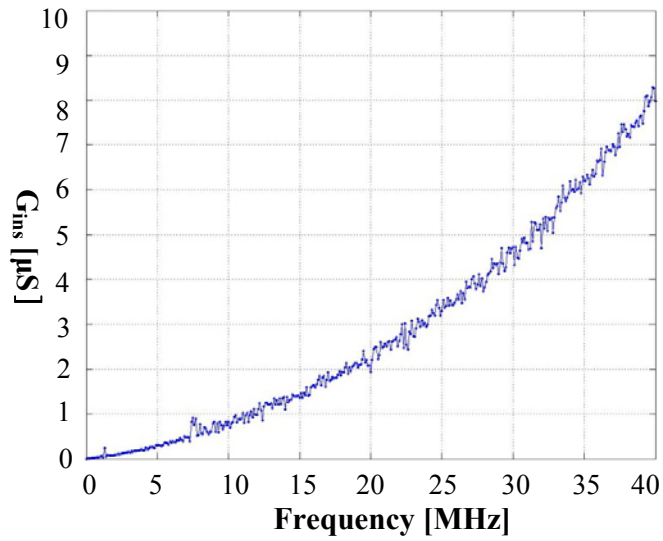


Figure 5.7: Equivalent circuit model for G_{ins} estimation.

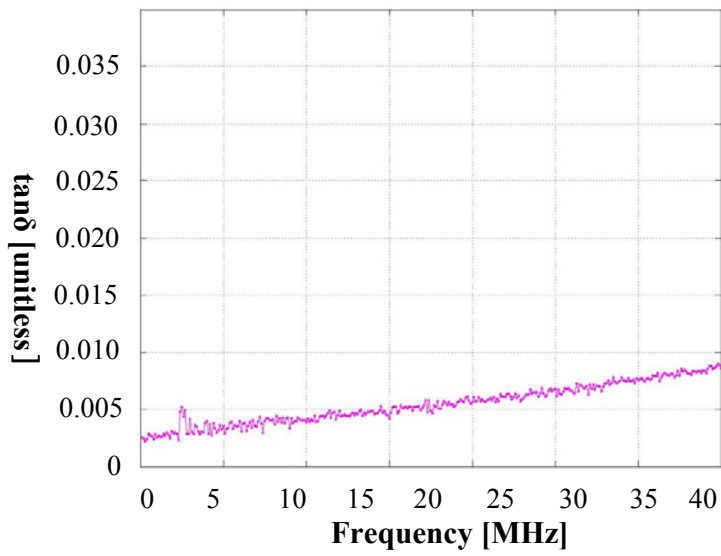
The total impedance of the circuit Y_{ins_air} is given by

$$Y_{ins_air} = j\omega C_p + \left(\frac{1}{G_{ins} + j\omega C_{ins}} + \frac{1}{j\omega C_{air}} \right)^{-1} \quad (5.7)$$

Note that the contribution of substrate is already subtracted from the measurement data and Y_{ins_air} represents only the upper part of IDC electrodes. After some manipulation of the equation (5.7), G_{ins} is extracted from Y_{ins_air} measurement data and $\tan\delta$ is also extracted. The results are shown in Figure 5.8.



(a)



(b)

Figure 5.8: Plot of (a) extracted G_{ins} and (b) $\tan\delta$ of the insulation layer over various frequencies.

5.4 Measurement of dielectric properties of materials using fitting model analysis

In this section an analytical fitting model analysis is presented. The fitting model analysis consists of iterative extraction process by simultaneously fitting both C_{mut} and C_{ins} in order to extract the dielectric properties of materials. It begins with an initial guess value of ϵ_{mut} and the iteration processes continue until the extracted values converge.

The basic principle of fitting iteration process is as follows. Once the initial guess value of ϵ_{mut} determines C_{ins} , the admittance of insulation layer is defined as $Y_{ins}=G_{ins}+j\omega C_{ins}$. The data measured directly from the impedance analyzer (i.e., the raw data at the connector plane as illustrated in Figure 4.3b) is first compensated for any parasitic connector admittance, substrate capacitance, and the C_p term through the subtraction of the measured admittance of an IDC-connector device that has no insulator or MUT covering the IDC electrodes. Then, this compensated measured data, $Y_{measured}$, contains impedance information about only the insulation layer and MUT. Therefore, Y_{mut} can be easily obtained as follows:

$$Y_{mut} = G_{mut} + j\omega C_{mut} = \left(\frac{1}{Y_{measured}} - \frac{1}{Y_{ins}} \right)^{-1} \quad (5.8)$$

Then, ϵ_{mut} is extracted from $[C_{mut}/\epsilon_o] \bullet [K_2(k_2)/K_2(k'_2)]$. Similarly, σ_{mut} is extracted using $\epsilon_{MUT}\epsilon_o G_{mut}/C_{mut}$. This extracted ϵ_{mut} is used for the second iteration to determine new C_{ins} . In the same fashion, the fitting iteration processes continue until the extracted values converge to the previous input values.

Extraction of dielectric properties of known materials is conducted first in order to validate this fitting model analysis. Then, dielectric properties of truly unknown materials are extracted using the same fitting model analysis.

5.4.1 Extract dielectric properties of known materials

5.4.1.1 Extraction of dielectric properties of air

Air is tested first for the self consistency check. The equivalent circuit model is shown in Figure 5.9. Again, C_p is assume to be 0.05 [pF/cm] and Y_{ins_air} is the measured air data.

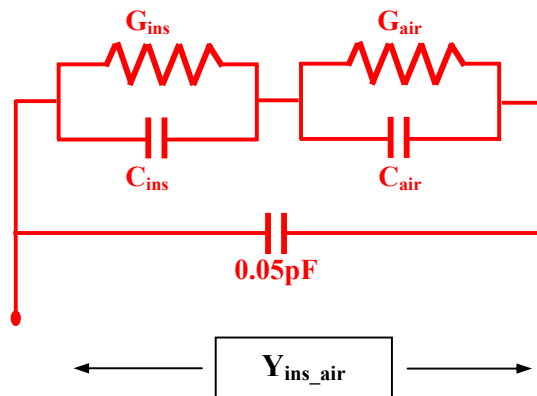
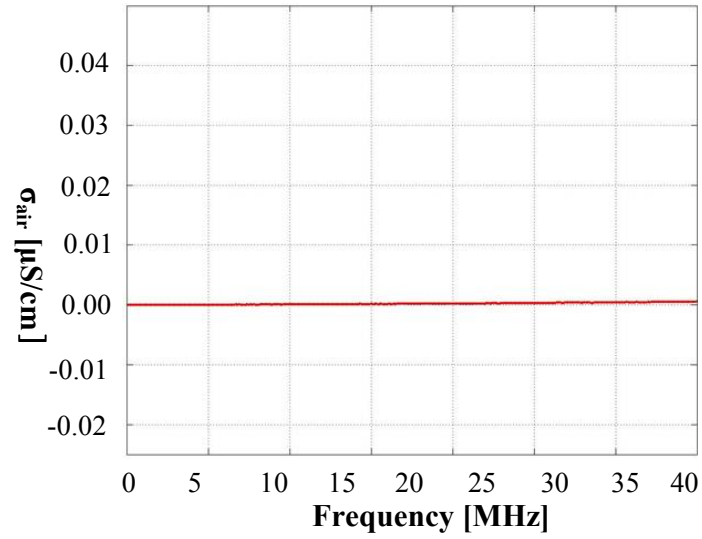
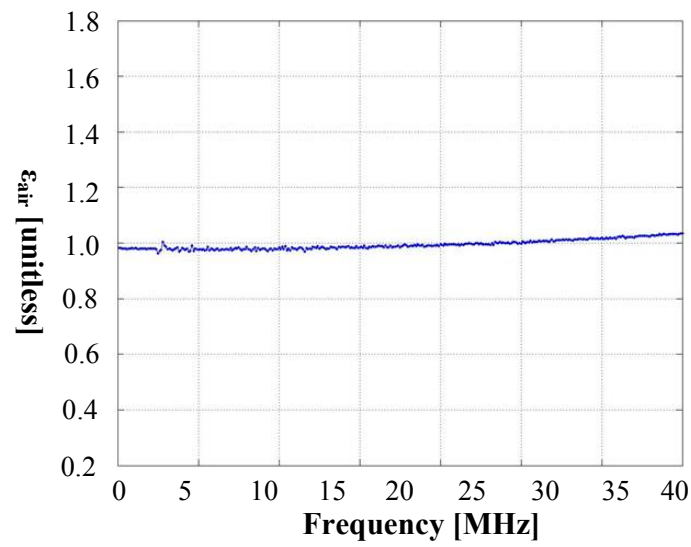


Figure 5.9: Equivalent circuit model for extraction of dielectric properties of air.



(a)



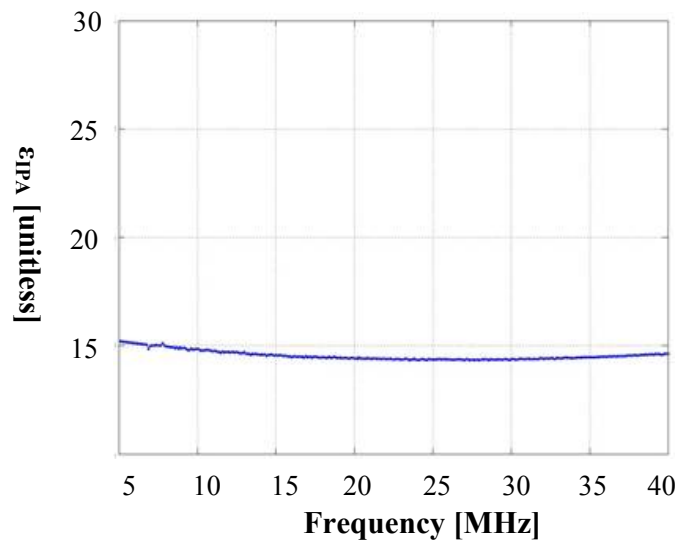
(b)

Figure 5.10: Plots of extracted (a) conductivity and (b) relative dielectric constant of air over various frequencies.

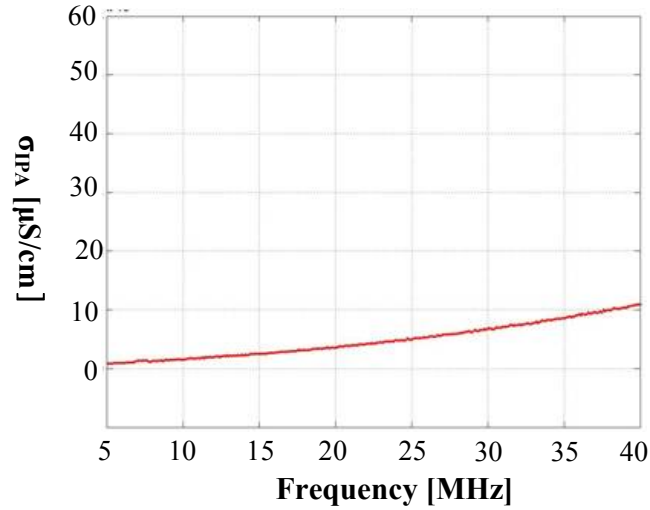
Figure 5.10 shows clearly that the extracted conductivity and dielectric constant of air are very close to the expected value. This self consistency check demonstrates that the fitting model analysis is valid.

5.4.1.2 Extraction of dielectric properties of IPA

Now let's assume that IPA is unknown material and initial guess value of $\epsilon_{mut}=30$ is used. Then, C_{ins} is calculated as 3.87 [pF/cm] using equation (5.6) and the first extracted dielectric constant and the conductivity of the "unknown" MUT are shown in Figure 5.11.



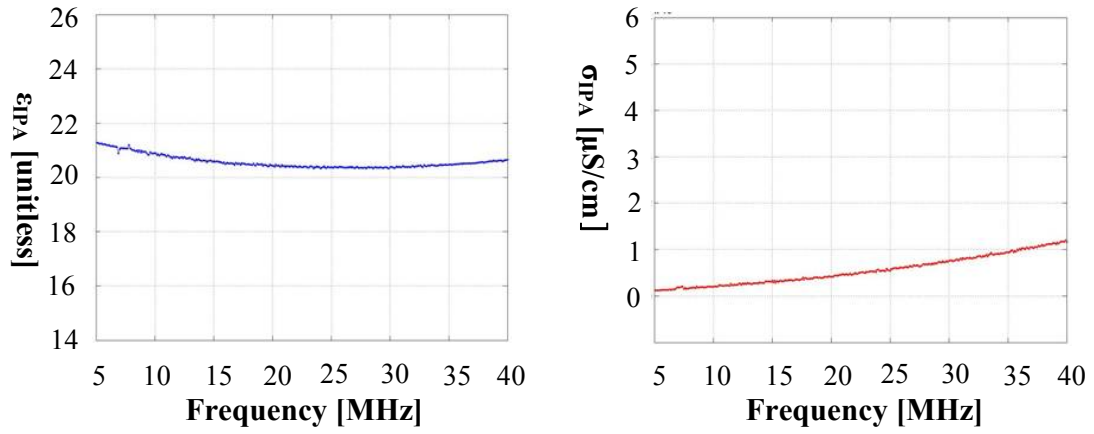
(a)



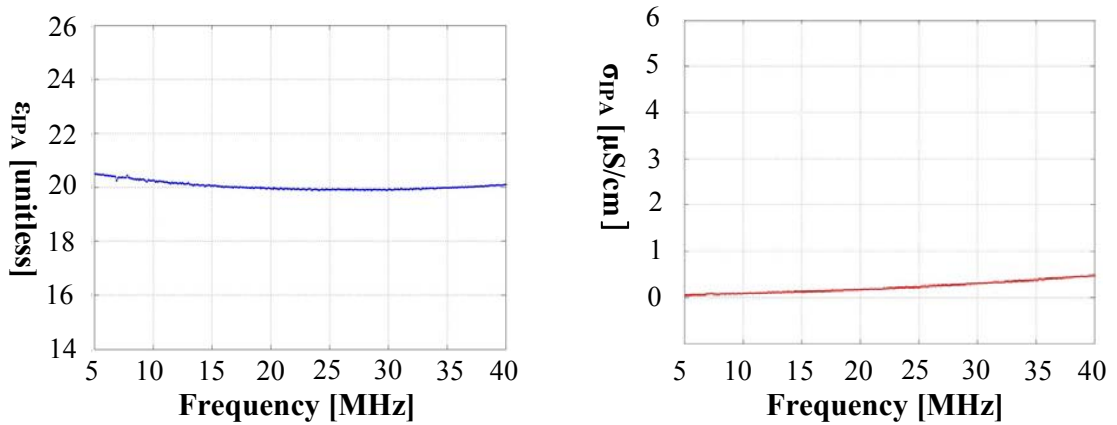
(b)

Figure 5.11: Plots of first extracted dielectric properties of IPA: (a) dielectric constant and (b) conductivity.

Then, the extracted dielectric constant of IPA is used again for the second iteration process and the calculation of C_{ins} . After the second iteration, new values of dielectric constant and conductivity are obtained and these are used again for the third iteration process. Figure 5.12 shows the results of the second and the third iteration processes. The iteration process stopped at the fourth iteration since it converged to the previous extracted values. The final result is shown in Figure 5.13. Note that the extracted dielectric constant of IPA is about 7% higher than the reference value ($\epsilon_{IPA}=18.6$), and the extracted conductivity is one order bigger than the reference value ($\sigma_{IPA}=0.06$ [$\mu\text{S}/\text{cm}$])[50]. However, the results are very promising if the conditions of the experimental environment is considered.



(a)



(b)

Figure 5.12: Plots of (a) the second iteration results with dielectric constant and conductivity and (b) the third iteration results with dielectric constant and conductivity of IPA.

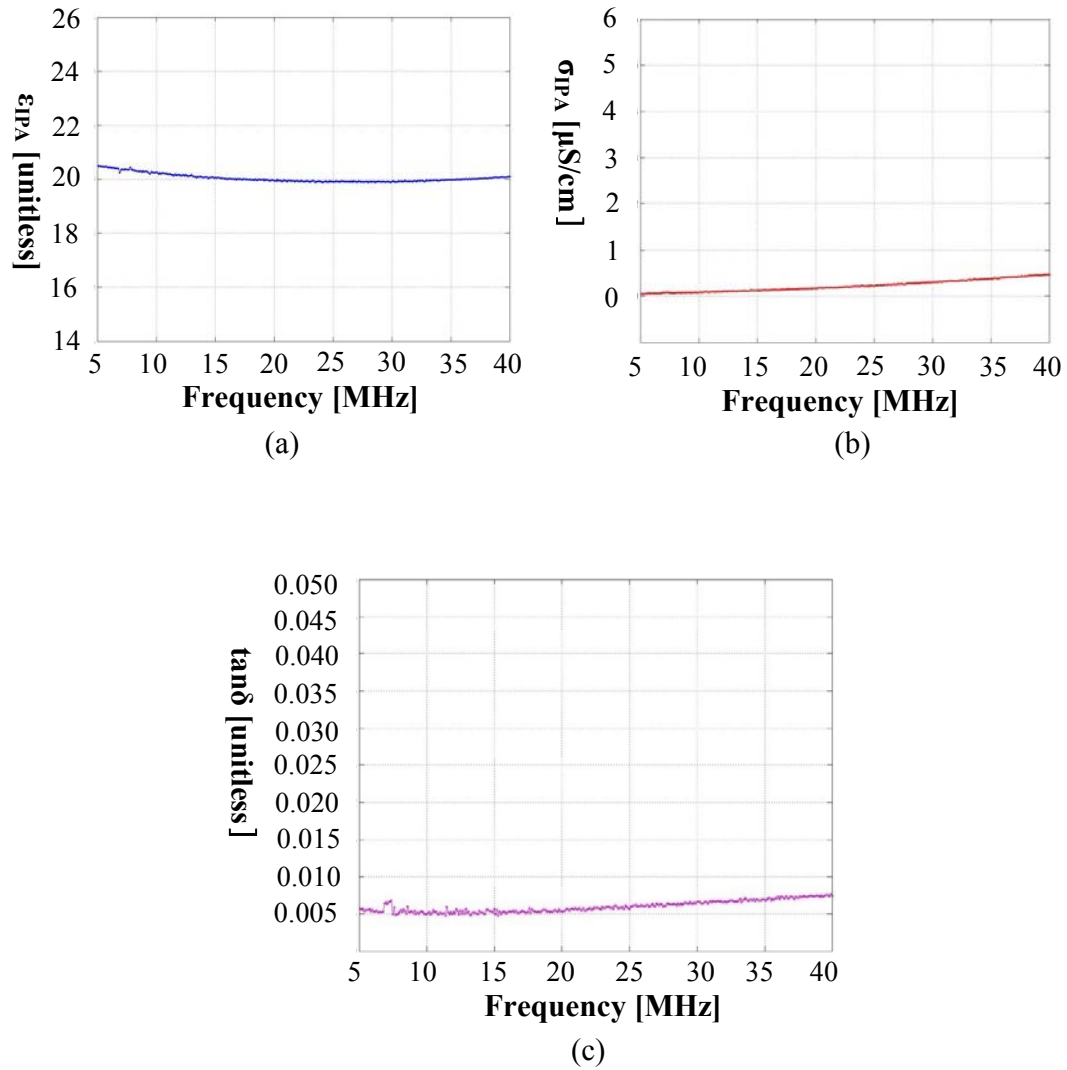


Figure 5.13: Plots of the final results of the fitting iteration processes: (a) extracted dielectric constant, (b) extracted conductivity, and (c) extracted $\tan\delta$ of IPA.

5.4.1.3 Extraction of dielectric properties of DI water

The initial guess value of $\epsilon_{mut}=60$ is used to extract dielectric properties of DI water. Again, fitting ϵ_{mut} and C_{ins} continue until they converge. Figure 5.14 shows the plots of the first and second iteration processes. The iteration stopped at fourth iteration and the final results are shown in Figure 5.15.

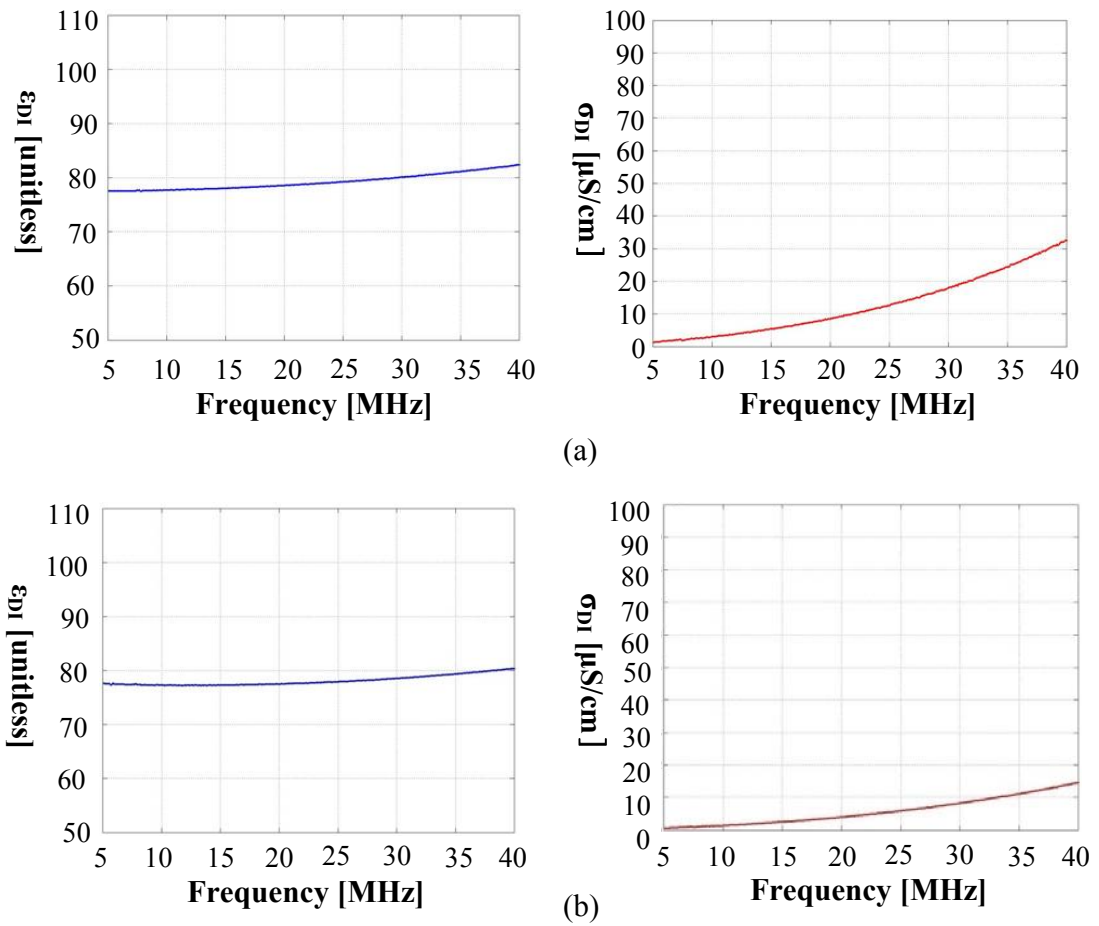


Figure 5.14: Plots of (a) the first iteration results with dielectric constant and conductivity and (b) the second iteration results with dielectric constant and conductivity of DI water.

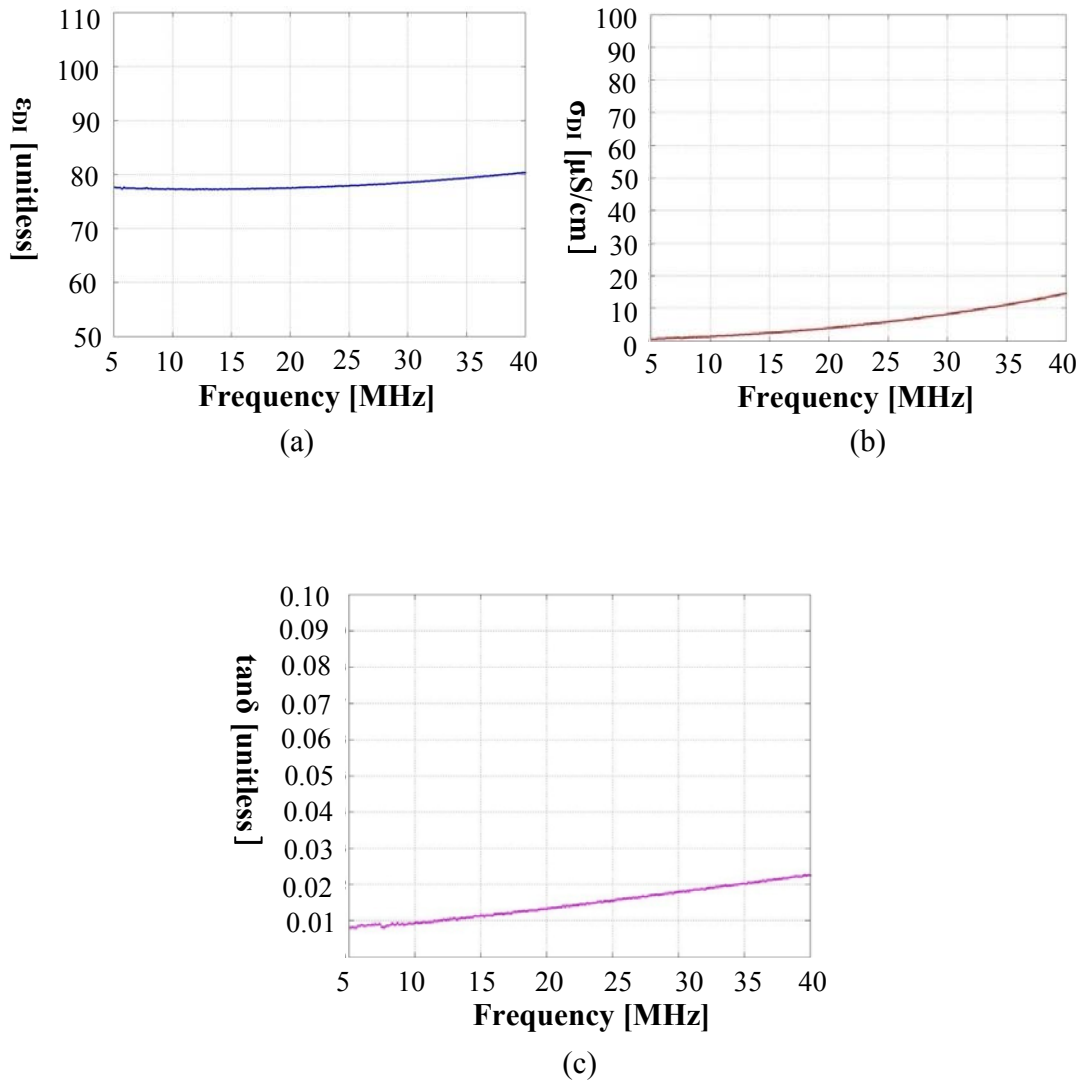


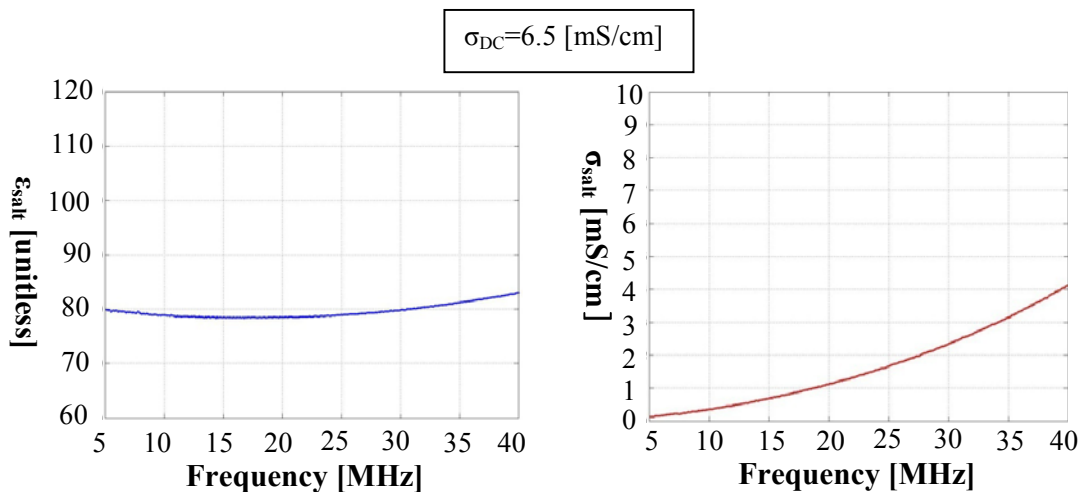
Figure 5.15: Plots of the final results of the fitting iteration processes: (a) extracted dielectric constant, (b) extracted conductivity, and (c) extracted $\tan\delta$ of DI water.

The extracted dielectric constant of DI water is in good agreement with the reference value ($\epsilon_{DI}=80$) within a 2.5% of error margin. However, the extracted conductivity value is much bigger than the reference value ($\sigma_{DI}=0.01$ [$\mu\text{S}/\text{cm}$])[51]. It is

concluded that the high extracted conductivity should account many factors since DI water is carried out from the clean room in a container and dispensed through a syringe pump, which might increase ion contamination.

5.4.1.4 Extraction of dielectric properties of salt water

Two different concentrations of salt water are tested. A commercial conductivity meter is used first to measure the DC conductivity of the salt water. The meter measured a conductivity of 6.5 [mS/cm] for one solution and 17 [mS/cm] for the other solution respectively. Then, fitting model analysis is used to extract the dielectric properties of the salt water. The initial guess value of $\epsilon_{mut}=60$ is used for both cases. The iteration processes are similar to the previous analysis. The iteration converged at fourth iteration and the results are shown in Figure 5.16.



(a)

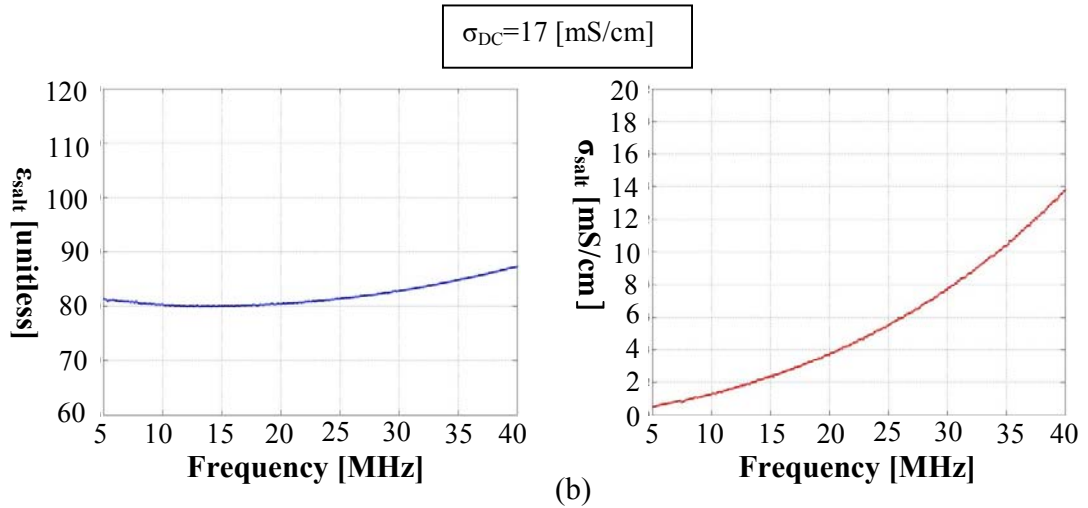


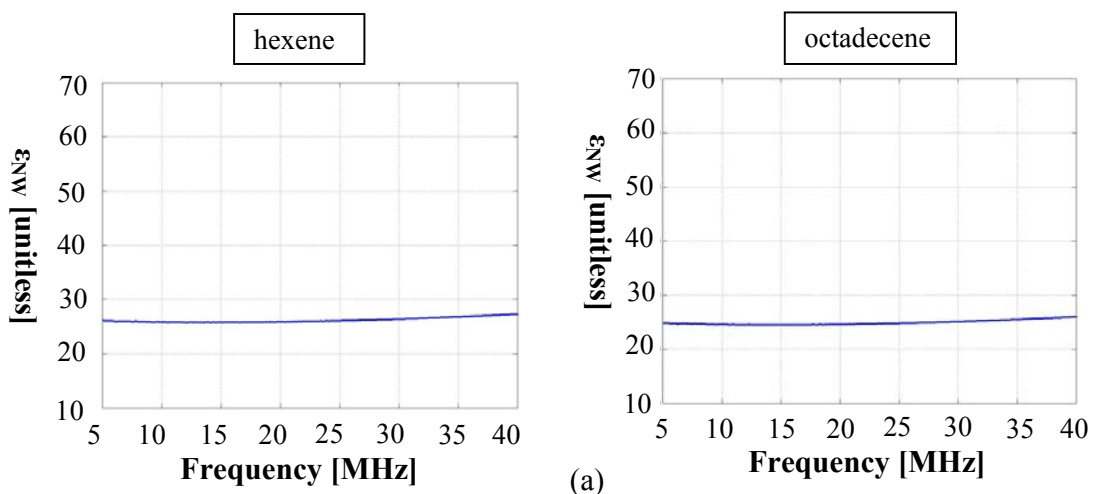
Figure 5.16: Plots of the final results of the fitting iteration processes: (a) extracted dielectric constant and conductivity of the salt water ($\sigma_{DC}=6.5$ [mS/cm]) and (b) extracted dielectric constant and conductivity of the salt water ($\sigma_{DC}=17$ [mS/cm]).

The extracted dielectric constant of the first salt water ($\sigma_{DC}=6.5$ [mS/cm]) is very close to the expected value ($\epsilon_{water}=80$) within a 2% of error margin and the second salt water ($\sigma_{DC}=17$ [mS/cm]) is about 7% of error margin. However, both extracted conductivities showing bigger errors but proportionally less than dc conductivity values. This unusual error might come from the double layer effect or electrode polarization effect at the interface between the insulation layer and the salt water.

5.4.2 Extract dielectric properties of unknown materials (GeNWs)

After successful measurement of dielectric properties of known materials, truly unknown materials such as germanium nanowires (GeNWs) are tested. The samples are prepared by Vincent C. Holmberg from the Dr. Brian A. Korgel's group at the department of chemical engineering of the University of Texas at Austin. The samples are 0.5% GeNWs by mass (3.9 mg of GeNWs dispersed in 790 mg of IPA). The carbon chain length of one sample is hexene and the other sample is octadecene respectively.

Again, the initial guess value of $\epsilon_{mut}=20$ is used for both samples for fitting model analysis. After several iterations, the extracted dielectric properties converged at fourth iteration for both cases. The final results are plotted in Figure 5.17. Unfortunately, both samples were hard to distinguish from one another, however, the extracted dielectric constant value was surprisingly high value. Given the dielectric constant of bulk Ge is 16, and that of IPA from the previous analysis is about 20, the extracted dielectric constant value of GeNWs of 26 indicates that the "effective" dielectric constant of the Ge nanowires is much bigger than 16. However, since this unusual result is beyond my research scope, I will not attempt to explain the result in more detail.



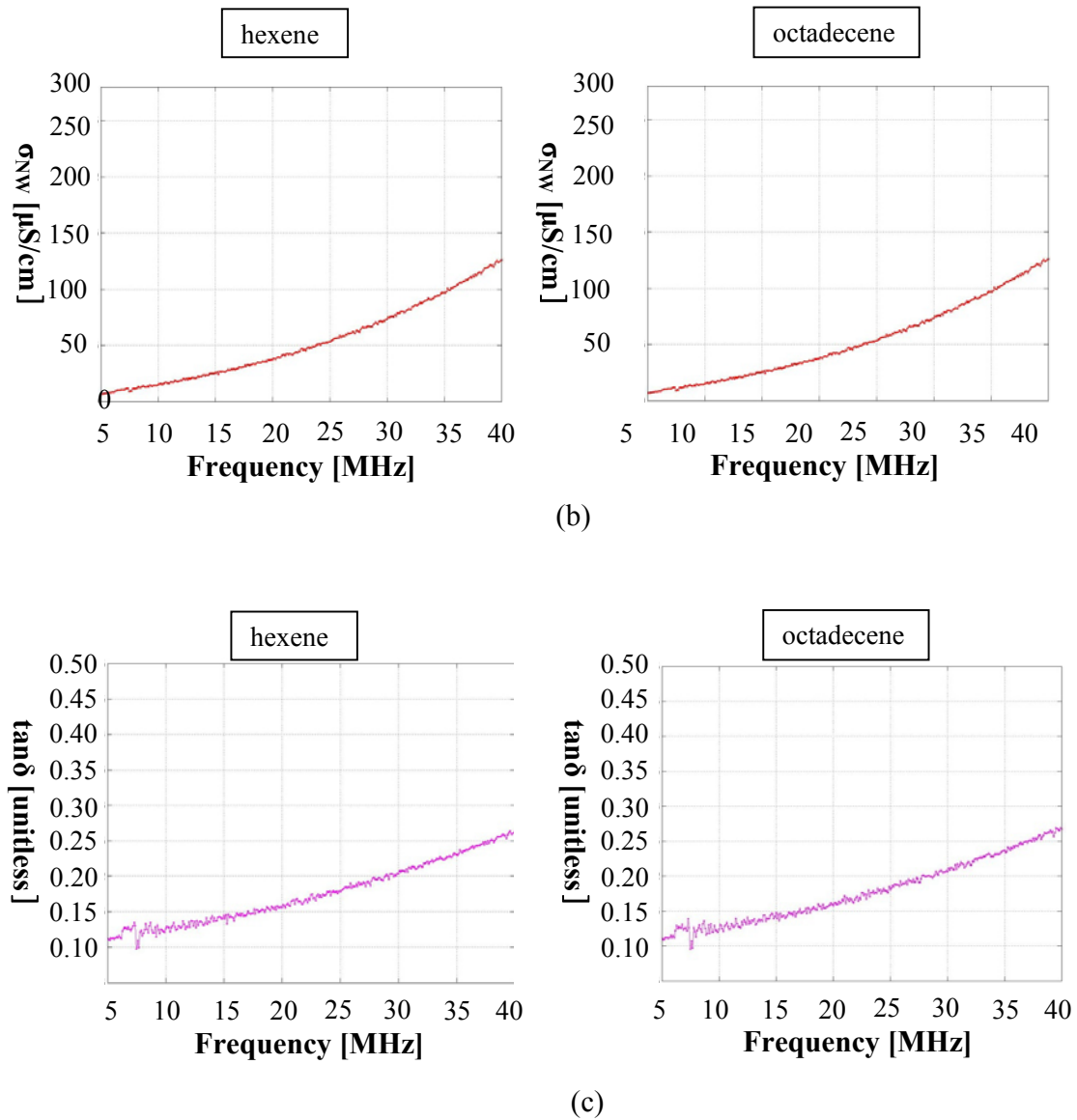


Figure 5.17: Plots of the final results of the fitting iteration processes for unknown materials (left column: GeNWs-hexene; right column: GeNWs-octadecene): (a) extracted dielectric constant, (b) extracted conductivity, and (c) extracted $\tan\delta$.

Chapter 6: Detection Mechanism of Wireless Measurement

This chapter presents an approach for indirect measurement technique in order to detect changes in the dielectric properties of MUT using a simple magnetically coupled wireless sensor, similar in concept to EAS (Electronic Article Surveillance) tags. These tags consist of a simple inductor-capacitor circuit which is characterized by a specific resonant frequency f_0 . The resonant frequency is determined by the values of the inductor and capacitor through the following relationship:

$$f_0 = \frac{1}{2\pi\sqrt{L \cdot C}} \quad (6.1)$$

In a similar fashion, the tag of our wireless sensor consists of an inductive coil connected to the IDC sensor, which is magnetically coupled to a separate reader coil. The more in-depth description of the detection mechanism is explained later in this section.

6.1 EAS-TAG LIKE WIRELESS SENSOR BASICS

Figure 6.1 shows a schematic diagram of magnetically coupled circuit between the reader and the tag coils of the wireless non-contact RFID-type measurement sensor. M represents the mutual inductance coupling between the reader and tag coils, and the tag is interrogated by measuring the input impedance Z_{in} from the reader coil. The center frequency f_0 of the “phase dip” is then used to analyze the state of the transducer.

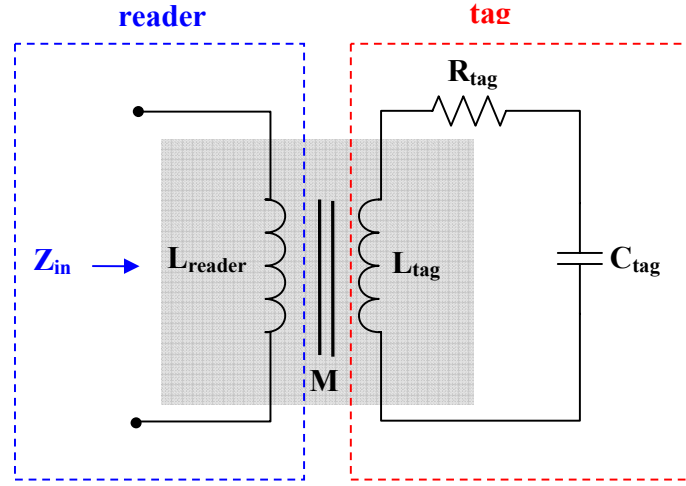


Figure 6.1: Schematic diagram of simple tag circuit for RFID-type measurement system.

The total input impedance of the circuit Z_{in} can be expressed in terms of the circuit parameters as follows

$$Z_{in} = j\omega L_{reader} + \frac{\omega^2 M^2}{j\omega L_{tag} + R_{tag} - \frac{j}{\omega C_{tag}}} \quad (6.2)$$

Equation (6.2) shows that changes in the tag portion of the circuit will cause a corresponding change in the measured impedance. This is the basic detection principle of the non-contact wireless measurement. In the following sections, effects of each parameter in tag portion, R_{tag} and C_{tag} , are explained respectively.

6.2 Effects of the R_{tag} and C_{tag}

In this section changes in phase of the input impedance due to the changes in the R_{tag} and C_{tag} are discussed. First, Figure 6.2 shows the phase responses with varying R_{tag} . The plots clearly show that if R_{tag} becomes larger the phase dip becomes shallower and broader. Note that the resonant frequency of the system remains the same.

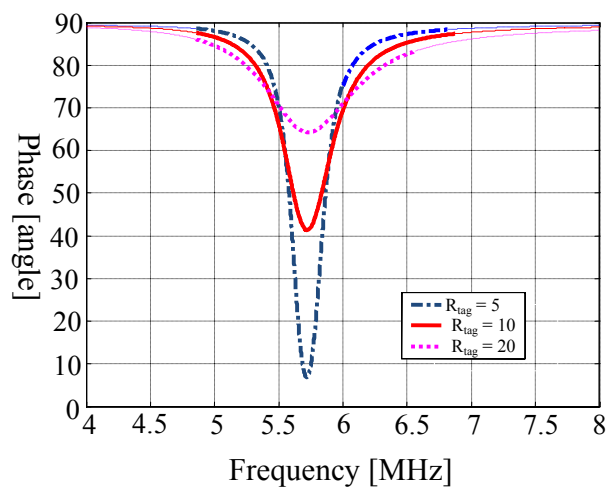


Figure 6.2: Phase plot of the input impedance with varying R_{tag} .

Another element that affects the input impedance is the capacitive load of the system. Equation (6.1) tells that when the capacitance increases, the resonant frequency of the tag should be changed, and the phase dip is predicted. Figure 6.3 shows phase plot with varying C_{tag} . As expected, as the C_{tag} increases, the phase dip occurs at lower frequencies. Note that the magnitude of the phase dip is also reduced with the increase of C_{tag} .

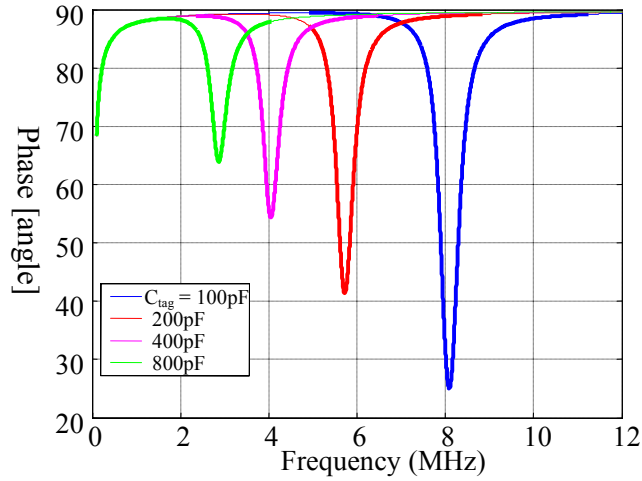


Figure 6.3: Phase plot of the input impedance with varying C_{tag}

6.3 Detection mechanism of wireless measurement

Figure 6.4 shows the schematic diagram of indirect wireless measurement system. The red box in the right side of the diagram represents IDC sensor with MUT, which is connected directly to the tag coil. Then the tag coil is inductively coupled to the reader coil, which is connected directly to the impedance analyzer meter. Figure 6.5 shows a photograph of the actual IDC wireless measurement setup.

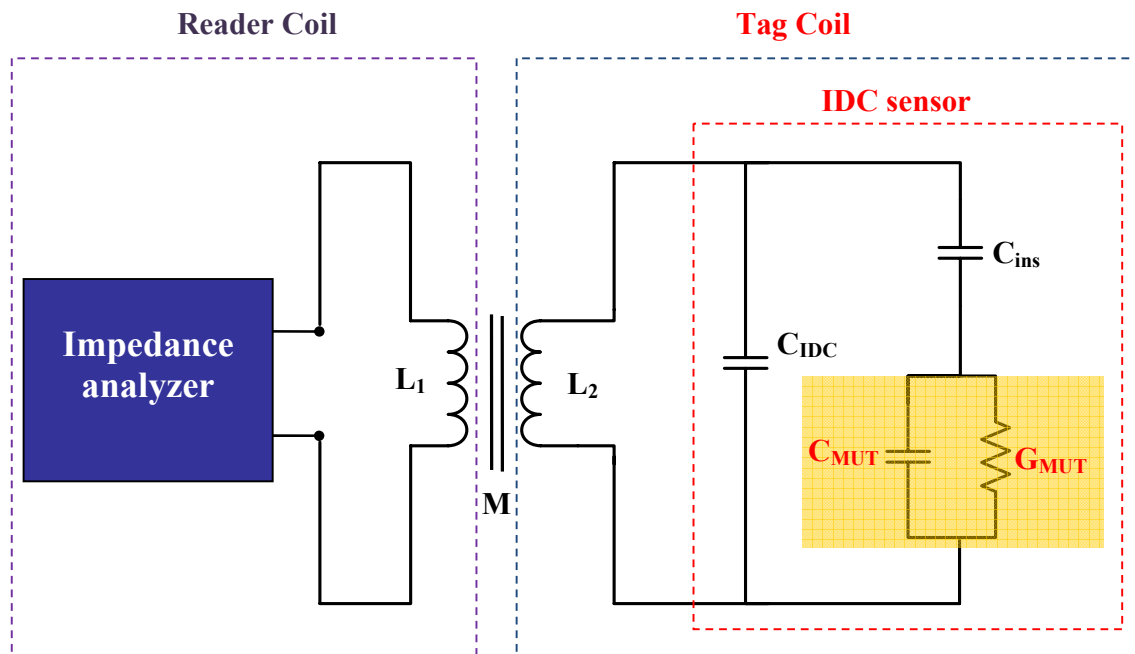


Figure 6.4: Schematic diagram of indirect wireless noncontact RFID-type measurement system.

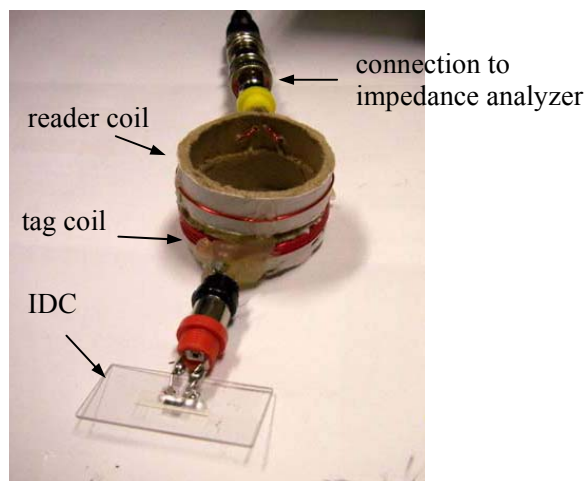


Figure 6.5: Photograph of the actual IDC wireless measurement setup.

Figure 6.6 are the experimental results using setup shown in Figure 6.5. The plots demonstrate that the wireless measurement system is very useful technique to detect easily the changes in the phase induced by the presence of different liquids. However, extracting the absolute dielectric properties of the MUT from the measurement data is very hard task, since this measurement setup involves many unknown parameters such as long cable, coupling factor, wires, etc. Therefore, effective analytical method needs to be designed in order to compensate those unknown parameter

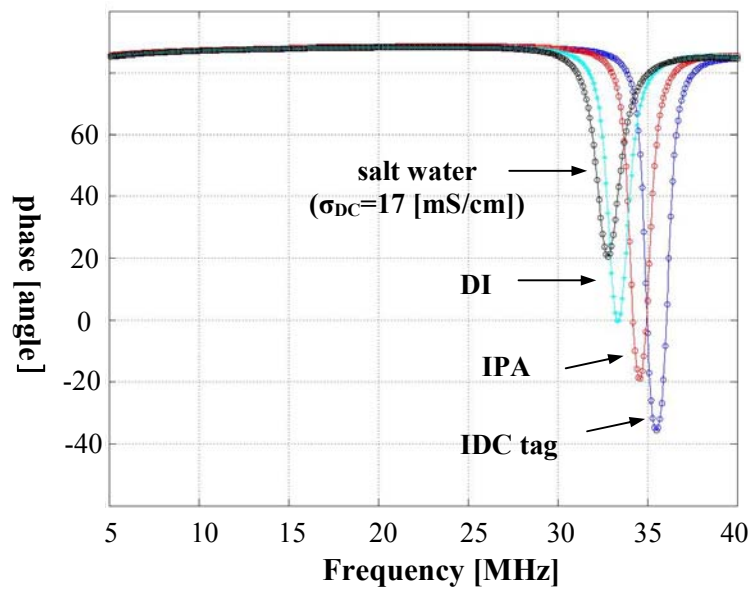


Figure 6.6: Phase plot change of several liquids over various frequencies.

Chapter 7: Conclusions and Future Work

An interdigital capacitor (IDC) sensor was designed, fabricated, and tested to measure dielectric properties of liquids. IDC electrodes are among the most widely used periodic electrode structures for the chemical sensing applications. The basic principle of detection mechanism relies on applying a spatially periodic fringing electric field into the material under test (MUT). Many researchers have investigated and developed IDC structures based on conformal mapping technique. Conformal mapping provides closed-form expressions for the computation of the capacitance of IDC electrodes. Based on conformal mapping technique, geometrical dimensions of our IDC sensor were designed.

In order to measure dielectric properties of liquids, the proper circuit model of the system must be defined first to interpret the measurement data. In chapter 5, several equivalent circuit models were proposed and analyzed. The initial circuit model was based on partial capacitance technique. The problem of this circuit model arises when MUT has relative dielectric constant bigger than that of the insulation layer. It involves negative capacitance which is not physically meaningful. In addition, parallel connection of capacitance of each layer does not make sense with the fringing electric flux path. Therefore, a new circuit model is proposed in order to overcome these problems.

In the second circuit model, the capacitance of the insulation layer is now connected in series with the capacitance of MUT. In addition, the insulation layer is no longer evaluated using conformal mapping technique and it is estimated using parallel plate model. However, we have found that this circuit model overlooks some very important parameters in order to obtain accurate information about MUT. The first parameter is the “loss” in the insulation layer which can not be ignored. The second

parameter is a portion of the electric flux flowing within the insulation layer, which account other “loss” term. And, the third, the most important of all, is the correlation between the capacitance of the insulation layer and the dielectric constant of MUT. In other words, the capacitance of the insulation layer must be calculated based on the dielectric constant of MUT.

The third modified equivalent circuit model was designed accordingly including the important parameters. While analyzing the third circuit model with the actual measured data, the correlation between the insulation layer and the dielectric constant of MUT was extracted. The maximum electric flux within the insulation layer was modeled as well using parallel plate analysis.

One notable achievement in this research is that we have defined new analytical evaluation method called fitting model analysis to extract the dielectric properties of MUT. The fitting model analysis consists of iterative extraction processes by simultaneously fitting both C_{mut} and C_{ins} . It begins with an initial guess value of the dielectric constant of MUT and the iteration processes continue until the extracted values converge. This fitting model analysis was tested by extracting dielectric properties of known liquids such as DI water, IPA, and salt water and it was proved that the fitting model worked so well that the extracted values are in good agreement with the reference data.

After successful test of the known materials, the fitting model analysis was used for extracting dielectric properties of truly unknown materials such as germanium nanowires (GeNWs). The extracted dielectric constant of GeNWs was about 26. Given the dielectric constant of bulk Ge is 16, and that of IPA from fitting model analysis is 20, the extracted value of 26 indicates that the “effective dielectric constant of the Ge

nanowires is much bigger than 16. This extracted value is surprisingly higher than we expected.

It was proved from the previous test with known liquids that the extracted values are correctly estimated from measurement and we have not seen any example of anything odd. However, we can not conclude yet that this unusually high value is the right answer. Even though this is beyond my research scope, we definitely need more collection of data of GeNWs to verify what this unusual number actually means. So, possible future works might be obtaining more fresh GeNWs samples and testing them more extensively in order to obtain more supportive information about GeNWs.

Another part of this research was to demonstrate the indirect wireless measurement using a simple magnetically coupled wireless sensor, similar in concept to EAS (Electronic Article Surveillance) tags. The experimental results showed that this novel approach is very useful technique to detect changes in the tag circuit. In other words, the capacitance changes of MUT are easily spotted using this wireless technique. However, the extraction of the dielectric properties of MUT from measurement data is not an easy task due to many unknown parameters such as coupling efficiency, parasitic in the long measurement cable, etc. Therefore, another possible future works for this application might be the design of effective analytical approach to calibrate those parasitic from the measurement data. Finally, additional future work might be the integration of the IDC electrodes into the actual microfluidic system in order to measure the dielectric properties of fluids flowing inside the system.

References

- [1] Henry Baltes, "CMOS Micro Electro Mechanical Systems," *Sensors and Materials*, Vol. 9, No. 6, pp. 331-346, 1997.
- [2] P. Rai-Choudhury, *MEMS and MOEMS Technology and Applications*, Bellingham, Washington: The Society of Photo-Optical Instrumentation Engineers, 2000.
- [3] Gregory T. A. Kovacs, *Micromachined Transducers Sourcebook*, New York, NY: The McGraw-Hill Companies, Inc., 1998.
- [4] Abe, H., Esashi, M., and Matsuo, T., "ISFETs Using Inorganic Gate Thin Films," *IEEE Transactions on Electronic Devices*, vol. ED-26, no. 12, pp. 1939-1944, Dec. 1979.
- [5] Johnson, C. L., Wise K. D., and Schwank, J. W., "A Thin-Film Gas Detector for Semiconductor Process gases," *Digest of the International Electron Devices Meeting (IEDM)*, p. 662, San Francisco, CA, Dec. 1988.
- [6] Kondoh, J., and Shiokawa, S., "Liquid Identification Using SH-SAW Sensors," *Proceedings of Transducers '95, the 8th International Conference on Solid-State Sensors and Actuators*, vol. 2, pp. 716-719, Stockholm, Sweden, June, 1995.
- [7] Kang, J., Kim, Y., Kim, H., Jeong, J., and Park, S., "Comfort Sensing System for Indoor Environment," *Proceedings of Transducers '97, the 1997 International Conference on Solid-State Sensors and Actuators*, vol. 1, pp. 311-314, Chicago, June, 1997.

- [8] Lee, H.-S., Wang, S. S., Smolenski, D. J., Viola, M. B., and Klusendorf, E. E., "In Situ Monitoring of High-Temperature Degraded Engine Oil Condition with Microsensors," *Sensors and Actuators*, vol. B20, no. 1, pp. 49-54, May, 1994.
- [9] J. Lavigne, S. Savoy, M. B. Clevenger, B. McDaniel, S. J. Yoo, E. V. Anslyn, J. T. McDevitt, J. Shear, and D. Niekirk, "Solution-based Analysis of Multiple Analytes by a Sensor Array: Toward the Development of an "Electronic Tongue", *J. Am. Chem. Soc.*, 1998, vol. 120, 6429-6430.
- [10] A. Goodey, J. J. Lavigne, S. M. Savoy, M. Rodriguez, T. Curey, A. Tsao, G. Simmons, J. Wright, S. J. Yoo, Y. Sohn, E. V. Anslyn, J. B. Shear, D. P. Neikirk, J. T. McDevitt, "Development of Multi analyte Sensor Arrays Composed of Chemically Derivatized Polymeric Microspheres Localized in Micromachined Cavities," *J. Am. Chem. Soc.* (2001), 123 (11), 2559-2570.
- [11] Gwynne, Peter, "Microfluidics on move: devices offer many advantages," *OE-Reports*, No. 200, Aug. 2000.
- [12] A. V. Mamishev, S. R. Kishore, F. Yang, Y. Du, M. Zahn, "Interdigital Sensors and Transducers," *Proceedings of the IEEE*, vol. 92, no. 5, May 2004, 808-845.
- [13] I. N. Court, "Microwave acoustic devices for pulse compression filters," *IEEE Trans. Microwave Theory Tech.* no. MTT-17, pp. 968-986, 1969.
- [14] G. D. Alley, "Interdigital capacitors and their application to lumped-element microwave integrated circuits," *IEEE Trans. Microwave Theory Tech.* MTT-18, pp. 1028-1033, 1970.
- [15] R. K. Hoffman, *Handbook of Microwave integrated circuits*, Artech, Norwell, MA, 1987.

- [16] N. Delmonte, B. E. Watts, G. Chiorboli, P. Cova, R. Menozzi, "Test structures for dielectric spectroscopy of the thin films at microwave frequencies," *Microelectronics Reliability*, 47, pp.682-685, 2007.
- [17] P. Van Gerwen et al., "Nanoscaled interdigitated electrode arrays for biochemical sensors," *Sensors and Actuators B*, 49, pp. 73-80, 1998.
- [18] L. Montelius, J. Tegenfeldt, T. Ling, "Fabrication and characterization of a nanosensor for admittance spectroscopy of biomolecules," *J. Vac. Sci. Technol. A*, 13 (3), pp. 1755-1760, 1995.
- [19] P. Jacobs et al. "Impedimetric detection of nucleic acid hybrids," *Proceedings of the Second International Conference on Microreaction Technology*, New Orleans, LA, March, pp. 8-12, 1998.
- [20] N. F. Shepard, D. R. Day, H. L. Lee, S. D. Senturia, "Microdielectrometry," *Sensors and Actuators*, 2, pp. 263-274, 1982.
- [21] M. C. Zaretsky, L. Mouayad, J. R. Melcher, "Continuum properties from interdigital electrode dielectrometry," *IEEE Transactions on Electrical Insulation*, vol. 23, no. 6, Dec. 1988.
- [22] C. Hagleitner, A. Hierlemann, D. Lange, A. Kummer, N. Kerness, O. Brand, H. Baltes, "Smart single-chip gas sensor microsystems," *Nature*, 414, pp 293-296, 2001.
- [23] R. Casalini, M. Kilitziraki, D. Wood, M. C. Petty, "Sensitivity of the electrical admittance of a polysiloxane film to organic vapors," *Sensors and Actuators B*, 56, pp. 37-44, 1999.

- [24] Novak, Lisa J.; Grizzle, Kristi M.; Wood, Sharon L.; Neikirk, Dean P., "Development of state sensors for civil engineering structures," Proceedings of SPIE's Vol. 5057 8th Annual International Symposium on NDE for Health Monitoring and Diagnostics: Smart Systems and NDE for Civil Infrastructures, March 3-6, 2003, pp. 358-363.
- [25] J. T. Simonen, M.M. Andringa, K.M. Grizzle, S.L. Wood, and D.P. Neikirk, "Wireless sensors for monitoring corrosion in reinforced concrete members," Proceedings of SPIE, Smart Structures and Materials 2004: Smart Systems and Nondestructive Evaluation for Civil Infrastructures, Vol. 5391, 2004, pp. 587-596.
- [26] Deniz Armani, Chang Liu and Narayan, "Reconfigurable fluid circuits by PDMS elastomer micromachining," Microelectronic Laboratory, University of Illinois-Urbana-Champaign.
- [27] http://www.microchem.com/products/su_eight.htm.
- [28] J. R. Macdonald, *Impedance Spectroscopy: emphasizing solid materials and systems*, New York, NY: John Wiley & Sons, Inc. 1987.
- [29] M. E. Orazem & B. Tribollet, *Electrochemical Impedance Spectroscopy*, New Jersey: John Wiley & Sons, Inc. 2008.
- [30] http://www.uni-mainz.de/FB/Chemie/AK-Janshoff/129_DEU_HTML.php.
- [31] C. Iliescu, D. P. Poenar, M. Carp, F. C. Loe, "A microfluidic device for impedance spectroscopy analysis of biological samples," Sensors and Actuators B, 123, pp. 168-176, 2007.
- [32] L. Yang, Y. Li, G. F. Erf, "Interdigitated array microelectrode-based electrochemical impedance immunosensor for detection of Escherichia coli O157:H7," Analytical Chemistry, 76, pp. 1107-1113, 2004.

- [33] S. K. Mohanty, S. K. Ravula, K. Engisch, A. B. Frazier, "Micro electrical impedance spectroscopy of bovine chromaffin cells," *Microtechnologies in Medicine & Biology Second Annual International Conference IEEE-EMB*, Madison, Wisconsin, May 2-4, 2002.
- [34] F. Laugere, G. W. Lubking, A. Berthold, J. Bastemeijer, and M. J. Vellekoop, "Downscaling aspects of a conductivity detector for application in on-chip capillary electrophoresis." *Sensors and Actuators*, 92, pp. 109-114, 2001.
- [35] J. G. A. Brito-Neto et al., "Understanding capacitively coupled contactless conductivity detection in capillary and microchip electrophoresis. Part 1. Fundamentals." *Electroanalysis*, 17, no. 13, 2005.
- [36] P. Jacobs, A. Varlan, and W. Sansen, "Design optimization of planar electrolytic conductivity sensors," *Medical and Biological Engineering and Computing*, 33, pp. 802-810, 1995.
- [37] J. Lichtenberg, N. F. de Rooij, E. Verpoorte, "A microchip electrophoresis system with integrated in-plane electrodes for contactless conductivity detection," *Electrophoresis*, 23, pp. 3769-3780, 2002.
- [38] P. Debye, *Polar Molecules*, New York: Chemical Catalog Co., 1954.
- [39] A. V. Mamishev, "Interdigital dielectrometry sensor design and parameter estimation algorithms for non-destructive materials evaluation." Department of Electrical Engineering and Computer Science, Massachusetts Institute of Technology, 1999.
- [40] Application Note 1217-1, "Basics of measuring the dielectric properties of materials," Hewlett Packard literature number 5091-3300E, 1992.
- [41] J. S. Wei, "Distributed capacitance of planar electrodes in optic and acoustic surface wave devices," *IEEE J. Quantum Electron.* QE-13, 152-158, 1977.

- [42] C. Veyres and F. Hanna, "Extension of the application of conformal mapping techniques to coplanar lines with finite dimensions," *Int. J. Electronics*, vol. 48, no. 1, pp. 47-56, 1980.
- [43] S. M. Wentworth, Dean P. Neikirk, and Carl R. Brahce, "The high-frequency characteristics of tape automated bonding (TAB) interconnects," *IEEE Trans. Components, Hybrids, and Manufacturing Technology*, vol. 12, no. 3, pp 340-347, September 1989.
- [44] S. S. Gevorgian, T. Martinsson, Peter L, J. Linner, E. L. Kollberg, "CAD models for multilayered substrate interdigital capacitors," *IEEE Trans. Microwave Theory and Techniques*, vol. 44, no. 6, pp. 896-904, June 1996.
- [45] R. Igreja and C. J. Dias, "Analytical evaluation of the interdigital electrodes capacitance for a multi-layered structure, *Sensors and Actuators A: Physical*, vol. 112, issues 2-3, pp. 291-301, May 2004.
- [46] J.W. Brown, R.V. Churchill, *Complex Variables and Applications*, 6th ed., McGraw-Hill, New York, 1996, pp.326-346.
- [47] Wolfgang Hilberg, "From Approximations to Exact Relations for Characteristic Impedances," *IEEE Transactions on Microwave and Techniques*, vol. MTT-17, no. 5, pp. 259, May 1969.
- [48] Hewlett-Packard 4194A Impedance/Gain-Phase Analyzer operational manual.
- [49] Robert James Friar, "Analysis, Design, and Measurement of On-Wafer Transmission Line Test Structures," PhD Dissertation, May 2000.
- [50] <http://www.shellchemicals.com/products/1,1098,63,00.html>.
- [51] <http://www.myronl.com/applications/diapp.htm>.

Vita

Jun Wan Kim was born in the Republic of Korea on December 17, 1972, the second son of Song Ja Jung. His family moved to Ecuador in 1988, and Jun Wan transferred to San Jose La Salle high school. After graduating in 1991, Jun Wan entered Escuela Superior Politecnica del Litoral. In 1994, he transferred to the College of Engineering at The University of Texas at Austin and graduated with his Bachelor of Science in Electrical Engineering in December of 1999. Jun Wan entered the Graduate School at the University of Texas at Austin in August, 2000. Jun Wan received his Master of Science in Engineering in 2003 under the supervision of Dr. Dean P. Neikirk.

Permanent address: 2320 Babcock Rd. San Antonio TX 78229

This dissertation was typed by the author.